

AD 749506

REPORT NO. 4

MELT-GROWN OXIDE-METAL COMPOSITES

ANNUAL TECHNICAL REPORT

(Period: 10 June 1971 to 9 June 1972)

Project Director

A. T. Chapman

Principal Investigators

J. F. Benzel J. K. Cochran

R. K. Feeney J. W. Hooper

J. D. Norgard

Sponsored By

Advanced Research Projects Agency

Department of Defense

ARPA ORDER NO. 1637

Contract No. DAAH01-71-C-1046

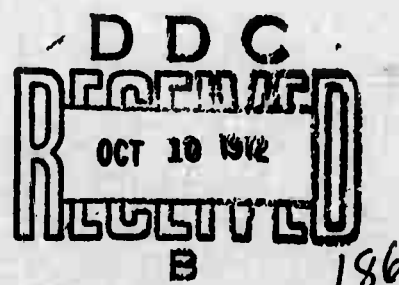
July 1972

Reproduced by
**NATIONAL TECHNICAL
INFORMATION SERVICE**
U S Department of Commerce
Springfield VA 22151



**School of Ceramic Engineering
GEORGIA INSTITUTE OF TECHNOLOGY
Atlanta, Georgia**

Distribution of this document is unlimited.



**BEST
AVAILABLE COPY**

DOCUMENT CONTROL DATA - R & D

(Security classification of title, body of abstract and indexing annotation must be entered when the overall report is classified)

1 ORIGINATING ACTIVITY (Corporate author)

School of Ceramic Engineering
Georgia Institute of Technology

2a. REPORT SECURITY CLASSIFICATION

Unclassified

2b. GROUP

3 REPORT TITLE

MELT-GROWN OXIDE-METAL COMPOSITES

4 DESCRIPTIVE NOTES (Type of report and inclusive dates)

Final (10 June 1971 - 9 June 1972)

5. AUTHOR(S) (First name, middle initial, last name)

Alan T. Chapman, James F. Benzel, J. K. Cochran, Robert K. Feeney,
John W. Hooper, J. D. Norgard

6 REPORT DATE

July 1972

7a. TOTAL NO. OF PAGES

170

7b. NO. OF REFS

12

8a. CONTRACT OR GRANT NO.

DAAH01-71-C-1046

9a. ORIGINATOR'S REPORT NUMBER(S)

E18-604-4

b. PROJECT NO

c.

d.

9b. OTHER REPORT NO(S) (Any other numbers that may be assigned this report)

ARPA ORDER NO. 1637

10. DISTRIBUTION STATEMENT

Distribution of this document is unlimited.

11. SUPPLEMENTARY NOTES

12 SPONSORING MILITARY ACTIVITY

Advanced Research Projects Agency
1400 Wilson Blvd.
Arlington, Virginia 22209

13 ABSTRACT

Research work is underway developing melt-grown oxide-metal composite structures for electron emission testing. Prior to this report period extensive composite growth of an array of metallic fibers uniformly distributed in an oxide matrix had been achieved only in the system UO_2 -W. In this report period well grown oxide-metal composite structures have been obtained in the systems Y_2O_3 stabilized ZrO_2 -W, Y_2O_3 stabilized HfO_2 -W, UO_2 -Ta, and the rare earth oxides (Gd_2O_3 , Nd_2O_3 or La_2O_3)-Mo or W. Metallic fiber densities in these systems have been varied between 7 to 70 million per cm^2 . The importance of the stoichiometry of the molten oxide on metal solubility was established in the system UO_2 -W and exploited in the rare earth oxide-metal systems (through doping with CeO_2) to achieve uniform composite structures and mechanically sound samples. Minor input power fluctuations were conclusively shown to be a major cause of discontinuous (banded) fiber growth. Selective chemical etching studies successfully exposed the W fibers in stabilized ZrO_2 and HfO_2 -W specimens. A two-step etching procedure was used to sharpen just the tips of W fibers in UO_2 -W samples. A variety of contact and cleaning approaches were tested to achieve "good" electrical contact with the small metallic fibers in composite samples. Many UO_2 -W samples containing different pin geometries with various anode configurations were tested in a field emission diode assembly. A maximum emission current density of 200 mA/cm^2 , approximately twice that obtained previously, has been achieved. A theoretical analysis of the electron emission of pin arrays is in progress.

KEY WORDS	LINK A		LINK B		LINK C	
	ROLE	WT	ROLE	WT	ROLE	WT
Oxide-Metal Composites		4				
Field Emission		4				
Rf Heating		3				
Field Emission Theory		3				
Oxides		2				
Refractory Metals		2				
Unidirectional Solidification		4				
Eutectic Structures		3				
UO ₂		2				
ZrO ₂ (Stabilized)		1				
HfO ₂ (Stabilized)		1				
Gd ₂ O ₃		2				
Nd ₂ O ₃		2				
La ₂ O ₃		2				
Internal Melting		3				
Etching		2				
Tungsten Fibers		4				
Molybdenum Fibers		4				
Electron Emitting Arrays		4				
Oxide-Metal Solidification		3				
High Field Emission		4				

16

Report No. 4

MELT-GROWN OXIDE-METAL COMPOSITES

ANNUAL TECHNICAL REPORT

(Period: 10 June 1971 - 9 June 1972)

from

THE SCHOOL OF CERAMIC ENGINEERING

GEORGIA INSTITUTE OF TECHNOLOGY

ATLANTA, GEORGIA 30332

PROJECT DIRECTOR: A. T. CHAPMAN

July 1972

Sponsored by:

ADVANCED RESEARCH PROJECTS AGENCY

DEPARTMENT OF DEFENSE

ARPA ORDER NO. 1637

CONTRACT NO. DAAH01-71-C-1046

Distribution of this document is unlimited.

Details of the distribution of
this document are contained in
the attached document

10

PERSONNEL PARTICIPATING IN PROJECT

Principal Investigators

J. F. Benzel
J. K. Cochran
R. K. Feeney
J. W. Hooper
J. D. Norgard

Graduate Students

W. F. Beaver
N. E. Grynkewich
C. C. Jen
T. A. Johnson
W. L. Ohlinger
M. C. Pao
J. W. Stendera
M. D. Watson

Undergraduate Students

J. A. Graves
G. B. Ricks

TABLE OF CONTENTS

<u>Section</u>	<u>Title</u>	<u>Page</u>
I	INTRODUCTION	1
II	INDUCTION COUPLING AND SOLIDIFICATION BEHAVIOR OF OXIDES AND OXIDE-METAL MIXTURES	7
	A. Induction Coupling and Melting Behavior of Oxide Systems	7
	B. Solidification Behavior of Oxide-Metal Systems	14
	1. Stabilized HfO_2 -W	15
	2. Stabilized ZrO_2 -W	28
	3. UO_2 -Metal	45
	4. Rare Earth Oxide-Metal	65
	C. Electron Beam Solidification Techniques	85
III	THE FORMATION OF OPTIMUM EMITTING ARRAYS	88
IV	OXIDE METAL COMPOSITE PROPERTIES	98
	A. Electrical Resistivity	98
	1. Resistivity Calculations and Resistance Measurements	98
	2. Effect of Chemical Cleaning and Vapor Deposited Contacts	99
	B. Electro-Chemical Effects	101
	1. Composite Anodes	107
	2. Composite Cathodes	107
	C. Summary	114
		118
V	EXPERIMENTAL EMISSION MEASUREMENTS	119
	A. Experimental Apparatus	119
	B. Electron Emission Measurements	121
	1. Unique Emitter Geometry	122
	2. ZrO_2 -W Composite Type Electron Emitters	128
	3. Correlation of Emission With Pin Continuity	129
	4. Effects of Various Anode Configurations	132
	5. High Current Emitter Development	133
VI	THEORETICAL ANALYSIS OF ELECTRON EMITTING ARRAYS	141
	A. Models	142
	1. Prolate Spheroids	143
	2. Oblate Spheroids	148
	B. Numerical Solutions	153
	1. Potential Distribution	153
	2. Electric Field Intensity	158
	3. Current Density	159
	4. Total Current	161
	C. Sample Run	161
VII	SUMMARY	163

LIST OF ILLUSTRATIONS

<u>Figure</u>	<u>Title</u>	<u>Page</u>
1	Schematic Diagram of the Facility for the Growth of Oxide-Metal Composites.	2
2	Dendritic W Growth in a Solidified HfO_2 - 20 Mole % CaO - 6 Weight % W Sample.	17
3	Random W Fibers in a Solidified HfO_2 - 20 Mole % CaO - 6 Weight % W Sample.	17
4	Two-Phase Oxide Matrix Present in the CaO Stabilized HfO_2 - 6 Weight % W Sample.	18
5	Poor Fiber Growth in a Solidified HfO_2 - 20 Mole % CaO - 12.6 Weight % W Sample.	18
6	Good Eutectic Growth in a Solidified HfO_2 - 10 Mole % Y_2O_3 - 9.1 Weight % W.	19
7	Nonuniform Solidification Areas in Y_2O_3 Stabilized HfO_2 -W Samples. a) Banded Fiber Growth, b) Platelet and Rod Growth.	21
8	Primary Oxide Areas in Solidified HfO_2 - 10 Mole % Y_2O_3 - 10.7 Weight % W.	22
9	Transverse and Longitudinal Sections of "Good" Fiber Growth in a Y_2O_3 Stabilized HfO_2 Sample to Which 14 Weight % W Was Added. a) Transverse Section, b) Longitudinal Section.	23
10	Tungsten Dendrites and Areas of Fan Growth in Solidified HfO_2 - 10 Mole % Y_2O_3 - 13.8 Weight % W.	24
11	Typical Cross Section of a Solidified HfO_2 - 10 Mole % Y_2O_3 - 12.3 Weight % W Pellet Showing Cracking Present.	24
12	Typical Cracking in Solidified HfO_2 Stabilized With (a) 15, and b) 20 Mole % Y_2O_3 and Containing 12.3 Weight % W.	26
13	Colony or Cell Boundaries Typically Observed in Y_2O_3 Stabilized HfO_2 -W Samples. a) Longitudinal Section, b) Scanning Electron Micrograph of Transverse Section, Sample Selectively Etched to Expose the Fibers.	27
14	The Effect of a W Dendrite on Fiber Growth in a ZrO_2 - 10 Mole % Y_2O_3 - 17 Weight % W Sample.	31

LIST OF ILLUSTRATIONS (Continued)

<u>Figure</u>	<u>Title</u>	<u>Page</u>
15	The Effect of Growth Rate on W Fiber Density in ZrO ₂ - 10 Mole % Y ₂ O ₃ % W Samples. a) Growth Rate 0.51 cm/hr, b) Growth Rate 5.9 cm/hr.	36
16	The Effect of Varying Growth Rate on the W Fiber Diameter in Y ₂ O ₃ Stabilized ZrO ₂ -W Samples.	37
17	Discontinuous W Fibers in a ZrO ₂ - 10 Mole % Y ₂ O ₃ Samples in Which a Few Fibers Apparently Cross the Band.	39
18	Wide Growth Discontinuity in Y ₂ O ₃ Stabilized ZrO ₂ Sample Artificially Produced by a Power Fluctuation.	40
19	Region Adjacent to Skin Suggesting Limited Eutectic Growth in a Y ₂ O ₃ Stabilized ZrO ₂ -Fe Sample.	43
20	Interior of Y ₂ O ₃ Stabilized ZrO ₂ -Fe Sample Showing Spherical Fe Particles After Solidification.	43
21	Poorly Formed Ni Fibers in a Y ₂ O ₃ Stabilized ZrO ₂ -Ni Sample.	44
22	Poorly Formed Co Fibers in a Y ₂ O ₃ Stabilized ZrO ₂ -Co Sample.	44
23	Longitudinal Section of UO _{2.14} - 10 Weight % W Rod Lowered at 32 cm/hr Showing Trapped Voids and Poor Growth Geometry.	47
24	Longitudinal Section of UO _{2.05} - 5 Weight T W Sample Showing Large Particles of Partially Dissolved W in Base of Molten Zone.	50
25	Longitudinal Section of UO _{2.03} - 5 Weight % W Sample Displaying Limited Banded Eutectic Growth.	50
26	Tungsten Solubility in Molten UO _{2+x} as a Function of O/U Ratio From Latta and Fryxell's Work.	51
27	Longitudinal Section of UO ₂ -W Composite Containing WO ₂ in the Premelting Composition, Table V Experiment No. 3-34a.	54
28	Longitudinal Section of UO ₂ -W Composite Containing WO ₃ in the Premelting Composition, Table V Experiment No. 3-34.	54

LIST OF ILLUSTRATIONS (Continued)

<u>Figure</u>	<u>Title</u>	<u>Page</u>
29	Typical Structure of Last Liquid to Solidify Showing U_xWO_3 in the Boundary Between UO_2 Grains.	55
30	Tungsten Dendrites Found Extensively in a UO_2 -W Sample Melted in a N_2 -CO Atmosphere, Table VI, Experiment No. 13-70.	55
31	Solidified Region of a UO_2 -Ta Sample Using a Ta Rod as the Metal Source. High Concentration of Ta Adjacent to Rod Appears Favorable for the Formation of an Oxide-Metal Lamellar Structure.	61
32	Transverse Section of UO_2 -Ta Sample Displaying Ordered Ta Fiber Growth and Extensive Microcracking of the Matrix.	61
33	Scanning Electron Micrographs of UO_2 -Ta Sample Etched to Remove the Ta Fibers. Note Extensive Microcracking of Matrix. a) Transverse Section, b) Longitudinal Section.	62
34	Longitudinal Section of UO_2 -Ta Sample Displaying Eutectic Growth and a Crack-Free Matrix.	64
35	Longitudinal Section of Nd_2O_3 -W Sample Displaying Poor Fiber Continuity.	68
36	Transverse(b) and (a) Longitudinal Sections of "Good" Fiber Growth in the System Nd_2O_3 - CeO_2 -Mo. This Type of Growth is Typical for All the CeO_2 Doped Rare Earth Metal Systems.	70
37	Longitudinal Sections Comparing the "Best" Fiber Growth Achieved in Nd_2O_3 -Mo Samples Without CeO_2 (a) With a Typical Sample Containing CeO_2 (b). (Note the Dramatic Improvement in Eutectic Structure.)	71
38	Longitudinal Sections of Nd_2O_3 - CeO_2 -Mo Samples Showing a) Areas of Primary Oxide ("Pothole" Structure) Seen if the System Is Oxide-Rich, and b) a W Dendrite Present in Metal-Rich Structures.	73
39	Increase in Co Lattice Parameter of Nd_2O_3 [Calculated From (0002) Planes] as a Function of CeO_2 Additions.	74

LIST OF ILLUSTRATIONS (Continued)

<u>Figure</u>	<u>Title</u>	<u>Page</u>
40	Transverse Sections of Nd ₂ O ₃ -CeO ₂ -Mo Samples Displaying Three Types of W Morphology. a) W Rod or Fiber Growth, b) W Platelet or Lammelar Growth, and c) Random W Triangular or "Bird Feet" Growth.	76
41	Longitudinal Section of Nd ₂ O ₃ -CeO ₂ -Mo Sample Showing Abrupt Change in Fiber Morphology Seen at Colony Boundaries.	77
42	SEM Photograph of Mo Fibers That Have Been Removed From the Nd ₂ O ₃ -CeO ₂ Matrix With Dilute HCl.	77
43	Entire Molten Zone of Nd ₂ O ₃ -CeO ₂ -Mo Sample Showing Regularly Spaced Bands Induced Through Periodic Power Fluctuations.	82
44	Higher Magnification View of the Band Induced Through a Power Fluctuation Shown in Figure 43.	83
45	Longitudinal Section of Nd ₂ O ₃ -CeO ₂ -Mo Sample Showing Narrow Band of Pure Oxide With Aligned Fibers Above and Below the Discontinuity. Also Note the Typical Cell or Colony Boundary.	83
46	A ZrO ₂ -W Sample Etched in Hot, Concentrated Phosphoric Acid for 17 Hours. Fibers Are Approximately 0.5 Microns in Length.	90
47	A ZrO ₂ -W Sample Etched in Hot, Concentrated Phosphoric Acid for 17 Hours. Fibers Are Approximately 4 Microns in Length.	90
48	A ZrO ₂ -W Sample Etched in Hot, Concentrated Phosphoric Acid for 17 Hours. Fibers Are Approximately 15 Microns in Length.	91
49	A HfO ₂ -W Sample Etched in Hot, Concentrated Phosphoric Acid for 22 Hours. Fiber Diameter is Approximately 0.15 Micron.	91
50	UO ₂ -W Specimen Etched to Point Tungsten Fibers. Fibers Are Approximately 4 Microns in Length.	94
51	UO ₂ -W Specimen Etched to Expose Fibers Without Affecting Fiber Shape. Fibers Are Approximately 17 Microns in Length.	94

LIST OF ILLUSTRATIONS (Continued)

<u>Figure</u>	<u>Title</u>	<u>Page</u>
52	UO ₂ -W Specimen Etched Using Two-Step Process to Produce Long, Sharply Pointed Fibers. Fibers Are Approximately 10 Microns in Length.	95
53	UO ₂ -W Specimen Etched Using Ultrasonic Vibrator. Etching Time of 10 Minutes and Fiber Length Approximately 89 Microns.	95
54	Nd ₂ O ₃ -Mo Sample Etched in 50% HCl for 15 Seconds.	96
55	Gold Vapor Deposit on Exposed Pin UO ₂ -W Sample.	103
56	Copper Sulfate Electrolysis Cell Using Either UO ₂ -W or ZrO ₂ -W Composites as the Anode.	108
57	Dark Field Reflected Light Micrographs of ZrO ₂ -W Sample 18-11, Slice 10, Used as Anode in a CuSO ₄ Electrolysis Cell.	110
58	UO ₂ -W Sample 13-52 Used as Anode in a CuSO ₄ Electrolysis Cell.	111
59	Sulfuric Acid Electrolysis Cell.	113
60	Electrolysis Current as a Function of Time for H ₂ SO ₄ Cell.	113
61	Three Photomicrographs Comparing a) Post Emission Damage, b) Cell Boundary Location, and c) Copper Electro-Deposits for Sample ZrO ₂ -W Sample 18-11, Slice 13.	115
62	Scanning Electron Micrographs of Copper Electro-Deposits on ZrO ₂ -W, Sample 18-11, Slice 13.	117
63	Overall View of the Experimental Apparatus.	120
64	Scanning Electron Micrograph of UO ₂ -W Sample 13-45/11-13 With Recessed Pins Showing Non-Uniform Pin Etching and Post Emission Damage.	125
65a	Section of a Simplified Recessed Pin Type Emitter Showing Origin of Components of Matrix Resistance.	127
65b	Approximate Lumped Parameter Model of Emitter Pins and Oxide Matrix.	127

LIST OF ILLUSTRATIONS (Continued)

<u>Figure</u>	<u>Title</u>	<u>Page</u>
66	Micrographs of ZrO ₂ -W Sample 18-11/13 Showing Correlation of Arc Damage with Pin Continuity. a) Post Emission Micrograph Showing Arc Damage, and b) Micrograph After Immersion in CuSO ₄ Electrolytic Cell.	131
67	Pre-Emission Scanning Electron Micrograph of Sample No. 13-57/13-65 (UO ₂ -W).	134
68	Pre-Emission Scanning Electron Micrographs of Sample No. 13-57/11-31c (UO ₂ -W), a) View of Sample Showing Long Exposed Pins Near Edge, b) Interior of Sample.	135
69	High Field Electron Emission Current Density for Two Different UO ₂ -W Samples. Anode-to-Cathode Spacing 0.030-Inch Both Cases.	137
70	Field Emission Current Density as a Function of Time for UO ₂ -W, Sample 13-57/11-31c.	138
71	Post Emission Scanning Electron Micrographs of Sample 13-57/11-31c (UO ₂ -W). a) Overall View of Sample Showing Areas of Arc Damage, b) High Magnification View of Arc Damage Areas.	139
72	Prolate Spheroidal Model.	145
73	Oblate Spheroidal Model.	145
74	Geometry for Test Problem.	155
75	Comparison of Numerically Calculated (a) and Exact (b) Solutions on a Typical Plane Parallel to the x-y Plane	157

LIST OF TABLES

<u>Table</u>	<u>Title</u>	<u>Page</u>
I	INDUCTION MELTING BEHAVIOR OF SINGLE AND BINARY OXIDE COMPOUNDS	10
II	INDUCTION MELTING BEHAVIOR OF OXIDE MIXTURES	12
III	FIBER SIZE, DENSITY, COMPOSITION AND GROWTH RATE DATA FOR ZrO_2 - 10 MOLE % Y_2O_3 -W SAMPLES	33
IV	THE RESULTS OF UO_2 -W COMPOSITE GROWTH USING $UO_2.03$ AND VARYING W ADDITIONS	48
V	THE RESULTS OF UO_2 -W COMPOSITE GROWTH USING $UO_2.03$ AND $UO_2.14$ MIXTURES AND WO_2 AND WO_3	53
VI	THE RESULTS OF UO_2 -W COMPOSITE GROWTH IN VARIOUS ATMOSPHERES (OXYGEN POTENTIALS)	57
VII	SUMMARY OF ATTEMPTS TO ARTIFICIALLY INDUCE INTERRUPTED (BANDED) FIBER GROWTH IN Nd_2O_3 - CeO_2 -Mo SAMPLES	81
VIII	CHEMICAL TREATMENT AND ELECTRICAL RESISTIVITY FOR ZrO_2 -W, SAMPLE NO. 18-11	105
IX	CHRONOLOGICAL SUMMARY OF EMISSION MEASUREMENTS	123
X	FIELD EMISSION FUNCTION	160

FOREWARD

This research was supported by the Advanced Research Projects Agency of the Department of Defense and was monitored by the U. S. Army Missile Command under Contract Number DAAH01-71-C-1046.

"The views and conclusions contained in this document are those of the authors and should not be interpreted as necessarily representing the official policies, either expressed or implied, of the Advanced Research Projects Agency or the U. S. Government."

ABSTRACT

During the last two years work has been underway developing melt-grown oxide-metal composite structures for electron emission testing. Prior to this report period extensive composite growth consisting of an array of metallic fibers uniformly distributed in an oxide matrix had been achieved only in the system UO_2 -W. In this report period well grown oxide-metal composite structures have been obtained in the systems Y_2O_3 stabilized ZrO_2 -W, Y_2O_3 stabilized HfO_2 -W, UO_2 -Ta, and the rare earth oxides (Gd_2O_3 , Nd_2O_3 or La_2O_3)-Mo or W. Metallic fiber densities in these systems have been varied between 7 to 70 million per cm^2 . Attempts to solidify magnetic metal (Fe, Co or Ni) fibers in some of these oxides has only met with limited success.

The importance of the stoichiometry of the molten oxide on metal solubility was established in the system UC_2 -W and exploited in the rare earth oxide-metal systems (through doping with CeO_2) to achieve uniform composite structures and mechanically sound samples. Minor input power fluctuations were conclusively shown to be a major cause of discontinuous (banded) fiber growth. Selective chemical etching studies successfully exposed the tungsten fibers in stabilized ZrO_2 and HfO_2 -W specimens. A two-step etching procedure was used to sharpen just the tips of W fibers in UO_2 -W samples. The metallic W and Mo fibers were successfully "harvested" from the rare earth oxide-metal composites.

A variety of contact and cleaning approaches were tested to achieve "good" electrical contact with the small metallic pins of the composite structures, and the lowest resistivity values measured to date on oxide-metal samples (parallel to the fibers) are reported. Electrochemical deposition studies were initiated, primarily to determine fiber continuity but also as an approach to deposit various materials on the ends of the individual fibers.

The initial electron emission testing of a ZrO_2 -W sample is reported. Many UO_2 -W samples containing different pin geometries with various anode configurations were tested in a field emission diode assembly. A UO_2 -W sample with very long exposed W fibers was run for 300 hours at a current density of 50 mA/cm^2 with current variations of less than 10%. This same sample displayed a maximum current density of 200 mA/cm^2 before vacuum arcing occurred. A theoretical analysis of the electron emission expected from an array of pins is being calculated using a numerical analysis of a three-dimensional model. A sample calculation for a single pin is presented.

SECTION I

INTRODUCTION

This is the fourth report describing research performed on the "Melt-Grown Oxide-Metal Composites" Project, ARPA Order Number 1637, and also the Annual Technical Report for Contract DAAH01-71-C-1046, covering the report period 10 June 1971 through 9 June 1972. The information contained in this Report will emphasize work accomplished since the Semi-Annual Report¹, although some of the earlier information will be repeated to provide informational continuity. Previous reports^{2,3} contained a description of the modified floating zone technique employed during the growth of the oxide-metal composite structures containing many millions of less than 1 micron diameter metallic fibers per cm^2 uniformly embedded in an oxide (insulating or semi-conducting) matrix. A brief description of the growth technique will be included again, as it provides valuable background information for interpreting the various sections of this Report. The major research objectives in the different project areas are also outlined in this section.

A modified floating-zone technique is used to grow oxide-metal composites. In this technique pressed rods of the oxide-metal mixture are sintered inside rf heated molybdenum tubes in an inert atmosphere to densify and preheat the material. A schematic diagram of the growth facility is shown in Figure 1.

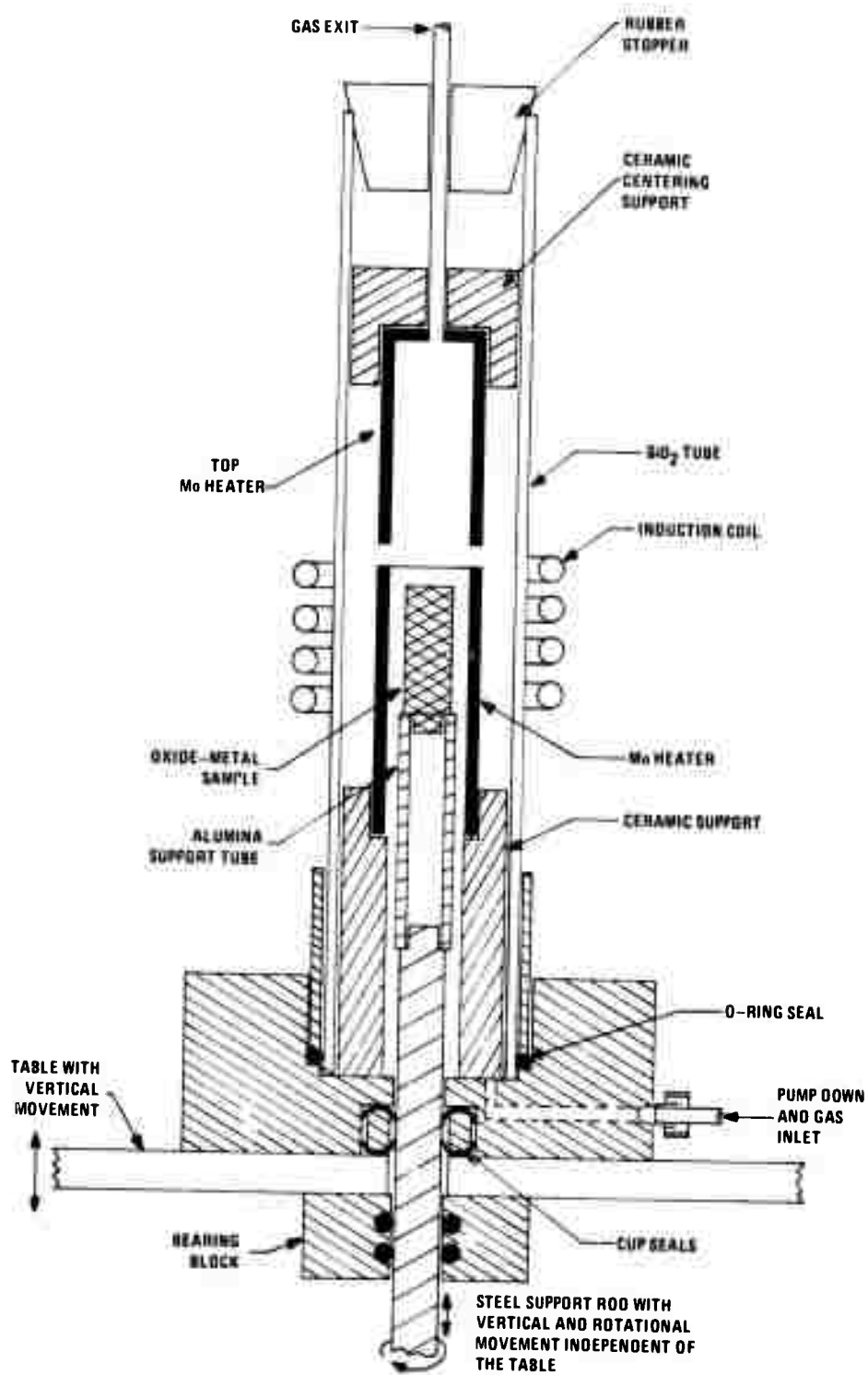


Figure 1. Schematic Diagram of the Facility for the Growth of Oxide-Metal Composites.

After the initial heating, which also serves to increase the electrical conductivity of the oxides, the molybdenum tube heaters are separated to expose approximately 2 cm of the rod to an rf field normally between 3 to 5 megahertz (MHz). Often only a single Mo preheater is used, and in this configuration the Mo tube is simply lowered out of the coil to expose the sample to the rf field. The concurrent increase of temperature, electrical conductivity and resistance heating continues until the interior of the rod melts at temperatures up to 3000°C. The high radiant heat loss from the surface and the inherent low thermal conductivity of the oxides maintains the skin of the rod well below the eutectic temperature of the mixture. The solid skin acts as a crucible to contain the molten zone. Composite growth is obtained by moving the molten zone up through the rod. In practice a cavity is generated in the molten zone because of the difference in density between the initial polycrystalline rod and solidified composite. During growth the oxide and metal melts from the roof of this cavity and solidifies at the base.

The primary technical objective of this study is to understand the growth processes leading to coupled growth and ordered microstructures during the solidifications of refractory oxide-metal mixtures, and to successfully produce useable samples of these composites and evaluate their potential for electronic applications, with the initial emphasis on electron field emission. The research program is divided into five areas to meet these objectives. These areas have been modified somewhat

since the last report³ primarily because of the increased effort to explore additional applications besides electron emission for these materials. Also, because of the success in developing a spectrum of oxide-metal systems exhibiting ordered structures, less effort has been expended looking for additional new systems. The structural and chemical characterization information pertinent to the various samples is included along with the growth data to provide more reporting continuity. To reflect these changes the section entitled "Structural and Chemical Characterization of Oxide-Metal Composites" presented in previous reports has been replaced by a section on "Oxide-Metal Composite Properties." The work underway in the five major research areas is briefly outlined below:

A. INDUCTION COUPLING AND SOLIDIFICATION BEHAVIOR OF OXIDES AND OXIDE-METAL MIXTURES

A study of the chemical, thermal, electrical and mechanical variables active during the solidification of numerous induction melted oxides and oxide-metal mixtures is in progress to interpret and understand the parameters that control the successful growth of oxide-metal composites. Various techniques including doping, higher sample densification and higher preheat temperatures have been used to increase the number of oxide materials that can be internally melted by induction heating. During this report period eutectic growth has been achieved using rare earth oxides with both W and Mo. Some of the factors controlling metal solubility in molten oxides have been explored and the causes of discontinuous eutectic growth investigated.

B. FORMATION OF OPTIMUM EMITTING ARRAYS

Selective chemical etching studies are in progress to expose as well as remove the metallic pins from the oxide-metal composites to obtain structures of interest for electron emission testing. The development of a sequential etching technique yielding sharpened W pins of variable length and the success of selectively removing the matrix from stabilized ZrO_2 and HfO_2-W samples are reported.

C. OXIDE-METAL COMPOSITE PROPERTIES

Work in this area is designed to explore any and all properties of these materials which are unique and potentially useful for applications. Presently the electrical resistivity is being measured and techniques to make "good" electrical contact to the very small metallic fibers is under investigation. Electro-chemical deposition experiments designed to measure the pin continuity are also described.

D. EXPERIMENTAL EMISSION MEASUREMENTS

The electron emission performance of oxide-metal composites is being evaluated in a diode structure as a function of array geometry and such electrical variables as field strength and interelectrode spacing. Emission measurements are conducted under carefully controlled conditions so that the onset of physical damage to the emitter structure can be determined. Current densities double that reported previously.

have been obtained; however, vacuum breakdown continues to limit emission current to several hundred milliamps per cm^2 .

E. THEORETICAL ANALYSIS OF ELECTRON EMITTING ARRAYS

In previous work two-dimensional analyses of the effects of the different array geometries on emission current have been considered. Using a numerical approximation, the realistic three-dimensional case is being analyzed and had progressed to the extent of determining the emission from a single pin of spheroidal geometry.

SECTION II

INDUCTION COUPLING AND SOLIDIFICATION BEHAVIOR OF OXIDES AND OXIDE-METAL MIXTURES

This section is subdivided into three subsections as follows: A) Induction Coupling and Melting Behavior of Oxide Systems, B) Solidification Behavior of Oxide-Metal Systems, and C) Electron Beam Melting and Solidification of Oxide-Metal Systems. These subsections cover investigations designed to develop new oxide systems that are capable of being internally melted by high frequency induction heating, attempts to combine these oxides with refractory metals to form useful oxide-metal composite structures, and the initiation of research into the use of an electron beam zone refiner to investigate oxide-metal systems that cannot be internally melted by direct induction heating.

A. INDUCTION COUPLING AND MELTING BEHAVIOR OF OXIDE SYSTEMS

Melting and subsequent controlled solidification of refractory oxides and oxide-metal mixtures have been previously accomplished¹⁻³ using high (4 to 30 MHz) frequency rf heating. This technique is limited to systems that have sufficient electrical conductivity at elevated temperatures to support eddy current heating at the level required to produce internal melting.

During this contract period a number of oxides, binary oxide compounds and oxide mixtures have been tested to determine their suitability for internal melting using the rf coupling scheme. A compilation of the test results including preheat temperatures, rf coupling and melting behavior and miscellaneous comments for the three classes of materials - oxides, oxide compounds and oxide mixtures - are presented in Tables I and II. Sample preparation and testing were carried out in the manner previously described¹⁻³ except as noted in the Tables.

Of the single and binary oxide compounds tested (Table I), Nd_2O_3 was the most promising candidate for composite structures. Although La_2O_3 was not tested, it should be noted that it was successfully internally melted by rf coupling when mixed with metal powders (see Section II-B-4). It appears that TiO_{2-x} is the next best oxide compound for use in composite structures. The addition of 5 weight % of -325 mesh titanium metal seems to have retarded the outgassing of oxygen resulting from the change in stoichiometry. The metal addition changed the color of the titania suboxide from white to black. Microscopic examination of a polished cross section did not reveal the presence of a metallic phase. However, under bright field illumination, three oxide phases were observed: a matrix composed of light and dark blue grains and orange colored platelets.

Of the oxide mixtures tested (Table II), HfO_2 + 10 mole % CaO and ZnO + 20 mole % Nb_2O_5 were the only ones to form a stable molten zone. However, they both suffer from other problems.

During melting of the HfO_2 -CaO mixtures, a reddish-brown substance was deposited on the quartz atmosphere tube of the growth system which prevented accurate temperature measurements. This problem may be related to the formation of a compound between the two components of the mixture or between the components and the glassy carbon preheat tube. The $\text{ZnO-Nb}_2\text{O}_5$ eutectic mixture containing 30 mole % Nb_2O_5 (melting point 1285°C) was unsuccessfully tested earlier². This two component system has another eutectic composition occurring at approximately 20 mole % Nb_2O_5 (melting point 1308°C). As indicated in Table II, this second eutectic was easily internally melted; but, because of the low melting temperature, the surface of the pellet did not emit enough thermal energy to remain solid and contain the molten zone. This eutectic mixture may have potential for developing low temperature oxide-metal composites if the molten zone can be contained by using a lower rf frequency or by cooling the external surface of the sample.

It should be pointed out that although HfO_2 - Y_2O_3 mixtures could not be internally melted, it was found that the addition of tungsten metal powder to this system increased its electrical conductivity enough to allow internal molten zones to be formed by rf coupling (Section II-B-1). The addition of CeO_2 to Nd_2O_3 made the normally easy to induction melt Nd_2O_3 form an unstable molten zone, and the sample cracked on cooling.

Based on the experimental results observed during this report period, it appears that because of rf arcing problems

TABLE I

INDUCTION MELTING BEHAVIOR OF SINGLE AND BINARY OXIDE COMPOUNDS

Oxide	Preheating OC	Type Susceptor	Frequency (MHz)	Atmosphere	rf Coupled/Melted	Comments or Problems
CaO·ZrO ₂	1600	Mo	3.8	H ₂ -N ₂	No	No Cracked on cooling.
Nd ₂ O ₃	1900	Mo	3.8	H ₂ -N ₂	Yes	Yes Formed stable molten zone.
NiO·TiO ₂	1300	Mo	3.8	N ₂	Yes	Yes Top of pellet "popped off" due to release of oxygen from liquid.
NiO·(1+x)TiO ₂	1300	Mo	3.8	N ₂	Yes	Yes Increasing the TiO ₂ to NiO ratio indicated that excess TiO ₂ (10 wt.%) reduces but does not eliminate out-gassing problem.
NiO·TiO _{2-x}	1300	Mo	3.8	N ₂	Yes	Yes Addition of 5 wt.% Ti metal reduced the stoichiometry of sample to the extent that nickel metal was precipitated.
NiO·TiO ₂	1300	Mo	3.8	N ₂	Yes	Yes A hole drilled halfway down through a pressed pellet was quickly closed by molten material when a molten zone formed.
ThO ₂	1900	Glassy Carbon	7.6	H ₂ -N ₂	No	No Broke up during cooling.

TABLE I (Continued)

Oxide	Preheating OC	Type Susceptor	Frequency (MHz)	Atmosphere	Coupled/Melted	Comments or Problems
Ti _{0.2-x}	1100	Mo	3.8	N ₂	Yes	Yes A 5 wt.% addition of titanium metal appears to have eliminated the stoichiometry outgassing problem in this system.
Y ₂ O ₃	1800	Mo	3.8	H ₂ -N ₂	Yes	No Broke up on cooling.
Y ₂ O ₃	1800	Mo	3.8	N ₂	Yes	No Broke up on cooling.
Y ₂ O ₃	1650	Mo	7.6	H ₂ -N ₂	Yes	No Came closer to internal melting than samples run at 3.8 MHz.

TABLE II

INDUCTION MELTING BEHAVIOR OF OXIDE MIXTURES

Oxide* Mixture	Preheating OC	Type rf Susceptor	Frequency (MHz)	Atmosphere	Coupled/Melted	Comments or Problems
Cr ₂ O ₃ +40% (ZrO ₂ +5%CaO)	1575	SiC	32	Air	Yes	Only small molten zones were formed. Coupling was unstable, and molten zones were lost after a very short time (~30 sec.)
Cr ₂ O ₃ +20% (ZrO ₂ +5%CaO)	1580	SiC	32	Air	Yes	Same as above.
HfO ₂ +10%CaO	1540	SiC	32	Air	Yes	No
HfO ₂ +10%CaO	1650	Glassy Carbon	32	N ₂	Yes	No
HfO ₂ +10%CaC	1810	Glassy Carbon	7.6	N ₂	Yes	Almost internally melted.
HfO ₂ +10%CaO	(Approx. 1850)	Glassy Carbon	7.6	H ₂ -N ₂	Yes	Reddish deposit formed on inside of quartz tube which prevented accurate temperature measurement. Stable internal molten zone formed.
HfO ₂ +10%CeO ₂	1560	SiC	32	Air	Yes	No

TABLE II (Continued)

Oxide* Mixture	Preheating OC	Type Susceptor	Frequency (MHz)	Atmosphere	Coupled/Melted	Comments or Problems
HfO ₂ +10%CeO ₂	1970	Mo	3.8	H ₂ -N ₂	-	Reacted with preheat tube. Area in contact with Al ₂ O ₃ support rod melted.
HfO ₂ +15%Y ₂ O ₃	1600	SiC	32	Air	Yes	NC
HfO ₂ +9wt%Y ₂ O ₃	1950	Mo	3.8	H ₂ -N ₂	Yes	No
Nd ₂ O ₃ +20%CeO ₂	1700	Mo	3.8	H ₂ -N ₂	Yes	Unstable molten zone, sample cracked on cooling.
Y ₂ O ₃ +10wt% CaCO ₃	1800	Mo	3.8	H ₂ -N ₂	Yes	No
Y ₂ O ₃ +4wt%SrCO ₃	1850	Mo	3.8	H ₂ -N ₂	Maybe	No
Y ₂ O ₃ +10wt%ZrO ₂	1850	Mo	3.8	H ₂ -N ₂	Yes	No
ZnO+20wt%Nb ₂ O ₅	1250	SiC	23	Air	Yes	ZnO did not sublime, but because of this eutectic's low melting point the molten material melted through the pellet's walls.

*Oxide additions are in mole % unless otherwise indicated.

the best method of improving the coupling efficiency of oxides and oxide mixtures is to decrease the rf frequency and utilize higher preheat temperatures to obtain the required electrical conductivity to support eddy current heating.

B. SOLIDIFICATION BEHAVIOR OF OXIDE-METAL SYSTEMS

The research included in this subsection was designed to improve and interpret the growth of oxide-metal eutectic structures in systems capable of being internally melted by rf heating. Prior to this contract period, only the growth of UO_2 -W samples had been controlled well enough to warrant electron emission testing.

During this contract period a number of major accomplishments have been achieved in the growth of metal fibers in oxide matrices. These are: 1) the ordered growth of W fibers in a stabilized HfO_2 matrix; 2) extensive ordered growth in the stabilized ZrO_2 -W system and the electron emission testing of this material; 3) demonstration that the oxygen-to-uranium (O/U) ratio of the oxide controls the solubility of W in molten UO_2 and that this behavior is a dominant factor controlling composite growth in the UO_2 -W system; 4) the initial growth of extensive areas of Ta fibers in UO_2 -Ta samples; 5) the growth of well ordered Mo and W fibers in several rare earth oxide mixtures (Gd_2O_3 -CeO₂, La_2O_3 -CeO₂ and Nd_2O_3 -CeO₂) the entire length of molten zone travel; 6) the limited growth of magnetic

metal fibers (Fe, Ni, Co) in various oxides; and 7) the determination and control of some of the parameters which have caused discontinuous fiber growth.

This subsection is subdivided into four major areas based on the oxide matrix materials.

1. Stabilized $\text{HfO}_2\text{-W}$

The success of rf melting HfO_2 stabilized with CaO (see Table II) suggested that this oxide is suitable for satisfactory oxide metal structures employing $\text{HfO}_2\text{-CaO-W}$ mixtures, and the subsequent improved structures obtained by substituting Y_2O_3 in place of CaO are described.

In the first successful internal melting of a stabilized $\text{HfO}_2\text{-W}$ mixture a hafnia pellet stabilized with 20 mole % CaO containing 6 weight % W was preheated in a $\text{H}_2\text{-N}_2$ atmosphere to 1850°C using a 7.6 MHz field and a vitreous graphite preheater. Both this pellet and a duplicate run of the same composition were difficult to control after melting because of a reddish-brown vapor deposit that coated the silica tube used to contain the $\text{H}_2\text{-N}_2$ atmosphere. In an effort to gain more control over the melt temperature and to improve the stability of the molten zone, another sample of the same composition was preheated to 1990°C using a molybdenum preheat tube and a rf frequency of 3.8 MHz. This procedure reduced the vapor deposits on the SiO_2 tube, and the sample readily melted; however, difficulty was encountered moving the molten zone through the pellet.

Examination of the $\text{HfO}_2\text{-CaO-W}$ samples melted using the 7.6 and 3.8 MHz rf fields revealed tungsten dendrites (Figure 2) in some areas of the solidified oxide; however, no ordered oxide-metal structures were observed. Isolated fibers (Figure 3) were observed in another pellet of the same composition that was preheated to 2000°C and melted using a 3.8 MHz field. In addition, portions of the matrix appeared to consist of a two-phase oxide structure (Figure 4). This was not unexpected since both HfO_2 and W are capable of forming compounds with CaO. Increasing the tungsten content to 10 and 12.6 weight % improved the fiber structure only slightly (Figure 5), and the two-oxide phases were still present.

Even though previous attempts to couple to HfO_2 which was stabilized with ceria or yttria were unsuccessful (Table II), an attempt was made to melt these systems with a tungsten addition in the hope it would increase the electrical conductivity of the sintered pellets enough to allow direct rf melting. A pellet of hafnia stabilized with 10 mole % ceria which contained 9 weight % W did not couple well enough to internally melt when preheated to 1860°C in a $\text{H}_2\text{-N}_2$ atmosphere and exposed to a 3.8 MHz field. In a similar experiment where the hafnia was stabilized with 10 mole % yttria and contained 9.1 weight % tungsten, the pellet easily coupled well enough to create a molten interior after preheating to 1950°C . Figure 6 shows an area of good fiber growth from this sample which was lowered at a rate of 3 cm/hr. Typical areas of nonuniform solidification

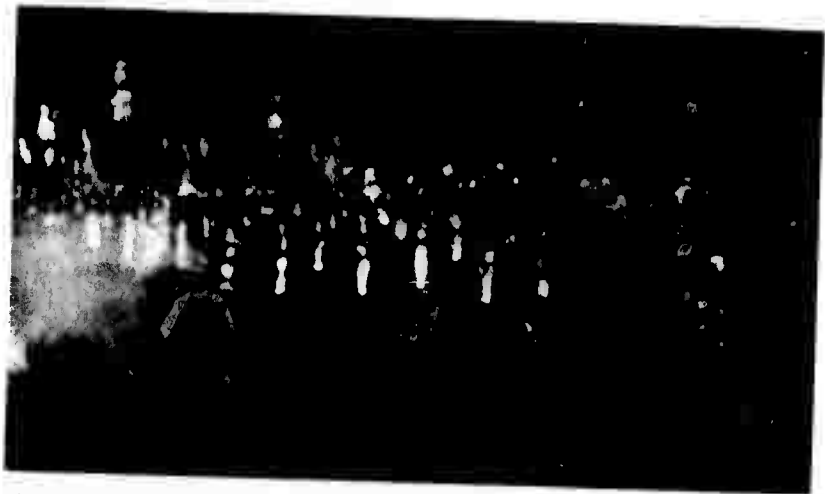


Figure 2. Dendritic W Growth in a Solidified HfO_2 - 20 Mole % CaO - 6 Weight % W Sample. Dark Field, X600.



Figure 3. Random W Fibers in a Solidified HfO_2 - 20 Mole % CaO -6 Weight % W Sample. Dark Field, X600.



Figure 4. Two-Phase Oxide Matrix Present in the CaO Stabilized HfO_2 - 6 Weight % W Sample. Bright Field, X600.

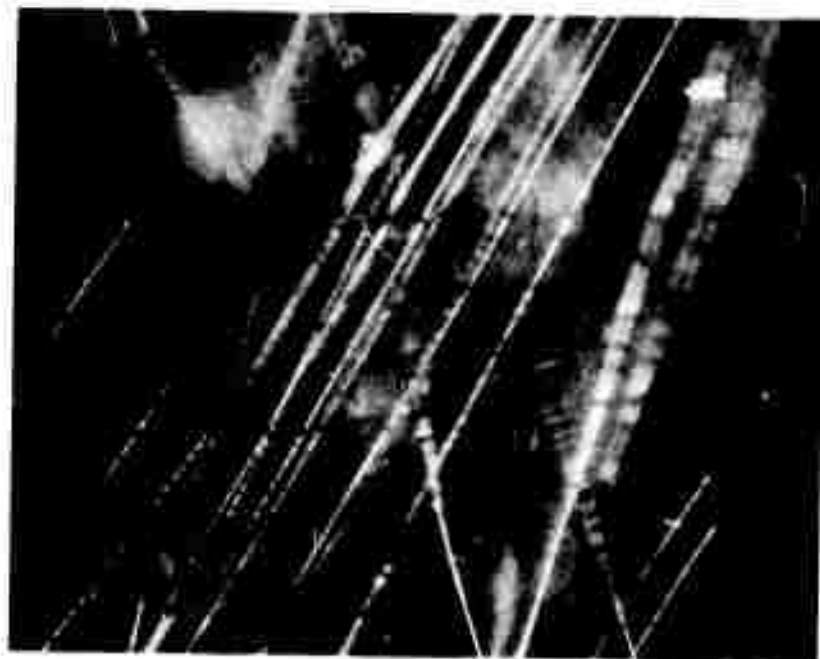


Figure 5. Poor Fiber Growth in a Solidified HfO_2 - 20 Mole % CaO - 12.6 Weight % W Sample. Dark Field, X600.



Figure 6. Good Eutectic Growth in a Solidified HfO₂ - 10 Mole % Y₂O₃ - 9.1 Weight % W. Dark Field, x600.

such as fiber banding and platelet formation are shown in Figure 7.

The banded structure in Figure 7a appeared to contain areas of primary oxide, suggesting a tungsten metal deficiency. To investigate this possibility a series of hafnia pellets stabilized with 10 mole % yttria containing 10.7, 12.3 and 13.8 weight % tungsten were internally melted in a H_2-N_2 atmosphere and solidified at 1 cm/hr. Examination of these samples revealed that primary oxide areas were still present (Figure 8) when 10.7 weight % tungsten was added. The 12.3% tungsten sample contained extensive areas of excellent fiber growth (Figure 9) with almost no primary oxide areas. Increasing the tungsten to 13.8% produced an excess metal condition as shown by the presence of primary metal in the form of dendrites (Figure 10).

Cracking has been a major problem in all the stabilized HfO_2-W samples described above. It is assumed that these cracks were formed as the result of the severe thermal gradients which the samples are subjected to during solidification and cooling to room temperature. Variations in the stabilizer-hafnia ratio and reduction of the thermal gradients through the use of a post-heater were investigated as possible means of reducing the development of cracks.

Figure 11 shows a typical cross section of a 10 mole % yttria stabilized pellet containing 12.3 weight % tungsten, which was lowered at 1 cm/hr with its normal room temperature crack pattern. Identically prepared samples containing 15 and



a) Banded Fiber Growth, X200.

Reproduced from
best available copy.



b) Platelet and Rod Growth. X600.

Figure 7. Nonuniform Solidification Areas in Y₂O₃ Stabilized HfO₂-W Samples. Dark Field.

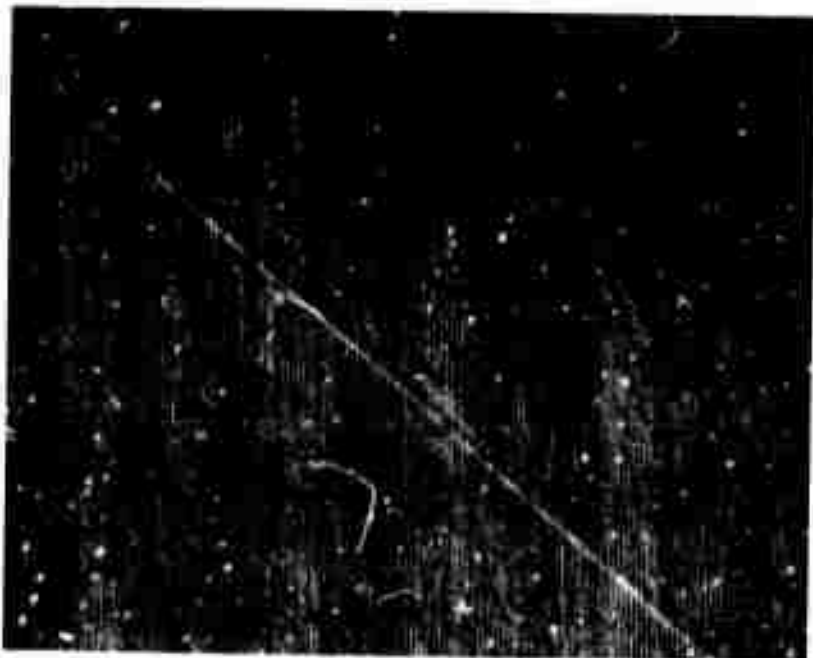


Figure 8. Primary Oxide Areas in Solidified HfO_2 - 10 Mole % Y_2O_3 - 10.7 Weight % W. Dark Field, $\times 600$.



a) Transverse Section

Reproduced from
best available copy.



b) Longitudinal Section.

Figure 9. Transverse and Longitudinal Sections of "Good" Fiber Growth in a Y_2O_3 Stabilized HfO_2 Sample to Which 12.3 Weight % W Was Added. Dark Field, X600.



Figure 10. Tungsten Dendrites and Areas of Fan Growth in Solidified HfO_2 - 10 Mole % Y_2O_3 - 13.8 Weight % W. Dark Field, X600.



Figure 11. Typical Cross Section of a Solidified HfO_2 - 10 Mole % Y_2O_3 - 12.3 Weight % W Pellet Showing Cracking Present. X2.5

20 mole % yttria additions were found to be cracked (Figure 12) to about the same degree as those containing 10 mole % yttria (Figure 11). Figure 13a shows an area from the 15 mole % yttria sample which exhibits an area of good growth, a band with no fiber growth, and then reinitiation of fiber growth with the formation of a colony wall where two growth zones intersect. A colony boundary intersecting the etched pellet surface normal to the growth direction is shown in Figure 13b.

The other approach to reduce cracking by reducing the thermal gradient to which the stabilized HfO_2 -W samples were subjected was accomplished by coupling to the pellet, establishing an internal molten zone, and then raising the molybdenum preheat tube back into the rf field. By properly controlling the rf power, it was possible to maintain the internal molten zone and raise the temperature of the molybdenum tube so that it increased the temperature of the solidified base of the sample thereby lowering the thermal gradients present in the pellet. After the pellet was lowered through the rf field (molten zone raised through the sample), the rf power was slowly decreased to slowly lower the temperature of the preheat tube to further reduce thermal stresses while the sample was cooled. However, the samples solidified using this technique did not appear to contain any fewer cracks than those subjected to the larger thermal gradients.

It is doubtful that additional work will be done on the solidification behavior in stabilized HfO_2 -W systems. The



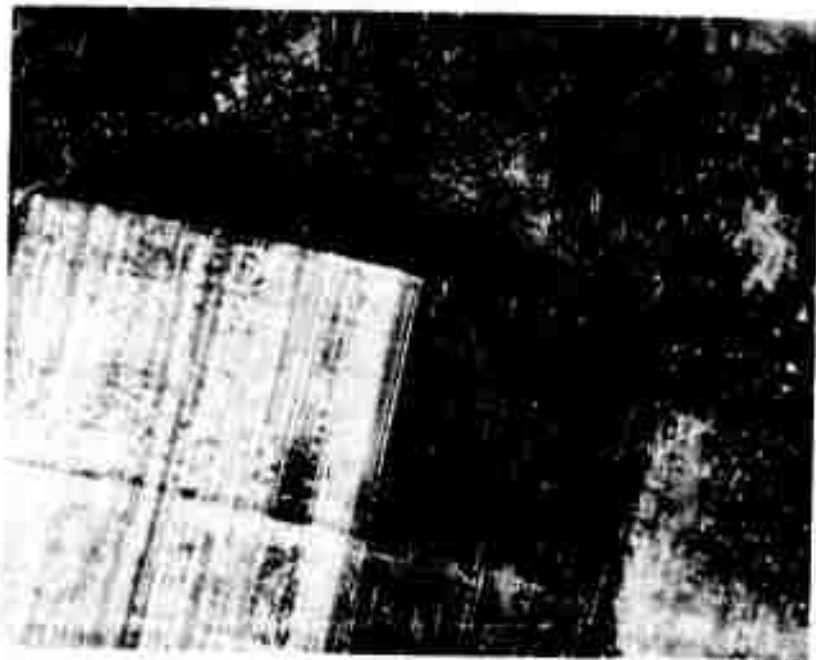
a) 15 Mole %
 Y_2O_3 .

Reproduced from
best available copy.

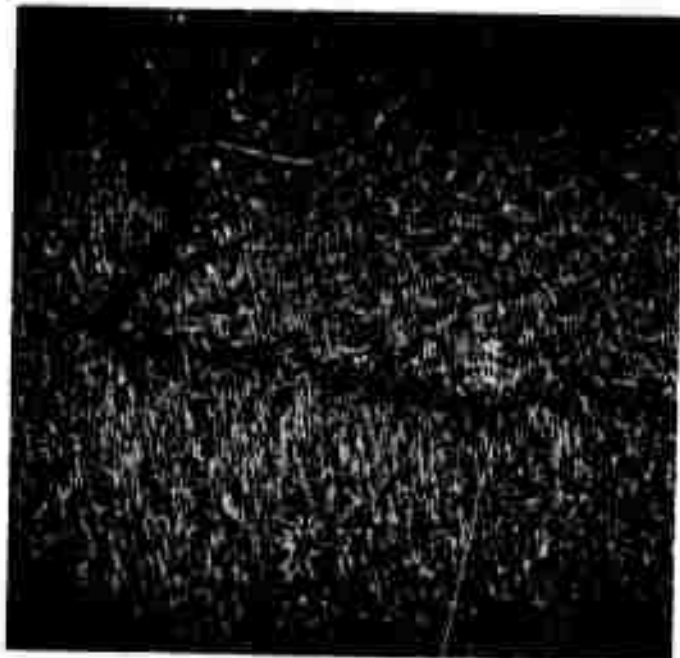


b) 20 Mole %
 Y_2O_3 .

Figure 12. Typical Cracking in Solidified HfO_2 Stabilized
With 15 and 20 Mole % Y_2O_3 and Containing
12.3 Weight % W. X2.5



a) Longitudinal
Section,
Dark Field,
X600.



b) Scanning Elec-
tron Micrograph
of Transverse
Section. Sample
Selectively
Etched to Expose
the Fibers. X655

Figure 13. Colony or Cell Boundaries Typically Observed in Y_2O_3 Stabilized $\text{HfO}_2\text{-W}$ Samples.

prevention of thermal cracking appears to be a formidable problem in these systems, and other oxide-metal systems (to be described in subsequent sections) exhibit improved oxide-metal eutectic growth and resistance to thermal failures.

2. Stabilized ZrO₂-W

The melt-growth of oxide-metal composites in the Y₂O₃ stabilized ZrO₂-W system has advanced to the point of producing uniform fiber growth throughout most of the solidified zone in many samples. This was achieved by lowering the rf frequency employed to melt the interior of the samples and the determination of the optimum additions of stabilizer and tungsten. Once good composite growth was achieved, the influence of growth rate, atmosphere, possible stabilizer segregation and WO₃ additions were investigated. An attempt to isolate the causes of discontinuous (banded) fiber growth in stabilized ZrO₂-W samples was also initiated.

a. Influence of rf Frequency

The frequency used to inductively heat stabilized ZrO₂-W rods has a great effect on the establishment of a stable internal molten zone. Frequencies used with ZrO₂-Y₂O₃-W mixtures were 16, 7.6, and 3.8 MHz. Initially the higher frequencies were used because only at these higher frequencies was it possible to establish eddy-current heating in this poorly electrical conducting system. With 16 MHz, ZrO₂-Y₂O₃ mixtures could be easily melted; but rf arcing and spilling of the molten zone (melting

through pellet skin) were problems. At 7.6 MHz the samples could also be melted, and arcing problems were reduced; however, there was difficulty establishing a power setting high enough to insure complete internal melting while still maintaining the integrity of the thin solid skin.

Improved coil-sample geometries and increased preheat temperatures have lead to the successful rf melting of ZrO_2 - Y_2O_3 -W mixtures at 3.8 MHz. At this frequency the increased rf penetration leads to a thick unmelted shell to contain the molten zone, and increased power assures complete internal melting. During typical experiments ZrO_2 - Y_2O_3 -W rods approximately 19mm in diameter were preheated and sintered at 1650 - $1700^\circ C$ in a H_2 - N_2 atmosphere using a molybdenum preheat tube. After being internally melted their skin temperatures were about $1870^\circ C$. (These are uncorrected, as-read optical temperatures obtained sighting directly on the Mo tube or oxide-metal rod.)

b. Determination of the Optimum Y_2O_3 and W Content

Variations in the amount of Y_2O_3 stabilizer and metal additions in the ZrO_2 - Y_2O_3 -W system have been studied to find compositions suitable for composite growth. Duwez, et.al.,⁴ report that ZrO_2 and Y_2O_3 form a cubic solid solution from 7 to 56 mole % Y_2O_3 at $2000^\circ C$. The Y_2O_3 addition is necessary to produce a cubic solid solution which does not have any disruptive crystal lattice changes. Pure ZrO_2 and ZrO_2 - Y_2O_3 mixtures with less than 7 mole % Y_2O_3 show a lattice transformation from monoclinic to tetragonal at about $1000^\circ C$, and a volume change

of about 9% which would cause severe cracking, especially during cooling.

An extensive series of experiments were run varying the tungsten content in samples containing 7.9 and 10 mole % Y_2O_3 . In samples containing 7.9 mole % Y_2O_3 the best tungsten content was approximately 10 weight % W. This produced a pellet with good fiber growth throughout most of the pellet except for the upper portion of the melted area which contained some areas of primary oxide. Additions of 5 weight % W produced much larger areas of primary oxide in the pellet. Additions of 15 weight % W produced W dendrites within the eutectic area and still contained primary oxide in the upper portion of the pellet.

Increasing the Y_2O_3 content to the 10 mole % level required the addition of 16 weight % W to achieve the best eutectic growth. Using 16 % W the pellets had larger areas containing good fiber growth than seen in pellets containing 15% W. Specifically, the upper portion of the solidified samples typically contained areas of primary oxide which disrupted the fiber growth. The areas containing these primary oxide regions were noticeably smaller, using 16% W instead of 15% W. When 17% W was used, dendrites of W occurred within the fiber areas. Figure 14 shows the effects of such dendrites on fiber growth. The fibers which were growing uniformly suddenly stop a short distance below the dendrite, as the growth of the dendrite depletes the metal content of the liquid. After the liquid-solid interface passed the dendrite and the W content of the



a) Bright Field.



b) Dark Field.

Figure 14. The Effect of a W Dendrite on Fiber Growth in a ZrO_2 - 10 Mole % Y_2O_3 - 17 Weight % W Sample. x600.

liquid increased, the fibers renucleated some distance above the dendrite producing uniform oxide-metal eutectic growth again.

The power necessary to maintain a stable molten zone was also effected by these slight changes in tungsten content. The power settings, for $ZrO_2-Y_2O_3-W$, to achieve good solidification were very critical and sensitive. It was found that a lower power input was necessary for 16% W mixtures than for either 15% or 17% W mixtures.

During stabilized ZrO_2 -W growth the composition of the solidified eutectic material does not remain the same as the initial starting mixtures. Table III tabulates along with other parameters the eutectic composition (in weight % W) calculated from fiber sizes and density counts taken from SEM micrographs of well grown areas of ZrO_2 - 10 mole % Y_2O_3 -W samples. To convert the volume percent W to weight percent, the theoretical density of tungsten, 19.3 gm/cm³, was used for the fibers. For the stabilized ZrO_2 matrix, 6.1 gm/cm³ was used. The density of the stabilized ZrO_2 was determined by x-ray methods and checked by direct measurement on a sample not containing any W. A typical density for the solidified portion of these composites was 6.3 gm/cm³. An error analysis on the composition calculations indicated the accuracy of these calculations to be about ± 2 weight %.

The information contained in Table III indicates the compositions of the solidified eutectics were between 4.2 and 9.8 weight % W, whereas the initial W contents were between 15 and 17%. This loss of tungsten can be explained by the formation and

TABLE III
FIBER SIZE, FIBER DENSITY, COMPOSITION AND GROWTH RATE
DATA FOR ZrO_2 - 10 Mole % Y_2O_3 -W SAMPLES

Sample Number	Weight % W Added	Growth Rate cm/hr	Fiber Diameter Microns	Fiber Density $\times 10^6$ Fibers/cm ²	Volume % Fibers	Calculated Eutectic Weight % W
6-80	15	0.34	0.95	-	-	-
18-57	15	1.06	0.74	7.6	3.3	9.8
6-67	15	1.75	0.52	12.5	2.6	7.9
18-67	16	1.94	0.47	14.5	2.5	7.6
18-59	17	2.17	0.45	12.3	1.9	5.9
6-82	15	2.59	0.40	10.8	1.3	4.2
18-70	16	3.62	0.31	31.8	2.4	7.3
18-74	16	5.87	0.22	48.7	1.9	5.8

vaporization of tungsten oxides and/or the vaporization of W. The silica tube in which the pellets were enclosed during melting normally became coated with a thick vapor deposit. This deposit was analyzed by x-ray diffraction, and found to contain WO_3 and WO_2 . The oxygen necessary for the oxidation of the W may come from the oxygen impurities in the N_2 atmosphere employed during routine growth. Another source of oxygen may be the slight reduction of the ZrO_2 . In all samples containing W, the ZrO_2 matrix was black. $ZrO_2-Y_2O_3$ pellets containing no tungsten were an amber-yellow color when melted in N_2 . $ZrO_2-Y_2O_3$ samples melted in a reducing H_2 atmosphere were black indicating sub-stoichiometry.

The depletion of some of the tungsten during growth also explains the regions of primary oxide often seen at the top of the solidified samples. If tungsten vaporizes directly or as WO_2 or WO_3 , eventually the tungsten content in the melt will be lower than the eutectic composition at which point primary oxide areas would appear. Apparently tungsten fiber growth is achieved by eutectic type solidification from a melt which is at first rich in tungsten in relation to the eutectic composition. If the initial tungsten composition is too high (17% or greater) some tungsten dendrites will be formed. As the solidification proceeds, the tungsten concentration is lowered by vaporization. When the liquid-solid interface is near the top of the pellet, the tungsten concentration is below the eutectic composition which causes solidification of primary oxide. The exact

compositions at which the tungsten dendrites and primary oxide would start forming is most likely effected by the degree of undercooling at the liquid-solid interface and the growth rate.

Variations in the growth atmosphere were tried to reduce the loss of tungsten during melting as well as the vapor deposits on the silica tube. These deposits prevent temperature readings with the optical pyrometer and visual observation of the sample. When an atmosphere of N_2 with about 20% volume H_2 was used, it reduced the deposit. The use of a pure H_2 atmosphere with samples containing 16% and 8% W lowered the fogging to a minimum, but the fiber area in both samples contained some tungsten dendrites like those seen in Figure 14.

c. Influence of Growth Rate

The effect of growth rate on the fiber size and density of a series of Y_2O_3 stabilized ZrO_2 -W samples is shown in Table III. Micrographs of two samples grown under identical conditions except for about a ten fold change in growth rate are shown in Figure 15. Figure 16 illustrates the effect of growth rate on fiber diameter. Another effect noted especially at the higher growth rates was a tendency for small voids to be left in the solidified area of the pellet. The void that is normally at the top of the pellet would sometimes not travel completely to the top with growth rates above about 5 cm/hr.



a) Growth Rate
0.51 cm/hr



b) Growth Rate
5.9 cm/hr

Figure 15. The Effect of Growth Rate on W Fiber Density in
 ZrO_2 - 10 Mole % Y_2O_3 % - 16 Weight % W Samples.
Dark Field, X600.

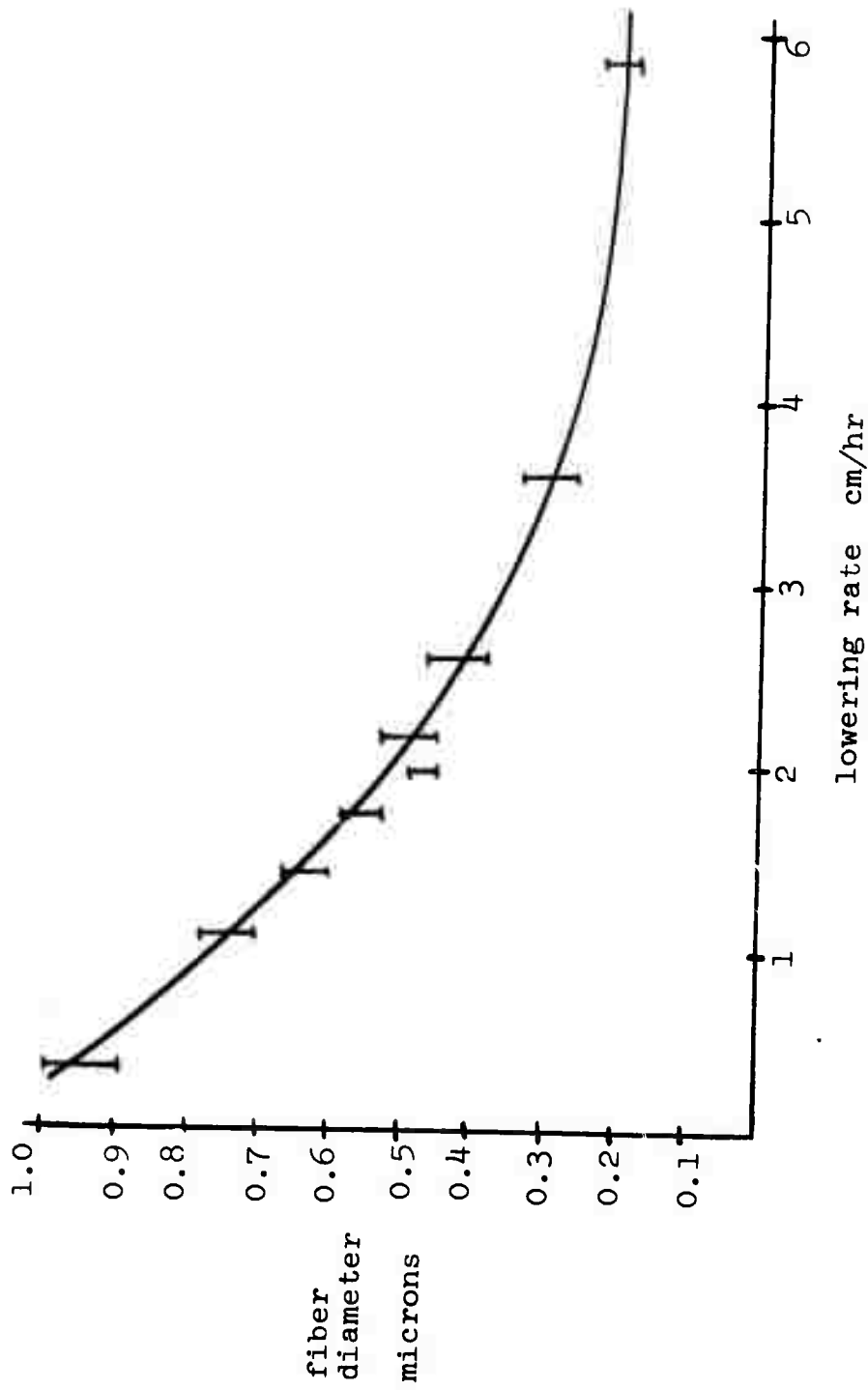


Figure 16. The Effect of Varying Growth Rate on the W Fiber Diameter in Y_2O_3 Stabilized ZrO_2 -W Samples.

d. Discontinuous (Banded) Fiber Growth

In addition to uniform continuous fiber structures, other types of interrupted structures have been observed and two different types have been identified. In the first type, Figure 17, the fibers are simply interrupted by a band of oxide a few microns thick. The fibers continue on the other side of the band just as if the discontinuity had never occurred. In addition a few of the fibers in this type area sometimes appear to cross the oxide band without interruption. Samples grown at very slow growth rates have many more of this type band than do those grown at faster rates.

The second type of banded structure, shown in Figure 18, exhibits a wide discontinuity consisting of particles of tungsten in the oxide after which the fibers appear to renucleate from a single point above the band and then fan out again to reform an ordered structure. This type banding was artificially produced by power fluctuations and is discussed in detail in the rare earth oxide-metal section (Section II-B-4).

e. Y_2O_3 Segregation

The potential segregation of the Y_2O_3 in a Y_2O_3 stabilized ZrO_2 sample was investigated by microprobe analysis. A solidified pellet of ZrO_2 stabilized with 10 mole % Y_2O_3 and containing no metal was cut in half longitudinally and scanned for yttrium both horizontally and vertically. There was no major segregation of the Y_2O_3 detected and the only variation noted was an increase of about 1% in Y_2O_3 content near the sides and bottom of the solidified region.

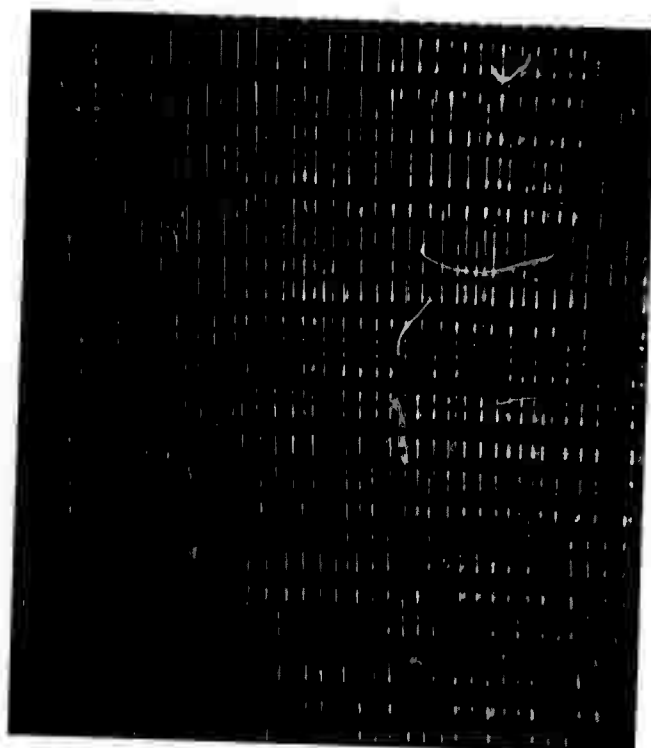
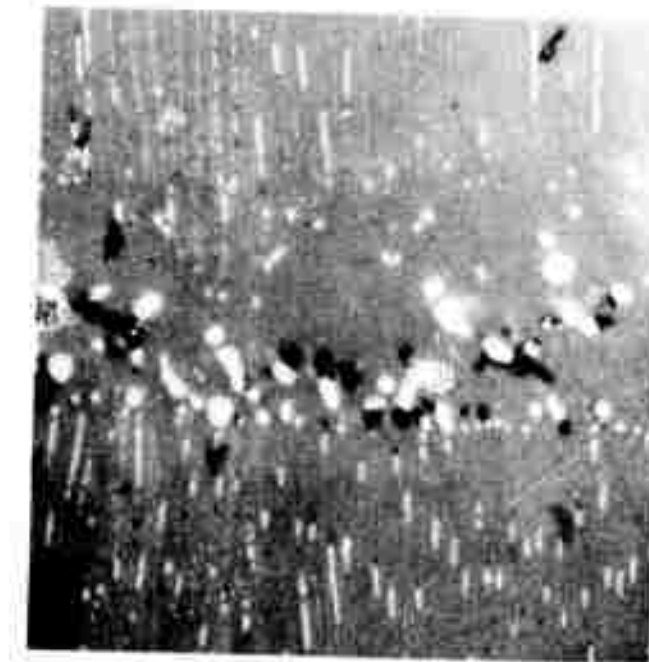


Figure 17. Discontinuous W Fibers in a ZrO_2 - 10 Mole % Y_2O_3 Sample in Which a Few Fibers Apparently Cross the Band. Dark Field, X600.



a) Bright Field.



b) Dark Field.

Figure 18. Wide Growth Discontinuity in Y₂O₃ Stabilized ZrO₂-W Sample Artificially Produced by a Power Fluctuation. X600.

f. Influence of WO_3 Additions

The favorable effect on oxide-metal eutectic growth obtained by oxide additions designed to increase the oxygen content of the liquid (CeO_2 in the rare earth oxide-metal systems and WO_2 or WO_3 in the UO_2 -W system to be described in subsequent sections) led to the addition of WO_3 to ZrO_2 - Y_2O_3 -W samples. In one sample a 1 weight % addition of WO_3 and adjustments in the tungsten addition to keep the total tungsten content at 16% were made. The only difference seen from the normal growth in samples not containing WO_3 was slightly more primary oxide at the top of the solidified zone. In another pellet 2 weight % WO_3 was added in the same manner. This resulted in very poor fiber growth with many tungsten droplets present. Apparently much of the tungsten had not gone into solution in the molten ZrO_2 , and consequently it was concluded that the fiber growth in ZrO_2 - Y_2O_3 -W system probably cannot be improved by chemical additions of oxygen in the form of WO_3 .

g. Stabilized ZrO_2 -Fe, Ni and Co

A series of runs were performed using Fe, Ni and Co as the metal addition to Y_2O_3 stabilized ZrO_2 . These metals are of interest because of their magnetic properties and the prospect of achieving aligned single crystal metallic fibers which approach domain size. To date this work has met with very limited success as only isolated areas of ordered oxide-metal eutectic structures have been found in these systems.

Several ZrO_2 samples stabilized with 10 mole % Y_2O_3 and containing 10 and 20 weight % Fe were inductively melted in a H_2-N_2 atmosphere. The rod was lowered in the conventional manner to move the molten zone through the rod; however, the rod appeared to remain entirely molten until most of the sample was below the rf coil, at which time it completely decoupled and rapidly solidified. Many attempts to control the zone using a Mo postheater were unsuccessful, as a delicate balance of power was required to prevent spills of the molten zone and to maintain the molten sample with the Mo tube in the rf coil. Figure 19 shows a narrow region adjacent to the unmelted skin of a Y_2O_3 stabilized ZrO_2 -Fe sample where limited coupled growth was found radiating from the skin and orientated perpendicular to the growth direction. The remainder of the molten zone contained spherical shaped Fe particles, as shown in Figure 20.

In ZrO_2 samples containing 5 weight % Ni, small regions of discontinuous Ni fibers were found adjacent to the unmelted skin, and this growth was also aligned perpendicular to the growth direction (Figure 21). No Ni metal was evident in the interior of the molten zone; the majority of the metal was present in a large sphere at the base of the solidified region.

A series of ZrO_2 samples containing 10 weight % Co were solidified in the conventional manner, and only in isolated locations across the samples were areas of aligned Co fibers and beads found (Figure 22). In contrast to the Fe and Ni growth the Co fiber structures were parallel to the lowering direction. Much of the solidified ZrO_2 was a blue color typical

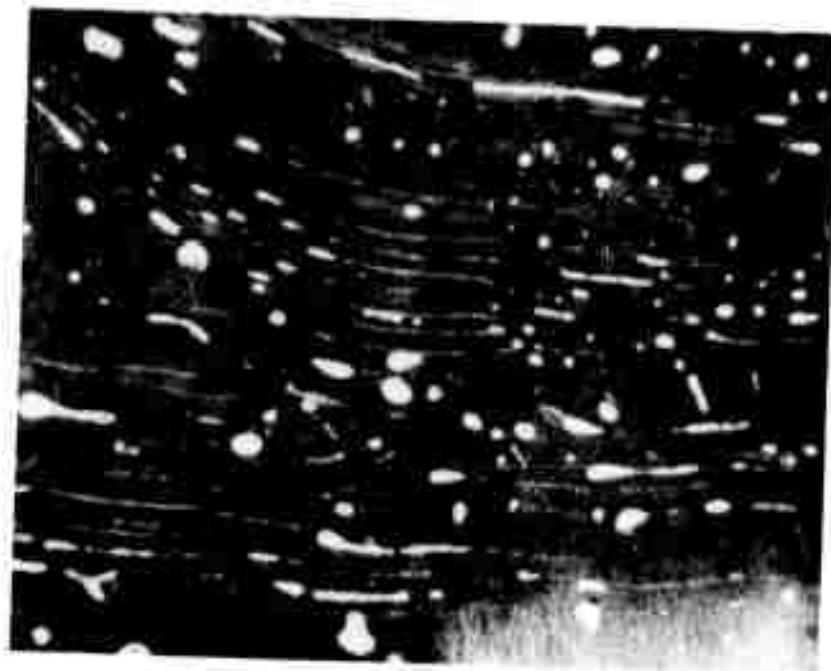


Figure 19. Region Adjacent to Skin Suggesting Limited Eutectic Growth in a Y_2O_3 Stabilized $\text{ZrO}_2\text{-Fe}$ Sample. Bright Field, X600.

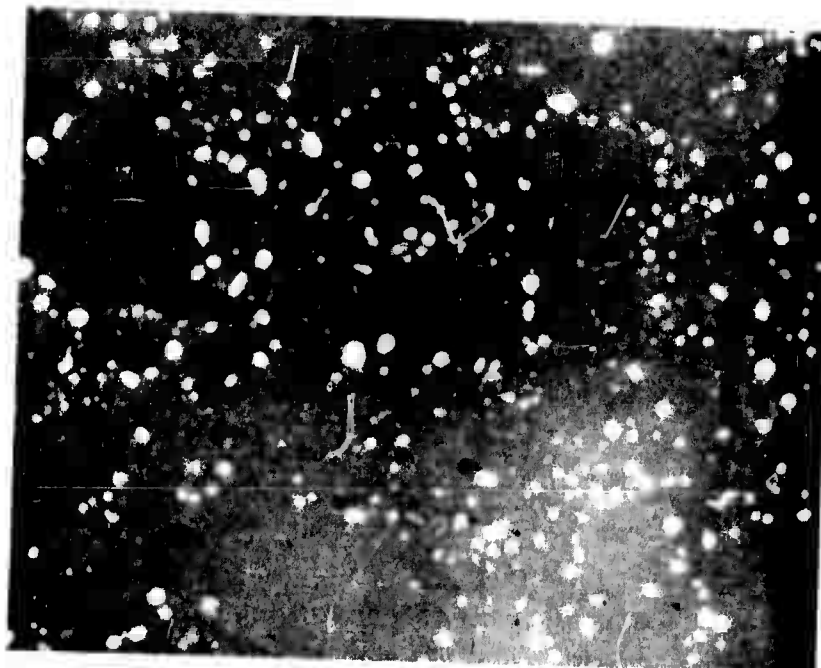


Figure 20. Interior of Y_2O_3 Stabilized $\text{ZrO}_2\text{-Fe}$ Sample Showing Spherical Fe Particles After Solidification. Bright Field, X600.



Figure 21. Poorly Formed Ni Fibers in a Y_2O_3 Stabilized $\text{ZrO}_2\text{-Ni}$ Sample. Dark Field, X600.



Figure 22. Poorly Formed Co Fibers in a Y_2O_3 Stabilized $\text{ZrO}_2\text{-Co}$ Sample. Dark Field, X600.

of coloring caused by cobalt oxide in glass.

Some preliminary experiments employing the complete or partial replacement of the metals Fe, Ni and Co with their oxides Fe_2O_3 , NiO , and CoO have been run in hopes of increasing the solubility of the metals in molten ZrO_2 . Extensive vaporization of the metal oxides has made it difficult to prepare well melted samples. It appears at present using a less refractory (lower melting) oxide matrix than ZrO_2 is the best approach for producing oxide-metal eutectic structures containing magnetic metals.

3. UO_2 -Metal

a. UO_2 -W

During the present work in the growth of oxide-metal composites in the system UO_2 -W, it has become increasingly evident that the oxygen-uranium (O/U) ratio of the oxide is a dominant factor controlling successful composite growth. In this subsection a series of experiments are outlined which clearly demonstrate the importance of the O/U ratio on the solubility of W in molten UO_2 . The subsequent efforts to maintain sufficient W solubility in molten UO_2 for good composite growth through the use of WO_2 and WO_3 additions as well as atmosphere control are described.

In the Semi-Annual Report¹ the influence of the O/U ratio on the sintering of the oxide-metal pellets, on the coupling characteristics leading to the formation of an internal molten

zone, on the melting and solidification kinetics relative to maintaining a stable molten zone, and on the cooling process needed to obtain large, sound (crack-free) specimens was reviewed. In this prior Report it was noted that a uranium dioxide powder with an O/U ratio in the neighborhood of 2.1 was desirable for the sintering and densification of oxide-metal samples as well as maintaining an electrical conductivity suitable for initiating rf melting leading to the formation of a stable molten zone. While a high O/U ratio was desirable prior to initiating composite growth, the subsequent evolution of oxygen from the oxide phase during melting was troublesome, especially at fast growth rates because of oxidation problems with the metal component of the UO_2 -W mixture. Figure 23 shows the voids and poor growth geometry in a $UO_{2.14} + 10\%$ W sample lowered at 32 cm/hr. (Growth rates greater than 5 to 10 cm/hr are of interest because they should yield composite structures containing greater than 50 million less than 0.1 micron diameter fibers/cm², and such geometries are of interest for several applications.)

In an effort to circumvent the oxidation problem several kilograms of the UO_2 powder (with an as-received O/U ratio of 2.14) was reduced in hydrogen and subsequently partially reoxidized to give an O/U ratio in the neighborhood of 2.03 to 2.04. This oxide was incorporated with 3 to 10 weight % W for composite growth. Results of these experiments are tabulated in Table IV. The most important observation from these runs was that even compositions containing as little as 3.3 weight %



Figure 23. Longitudinal Section of $UO_2.14 - 10$ Weight % W Rod Lowered at 32 cm/hr Showing Trapped Voids and Poor Growth Geometry. X1.5.

TABLE IV
THE RESULTS OF UO₂-W COMPOSITE GROWTH*
USING UO_{2.03} AND VARYING W ADDITIONS

Experiment Number	W Addition Weight %	Growth Rate cm/hr	Description of Composite Growth
3-29	10	6.0	All samples exhibited horizontal
3-29a	7.7	3.1	layers of pure oxide (horizontal banding) and excess undissolved
13-63	5.0	-	W and limited eutectic growth.
13-64	3.3	2.4	Figures 24 and 25 are typical of this growth mode.

*Growth atmosphere in these experiments consisted of approximately 10% H₂ and 90% N₂.

tungsten, when melted with UO_2 , exhibited limited eutectic growth; and, particles of tungsten were present in the melt zone which apparently had never gone into solution. Figures 24 and 25 show the typical UO_2 -W structures in these samples. Based on these results and subsequent runs (to be described shortly), it was evident that the solubility of tungsten in molten UO_2 was dependent on the oxygen-to-metal ratio of the oxide. This result was unexpected, primarily because the unit cell size of many solidified UO_2 -W samples has been determined by x-ray analysis³, and these data indicated the oxide stoichiometry (O/U ratio) was very close to 2.00. As a consequence, it was assumed that W was soluble in molten UO_2 . In addition, oxide-metal solidification in systems such as Y_2O_3 stabilized ZrO_2 -W and HfO_2 -W has been readily achieved, and these oxides exhibit little if any measurable increase in the oxygen-to-metal ratio above the stoichiometric ratio of 2.00. Therefore in these systems sufficient W solubility was achieved for good composite growth without the possibility of increasing the metal-to-oxygen ratio of the molten oxide above 2.00. In fact, in the HfO_2 and ZrO_2 -W systems the addition of Y_2O_3 as a stabilizer may actually lead to an oxygen vacancy type liquid structure.

The recent work of Latta and Fryxell⁵ in which they melted various oxygen to uranium ratio samples in a tungsten capsule also indicated that the tungsten solubility in molten UO_2 was dependent on the O/U ratio. Their data showing this behavior is reproduced in Figure 26.

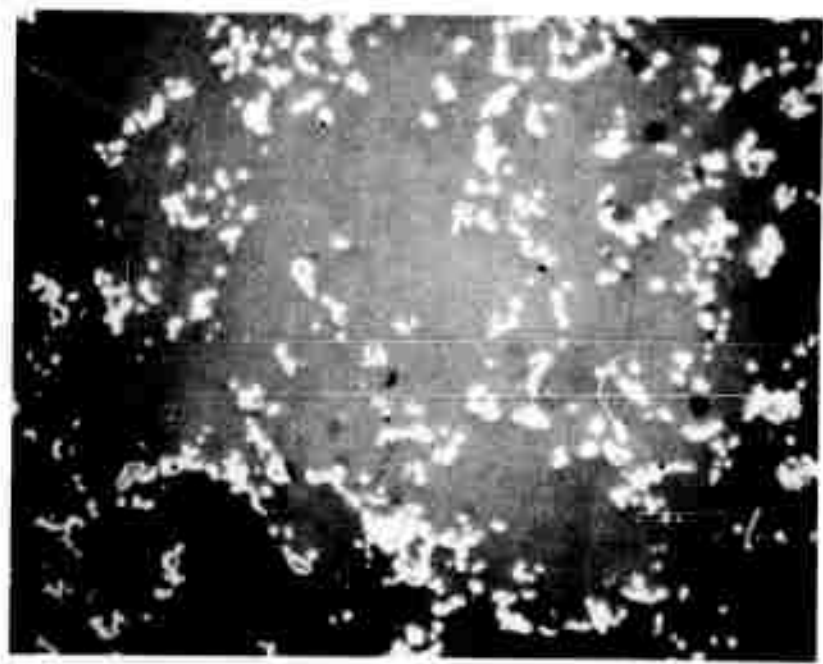


Figure 24. Longitudinal Section of $UO_2.05$ - 5 Weight % W Sample Showing Large Particles of Partially Dissolved W in Base of Molten Zone. Bright Field, X200.



Figure 25. Longitudinal Section of $UO_2.03$ - 5 Weight % W Sample Displaying Limited Banded Eutectic Growth. Dark Field, X600.

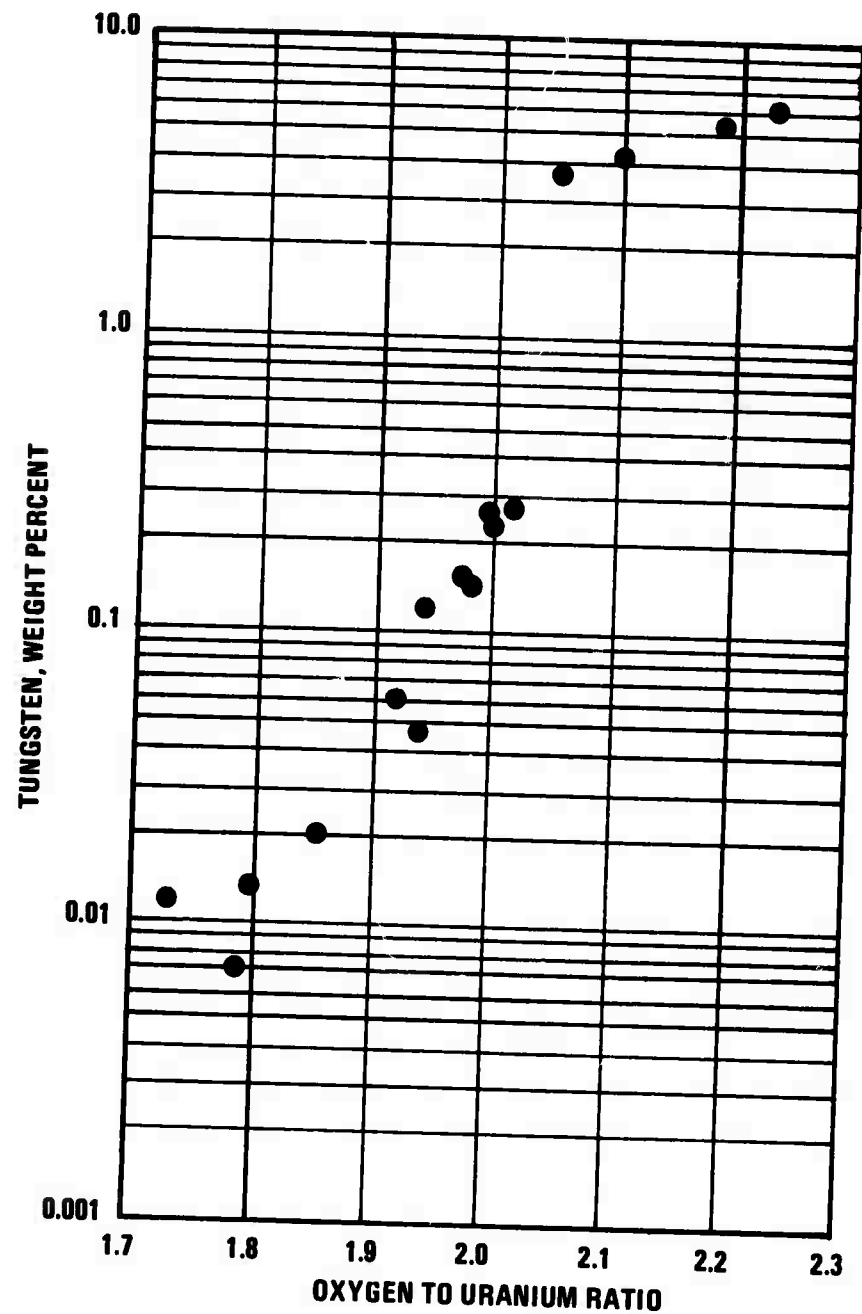


Figure 26. Tungsten Solubility in Molten UO_{2+x} as a Function of O/U Ratio from Latta and Fryxell's Work.⁵

A variety of different approaches were used to add and maintain the excess oxygen in UO_2 -W samples to achieve the W solubility required for composite growth. Table V is a partial listing of a series of experiments in which mixtures of $\text{UO}_{2.03}$ and $\text{UO}_{2.14}$ and/or partial or total replacement of the tungsten with WO_2 and WO_3 were used. In Table V the starting (premelting) O/U ratio is given for the various mixtures assuming the oxygen from the WO_2 and WO_3 additions was available to the uranium. In these runs the growth atmosphere was kept approximately constant at 10% H_2 and 90% N_2 , and growth rates between 3 and 4 cm/hr were employed. Micrographs from several experiments presented in Table V are shown in Figures 27 and 28. The general results from these runs showed that an initial premelting O/U ratio in the neighborhood of $\text{UO}_{2.08}$ or above is needed to obtain sufficient W solubility for good composite growth, if the uranium oxide is incorporated with the pure tungsten metal. Alternatively, a portion of the tungsten may be replaced with WO_2 or WO_3 , using 2 to 3% WO_3 and 7 to 8% W, and melted with $\text{UO}_{2.03}$ to achieve satisfactory composite structures. In these experiments the first extensive areas of U_xWO_3 were seen, predominantly in the top of the samples. This compound was found in the last liquid which was often rapidly cooled at the end of the zone travel. A typical structure showing UO_2 with W incorporated in the compound U_xWO_3 is shown in Figure 29.

A different and potentially more attractive approach to achieve tungsten solubility in molten UO_2 would be to maintain an oxygen potential in the growth atmosphere which would keep

TABLE V

THE RESULTS OF UO_2 -W COMPOSITE GROWTH* USING $UO_2.03$ AND $UO_2.14$
MIXTURES AND WO_2 AND WO_3 ADDITIONS WITH $UO_2.03$

Exper- iment Number	Oxide-Metal Composition	Pre- melting Weight %	Growth Rate O/U Ratio cm/hr	Description of Composite Growth
3-30	45 $UO_2.14$ 45 $UO_2.03$ 10 W	2.08	3.7	Excellent eutectic growth, continuous W fibers, no banding or excess W present.
13-69	45.5 $UO_2.14$ 45.5 $UO_2.03$ 9.0 W	2.08	2.3	Areas of good eutectic growth but thin oxide-rich horizontal bands present.
3-30a	67.5 $UO_2.03$ 22.5 $UO_2.14$ 10.0 W	2.06	3.2	Large region of undissolved W - some fair eutectic growth, oxide-rich horizontal banding in upper half of sample.
13-66	90 $UO_2.03$ 10 WO_3	2.06	2.4	Isolated areas of eutectic growth, extensive area of U_xWO_3 , no excess W present.
3-31a	90 $UO_2.03$ 9.7 W 0.3 WO_3	2.04	3.5	Oxide-rich horizontal banding, extensive areas of undissolved W.
3-33	90 $UO_2.03$ 8.8 W 1.2 WO_3	2.08	3.0	Excellent eutectic growth, no excess W present.
3-34	90 $UO_2.03$ 8.2 W 1.8 WO_3	2.10	3.0	Same as Experiment 3-33. (See Figure 28.)
3-34a	90 $UO_2.03$ 7.3 W 2.7 WO_2	2.07	3.0	Good eutectic growth but W build up heavy at sides and bottom of melt-solid interface. (See Figure 27.)

*Growth atmosphere in these experiments consisted of approximately 10% H_2 and 90% N_2 .

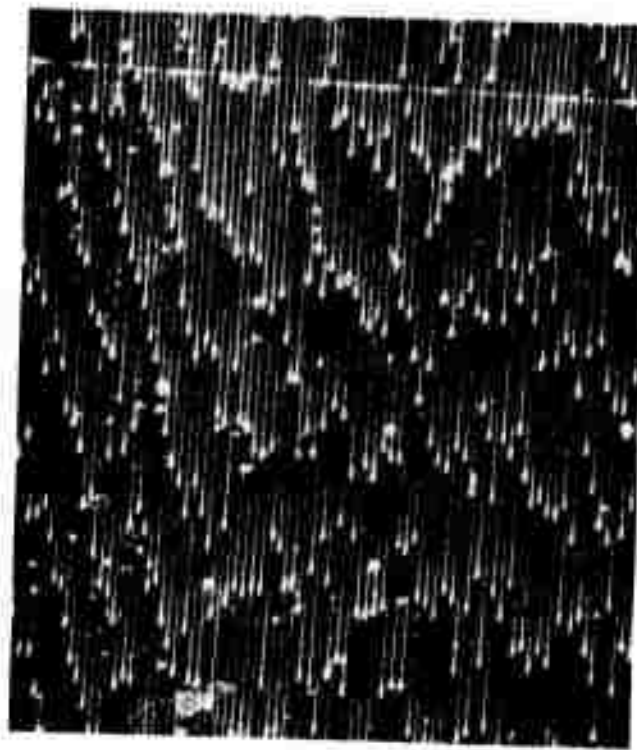


Figure 27. Longitudinal Section of UO_2 -W Composite Containing WO_2 in the Premelting Composition, Table V Experiment No. 3-34a. Dark Field, X600.

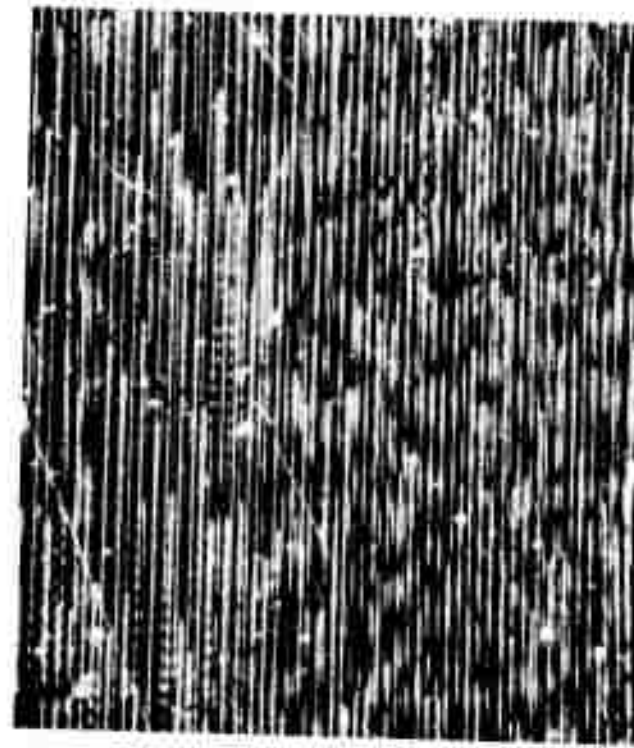


Figure 28. Longitudinal Section of UO_2 -W Composite Containing WO_3 in the Premelting Composition, Table V Experiment No. 3-34. Dark Field, X600.

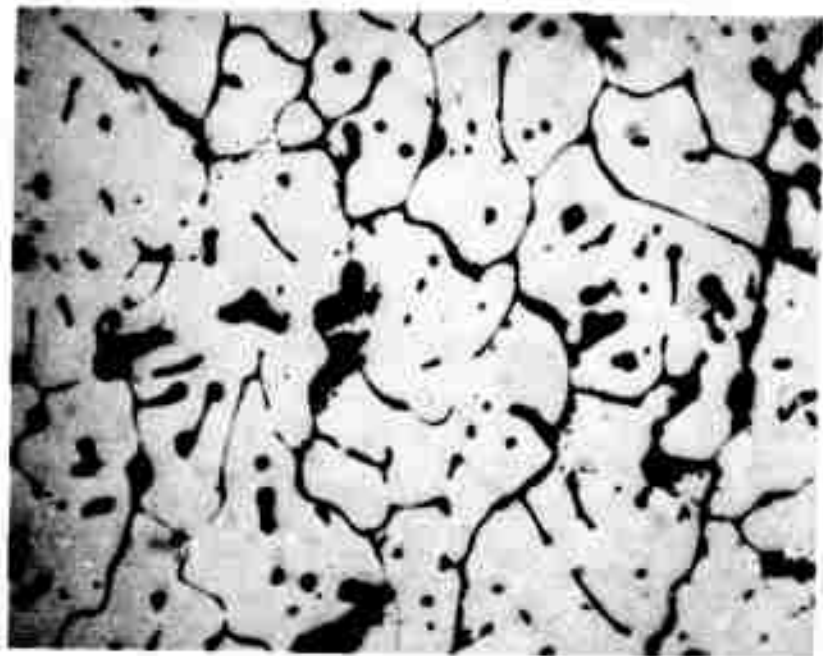


Figure 29. Typical Structure of Last Liquid to Solidify
Showing U_xWO₃ in the Boundary Between UO₂ Grains.
Bright Field, X200.

Reproduced from
best available copy.

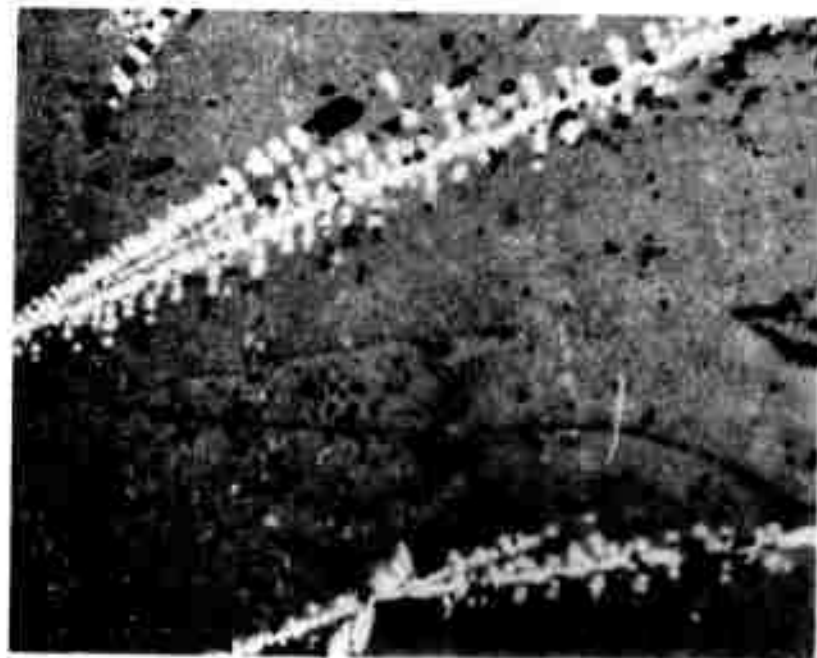


Figure 30. Tungsten Dendrites Found Extensively in a UO₂-W
Sample Melted in a N₂-Co Atmosphere, Table VI,
Experiment No. 13-70. Bright Field, X200.

the O/U ratio of the molten oxide near 2.08. Unfortunately, the large temperature gradients in the oxide-metal sample, the hot molybdenum pre- and post-heaters, and the oxygen delivery rates of various gas mixtures make this approach a formidable task. Some preliminary experiments were performed using atmosphere control to achieve the W solubility in molten UO_2 , and a partial listing of this work is presented in Table VI. Some initial observations are listed below:

- 1) Attempts to solidify UO_2 -W composites in an atmosphere of H_2 were unsuccessful (Exp. No. 8-3).
- 2) Some eutectic growth can be achieved solidifying $UO_{2.03} + W$ in a N_2 - H_2 atmosphere. Improved growth was achieved in N_2 with a small addition of H_2O . (Exps. No. 13-63 [Table IV] and 13-83).
- 3) UO_2 -W growth using H_2/H_2O ratios may be feasible, since at the temperature of the eutectic ($\sim 3000^{\circ}K$) 20,000 ppm H_2O in H_2 yields an O_2 potential which is in equilibrium with an O/U ratio of the molten oxide above 2.07.⁶ However, the cooler portions of the UO_2 -W rod will be subjected to severe reducing conditions because of less dissociation of the H_2O at lower temperatures (Exps. No. 13-73 and 13-78).
- 4) Usually the incompletely dissolved W in molten UO_2 has a "globular" shape. During growth in a N_2 and CO atmosphere, W dendrites (Figure 30) were observed (Exp. 13-70).

Thus it becomes apparent that certainly in the system UO_2 -W where the W solubility is so dependent on the O/U ratio

TABLE VI
THE RESULTS OF UO₂-W COMPOSITE GROWTH
IN VARIOUS ATMOSPHERES (OXYGEN POTENTIALS)

Experiment Number	Oxide-Metal Composition	Growth Rate cm/hr	Growth Atmosphere %	Description of Composite Growth
13-73	45 UO _{2.03} 45 UO _{2.14} 10 W	2.3	70 N ₂ 30 H ₂ +20,000 ppm H ₂ O	Bottom 2/3 excellent composite growth, top 1/3 excess W and banded growth.
8-3	90 UO _{2.14} 10 W	2.5	H ₂	Porous molten zone formation. W volatilization?
13-78	95 UO _{2.03} 5 W	2.5	H ₂ +20,000 ppm H ₂ O	Oxide-rich horizontal banding, limited W solubility.
13-83	96 UO _{2.03} 4 W	1.8	N ₂ +200ppm H ₂ O	Extensive oxide-rich horizontal banding.
13-87	47.5 UO _{2.03} 47.5 UO _{2.14} 5 W	4.7	N ₂	Extensive oxide-rich horizontal banding.
13-88	45 UO _{2.03} 45 UO _{2.14} 10 W	4.4	N ₂	Both oxide-rich horizontal banding and oxide-rich longitudinal cells.
13-70	45 UO _{2.03} 45 UO _{2.14} 10 W	5.0	80 N ₂ 20 CO	Extensive areas of oxide-rich horizontal banding, excess W and W dendrites. (See Figure 30)

of the melt, and perhaps in other oxide-metal systems, controlling oxide stoichiometry will play a major role in achieving uniform eutectic structures. Work is continuing in this area, and the current results are proving most beneficial in improving eutectic growth in other oxide-metal systems (Section 4), as well as providing insight into the parameters effecting and controlling the melt-growth of refractory oxide-metal composites.

b. UO_2 -Ta (Mo, Nb)

Preliminary experiments designed to evaluate the compatibility of metals other than tungsten as the metal component in the UO_2 -metal composites have been reported previously.^{1,2} The earlier UO_2 -Ta experiments¹ utilizing the uranium dioxide powder with an O/U ratio of 2.14 will be briefly reviewed. The availability of the reduced oxide (with an O/U ratio of 2.03 - 2.04) has greatly improved the extent of eutectic growth in UO_2 -Ta samples; and this current work will be only outlined, since much of the information is inconclusive at present. Some additional experiments designed to incorporate Mo and Nb in a UO_2 matrix will also be described.

The major problem encountered with the initial $\text{UO}_{2.14}$ -Ta samples was specimen cracking during preheating in a N_2 atmosphere and nonhomogeneous internal melting of samples in a H_2 - N_2 atmosphere. Initially it was incorrectly assumed that swelling problems were due to Ta reacting with the H_2 and/or N_2 . Several approaches were employed in an effort to minimize the apparent reaction with Ta. In an effort to reduce the large surface area

of Ta present in UO_2 -Ta pellets formed from powders, a UO_2 pellet was prepared and a hole drilled in its top face. A Ta rod was inserted into this hole to serve as the source of Ta in the melt. However, when this pellet was internally melted, the Ta rod was forced out of the hole either by gas or liquid pressure. The oxide-metal structures observed in the solidified zone around the tantalum rod suggested the formation of an ordered oxide-metal lamellar structure, Figure 31.

A pellet of $UO_2.14$ containing 13.8 weight % Ta was sintered in an atmosphere of 5% H_2 and 95% Ar at $1800-2000^\circ C$ for 1.5 hours in a controlled atmosphere furnace to densify the sample prior to internal melting and unidirectional solidification. This procedure produced a sample approaching 89% of theoretical density. The sample was subsequently preheated to $1600^\circ C$ in N_2 without cracking and internally melted in H_2 using an rf frequency of 3.8 MHz. Only a few areas of ordered Ta fiber growth were found.

The preparation of an uranium dioxide powder with an O/U ratio of 2.03-2.04 for the UO_2 -W work proved to be very beneficial to growth experiments using UO_2 -Ta mixtures, as it was possible to virtually eliminate the pellet swelling and micro-cracking problems encountered during sample sintering prior to melting. Apparently the severe sample swelling noted previously for UO_2 -Ta mixtures was the result of Ta oxidation rather than Ta nitriding or hydriding problems.

A series of $UO_2.03$ -Ta samples were solidified using various Ta/ $UO_2.03$ ratios in different atmospheres. The influence

of these parameters were inconclusive although a few general trends were noted. Figures 32 and 33 show a polished section and SEM micrographs of the best areas from the $UO_2.03$ -Ta samples. The SEM pictures, Figure 33, show a sample which was etched in the standard chromic acid etch used to expose the W fibers with UO_2 -W samples (Section III). The Ta fibers apparently are very soluble in this etchant, and holes remain in place of the Ta fibers. From the SEM micrographs a UO_2 -Ta eutectic composition of 17-18 weight % Ta was estimated. The Ta fibers were significantly larger than the metal fibers in other oxide-metal systems grown under similar conditions. Note the extensive microcracking of the oxide matrix in Figures 32 and 33.

Samples of $UO_2.03$ - 17 weight % Ta were melted in atmospheres of various ratios of H_2 and N_2 . Generally as the hydrogen content of the atmosphere was increased, the area of good Ta fiber growth decreased, and the number of small Ta droplets increased. It appears that the presence of H_2 in the growth atmosphere decreased the solubility of Ta in the molten oxide. This behavior agrees well with the effect of O/U ratio on W solubility in molten UO_2 (described in the preceding section).

Samples of $UO_2.03$ containing 18 weight % Ta were also internally melted in the following atmospheres: pure CO, 60% CO - 40% N_2 , 40% CO - 60% N_2 , 17% CO - 83% N_2 and 12.5% CO - 87% N_2 . The use of the CO atmosphere created two problems. First, it was difficult to control the melting process because of severe rf arcing, and secondly the samples were poorly

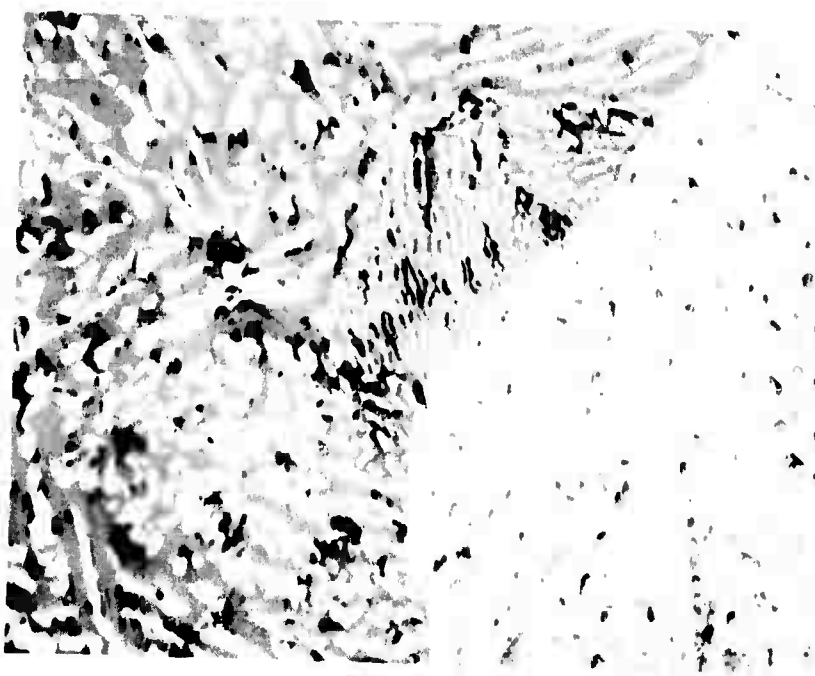


Figure 31. Solidified Region of a UO₂-Ta Sample Using a Ta Rod as the Metal Source. High Concentration of Ta Adjacent to Rod Appears Favorable for the Formation of an Oxide-Metal Lamellar Structure. Bright Field, X200.

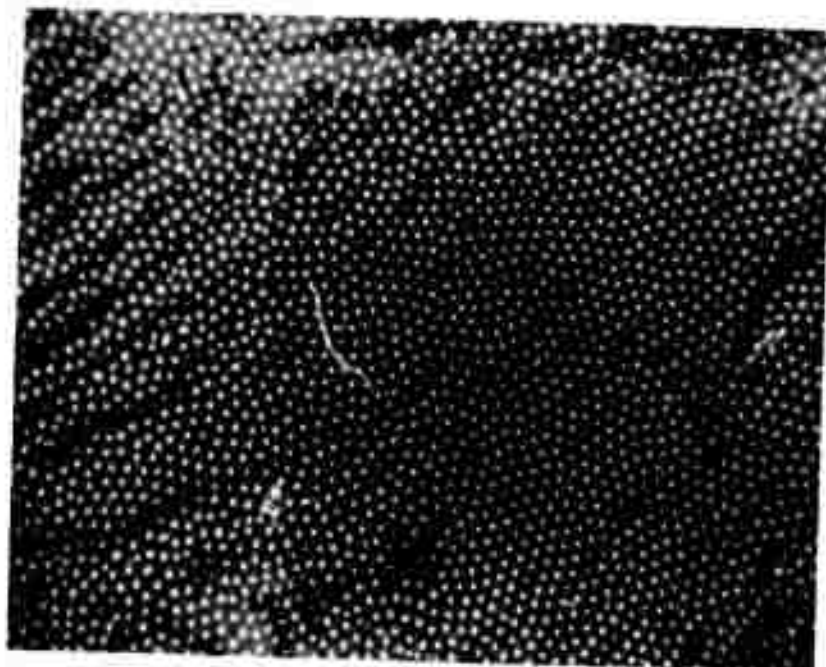
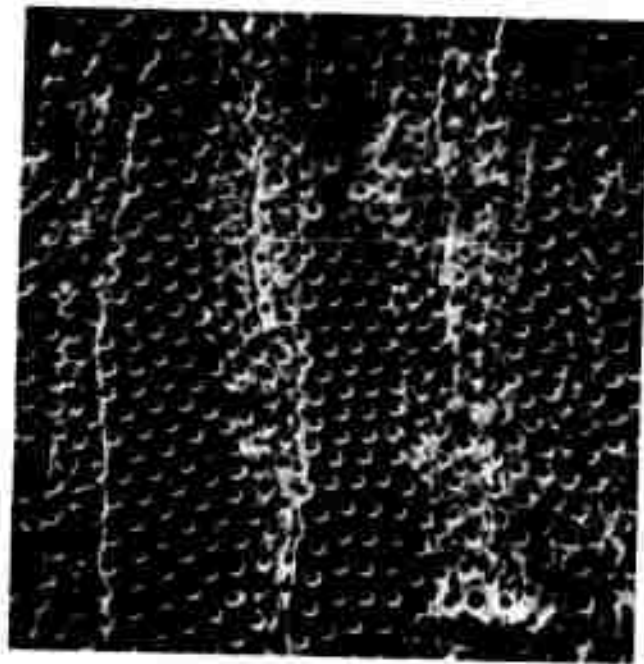
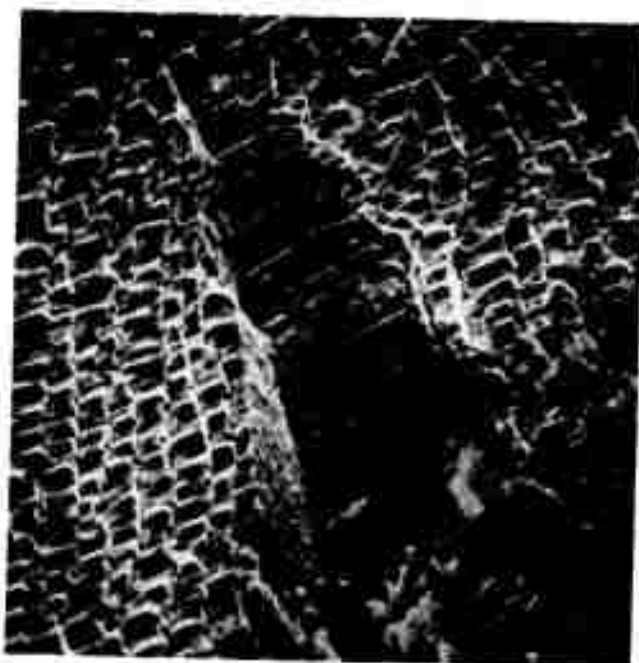


Figure 32. Transverse Section of UO₂-Ta Sample Displaying Ordered Ta Fiber Growth and Extensive Microcracking of the Matrix. Bright Field, X600.



a) Transverse Section.



b) Longitudinal Section.

Figure 33. Scanning Electron Micrographs of UO_2 -Ta Sample Etched to Remove the Ta Fibers. Note Extensive Microcracking of Matrix. X1150.

melted when their surface temperatures were maintained at about 1750°C, which in the past had produced well melted UO_2 -Ta samples. The only well melted area occurred in the sample solidified in the 17% CO atmosphere. It may be noteworthy that the microcracks normally observed in the UO_2 -Ta composites were absent in this and in an additional sample melted in a H_2 atmosphere containing 20,000 ppm H_2O . Figure 34 shows the UO_2 -Ta eutectic structure of a sample without the microcracks.

In a further attempt to better understand the influence of oxygen content of the liquid on metal solubility and unidirectionally solidified UO_2 -Ta structures, 7.5 and 2.2 weight % Ta_2O_5 was added to UO_2 -Ta pellets containing 18 and 20 weight % Ta. These additions did not appear to increase the solubility of Ta in the UO_2 when melted in N_2 . The sample containing 7.5% Ta_2O_5 swelled and cracked during melting, and no fibers were observed. The lower Ta_2O_5 addition did not cause specimen cracking until the latter stages of growth, but only a few Ta fibers were observed.

Solidification of UO_2 -Ta samples using the internal zone technique is generally more susceptible to spills of the molten interior than UO_2 -W samples, and hence minor variations in growth conditions become more critical. Undoubtedly this is partially the result of a lower eutectic temperature existing between UO_2 and Ta than UO_2 and W.

Although no concentrated effort to form ordered UO_2 -Mo and UO_2 -Nb eutectic structures has been undertaken, the success



Figure 34. Longitudinal Section of UO₂-Ta Sample Displaying Eutectic Growth and a Crack-Free Matrix. Bright Field, X600.

of using WO_3 with UO_2 - W in the UO_2 - W system suggested that the oxides of MoO_3 and Nb_2O_5 might serve similar functions with Mo and Nb - UO_2 mixtures. Several runs were made with both these oxide additions. All samples displayed extensive vaporization. In the case of MoO_3 the best eutectic structure contained strings of Mo beads rather than fibers. The UO_2 - Nb_2O_5 samples were badly cracked, and no ordered oxide-metal composite regions were found.

4. Rare Earth Oxide-Metal

The successful internal melting (Table I) of Nd_2O_3 suggested that the rare earth oxides are ideal candidates for the matrix material of oxide-metal composites, and ordered eutectic structures have been obtained using Mo and W in conjunction with Nd_2O_3 , Gd_2O_3 and La_2O_3 . After six months of experimental effort the oxide-metal composite growth using rare earth oxides has made significant progress, and these oxides appear promising as a matrix material for a variety of metals.

The properties of the rare earth oxides currently under investigation which make them attractive are as follows:

- a) they are thermally stable materials which may be melted in pure H_2 without major stoichiometry changes; b) they form very stable molten zones and allow a wide latitude of power settings between the initial internal melting and excessive melting, leading to spills of the molten zone; c) these oxides withstand the

severe thermal gradients inherent in the internal zone melting technique very well, and many sound crack-free samples have been grown; and, d) the rare earth oxide matrix can be easily selectively etched in a mild acid in order to "harvest" the metal fibers. In contrast to these desirable properties, the hydration characteristics of La_2O_3 and Nd_2O_3 make storage and analyzing these materials somewhat troublesome; the Gd_2O_3 samples show no tendency to hydrate and may be exposed to water for prolonged periods without deterioration.

In the rare earth oxide-metal growth experiments presented below, the sections will be divided based on the oxides used as the matrix material. Growth in a second series of systems containing ceria additions to the rare earth oxide-metal mixtures will then be described. In general, the ceria additions increased the metal solubility and greatly improved the eutectic growth. The system $\text{Nd}_2\text{O}_3\text{-CeO}_2\text{-Mo}$, which exhibited very well behaved eutectic growth, was used in a series of experiments designed to study the causes of discontinuous (interrupted) fiber growth, and these findings are presented in a separate subsection. The preliminary attempts to incorporate the magnetic metals Fe, Co and Ni with the rare earth oxides are described in the last subsection.

a. $\text{Nd}_2\text{O}_3\text{-W}$ and Mo

The initial rare earth oxide metal solidification work was performed using $\text{Nd}_2\text{O}_3\text{-W}$ samples containing 5 and 10 weight % W metal. These pellets were preheated to 1900°C in an $\text{H}_2\text{-N}_2$ atmosphere and melted using a 3.8 MHz rf field.

Examination of these samples showed both compositions contained tungsten fibers generally in fan shaped groupings and with very poor fiber continuity (Figure 35).

Pellets containing 2.5, 4.5 and 10 weight % Mo were also successfully internally melted using the same technique as with tungsten. Fiber structures similar to those obtained with the tungsten additions were observed. Examination of the microstructures from these experiments indicated that about 3 weight % Mo or W yielded the best fiber growth with pure Nd_2O_3 .

Two major problems were encountered melting Nd_2O_3 -W and Mo samples which are also pertinent to the other rare earth oxide-metal systems. These were the spontaneous travel of the molten zone to the top of the pellet, thus making it impossible to control the rate of travel of the solidification front and the destructive hydration of the raw powder and melted samples. The first problem was eliminated by shielding the upper portion of the pellet from the rf field with a Mo preheat tube. While this provided the necessary control over the movement of the molten zone, it did not improve the eutectic structures in the pure Nd_2O_3 -metal systems. The second problem was controlled by calcining the raw powders to 600°C prior to sample preparation and storing the raw powder and melted samples under vacuum.

b. La_2O_3 -W and Mo

Samples of La_2O_3 containing 7.5 weight % W and 5 weight % Mo respectively were internally melted and unidirectionally solidified. Both samples contained fiber structures similar

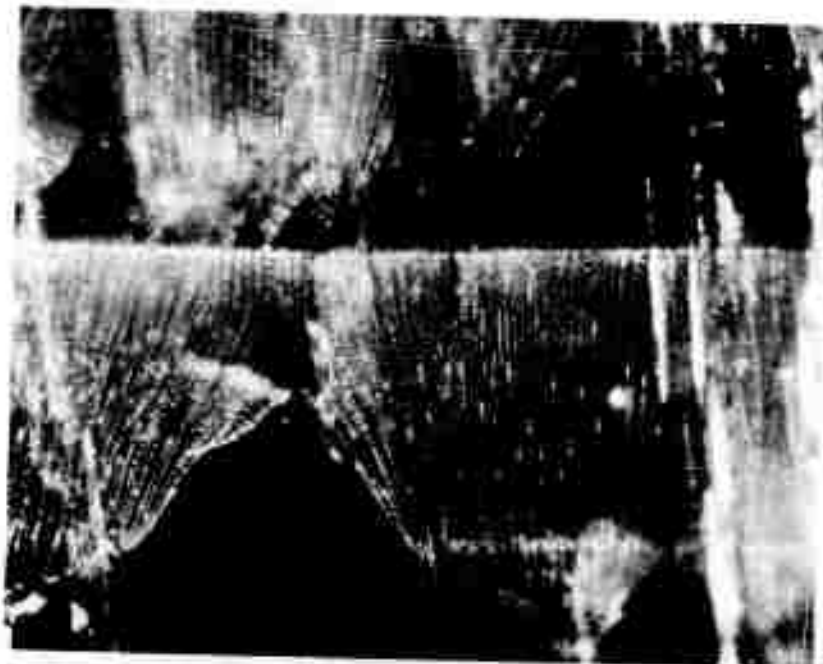


Figure 35. Longitudinal Section of Nd_2O_3 -W Sample Displaying Poor Fiber Continuity. Dark Field, X600.

to those seen in the pure Nd_2O_3 -metal systems. La_2O_3 hydrates much more rapidly than Nd_2O_3 , and both of the above samples integrated after a few weeks even though they were kept under moderate vacuum.

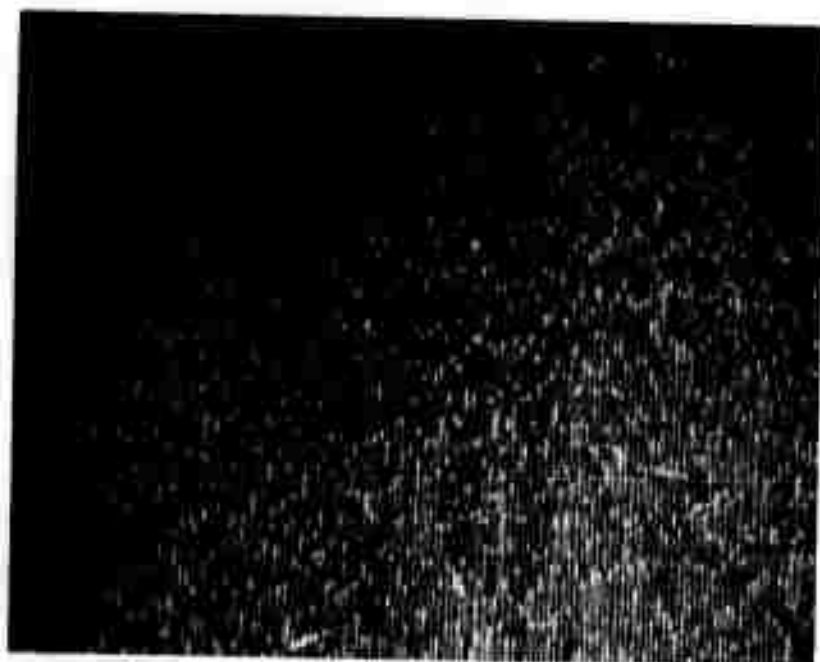
c. Dy_2O_3 -Mo

A Dy_2O_3 pellet containing 5 weight % molybdenum did not couple when preheated to 1900°C and broke up badly on cooling, suggesting the presence of a destructive phase change.

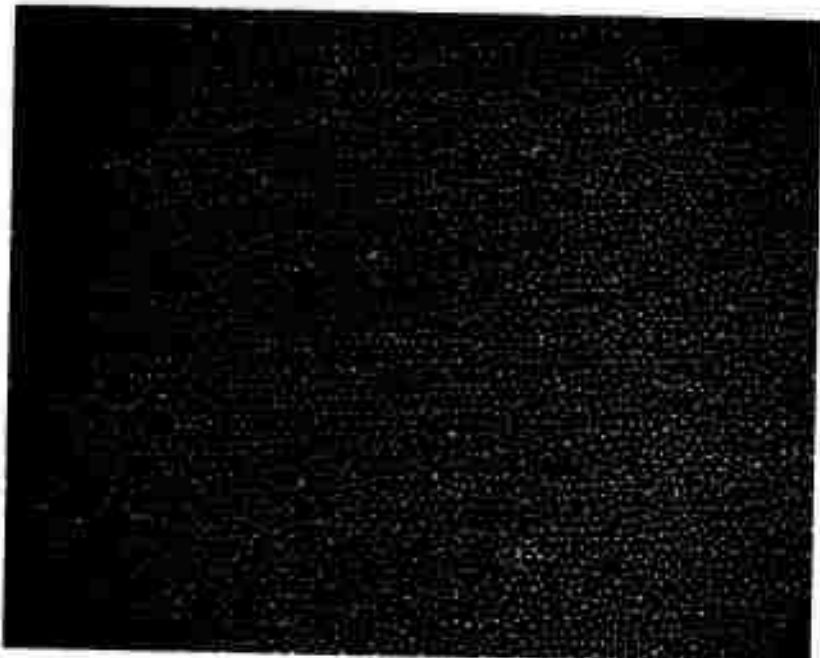
d. Nd_2O_3 - CeO_2 -W and Mo

The effect of oxygen content on composite growth observed in the UO_2 -W system suggested the addition of CeO_2 to the Nd_2O_3 -metal systems in hopes of forming a CeO_2 - Nd_2O_3 solid solution, providing extra loosely bound oxygen. Pellets of Nd_2O_3 containing CeO_2 and W or Mo were easily internally melted by preheating to 1700°C in a H_2 - N_2 atmosphere before directly coupling to a 3.8 MHz field. Solidification was controlled with the use of a top Mo preheater, and Figure 36 shows typical areas of good Mo fiber growth in the CeO_2 doped Nd_2O_3 matrix. It appears that the main effect of the ceria additions was to greatly increase the solubility of the metal in the liquid oxide, and Figure 37 compares Mo fiber structures in a typical Nd_2O_3 - CeO_2 -Mo sample with the best eutectic area seen in pure Nd_2O_3 -Mo samples.

Numerous Nd_2O_3 - CeO_2 -W or Mo samples were melted to establish the power settings, growth geometry and ratio of the constituents which gave the most uniform eutectic structures. A



a) Longitudinal Section.

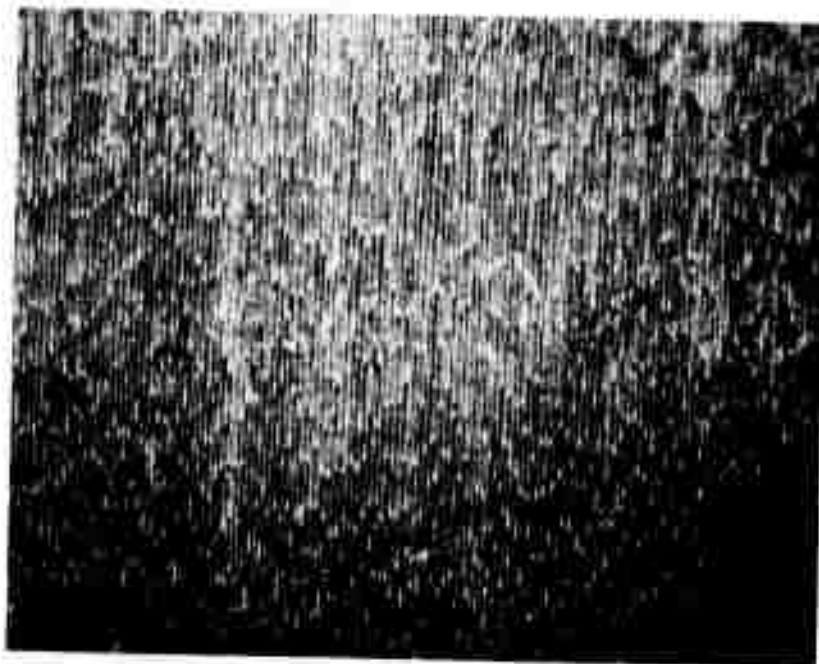


b) Transverse Section.

Figure 36. Transverse and Longitudinal Sections of "Good" Fiber Growth in the System Nd_2O_3 - CeO_2 -Mo. This Type of Growth is Typical for All the CeO_2 Doped Rare Earth Oxide-Metal Systems. Dark Field, X600.



a) Sample Without
 CeO_2 Addition.



b) Sample Con-
taining CeO_2
Addition.

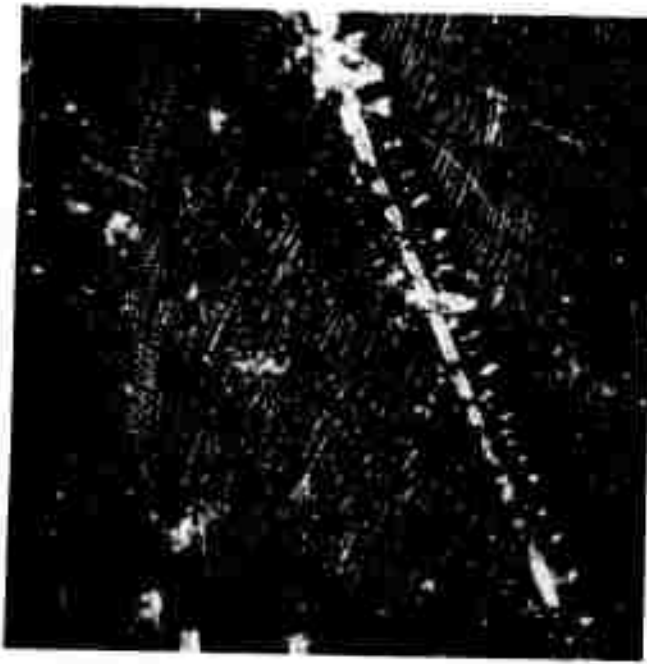
Figure 37. Longitudinal Sections Comparing the "Best" Fiber Growth Achieved in Nd_2O_3 -Mo Samples Without CeO_2 with a Typical Sample Containing CeO_2 . (Note the Dramatic Improvement in Eutectic Structure.) Dark Field, X600.

starting composition of Nd_2O_3 - 20 weight % CeO_2 containing either 15 weight % W or 10 weight % Mo gave the most consistent well ordered metal fiber geometries. Typical lowering rates of 2 to 3 cm/hr produced composites containing about 20 million fibers/cm², which were about 0.5 microns in diameter. Off-eutectic composition produced the oxide-rich "pothole" structure when there was too little metal, and metal dendrites were produced when the composition was metal rich. Figure 38 shows examples of these structures which are identical to the behavior observed in other systems.

A series of Nd_2O_3 - CeO_2 - 10 weight % Mo samples containing CeO_2 additions between 10 and 30 weight % were melted and unidirectionally solidified to establish the influence of CeO_2 content on the melting and solidification behavior of this system. X-ray diffraction analysis indicated that ceria forms a substitutional solid solution with the hexagonal Nd_2O_3 structure and between 10 and 30 weight % CeO_2 , Vegard's law, is followed very closely (Figure 39). In general the samples containing between 10 and 30 weight % CeO_2 displayed little if any noticeable change in composite geometry; however, differences in melting and solidification characteristics were noted. With increasing CeO_2 content: 1) the stability of the molten zone was increased (tendency to melt through pellet walls was greatly decreased), 2) susceptibility of samples to cracking due to thermal shock was increased, 3) preheat temperature required to obtain rf coupling decreased (electrical conductivity of sintered pellet increased), and 4) rf power requirements to maintain



a) Oxide-Rich Structure.



b) W Dendrite in Metal-Rich Structure.

Figure 38. Longitudinal Sections of $\text{Nd}_2\text{O}_3\text{-CeO}_2\text{-Mo}$ Samples Showing a) Areas of Primary Oxide ("Pothole" Structure) Seen if the System Is Oxide-Rich and b) a W Dendrite Present in Metal-Rich Structures. Dark Field, $\times 600$.

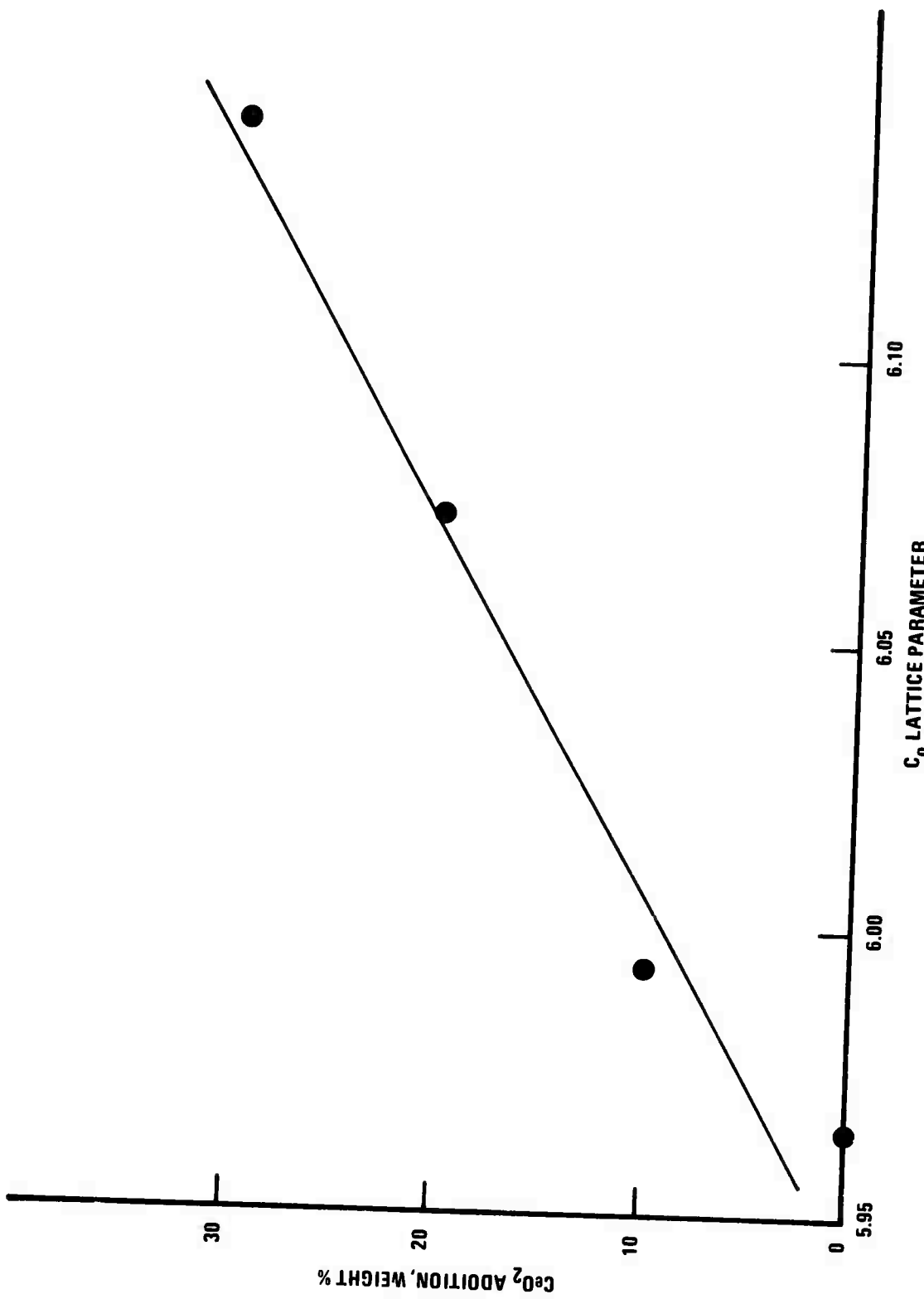


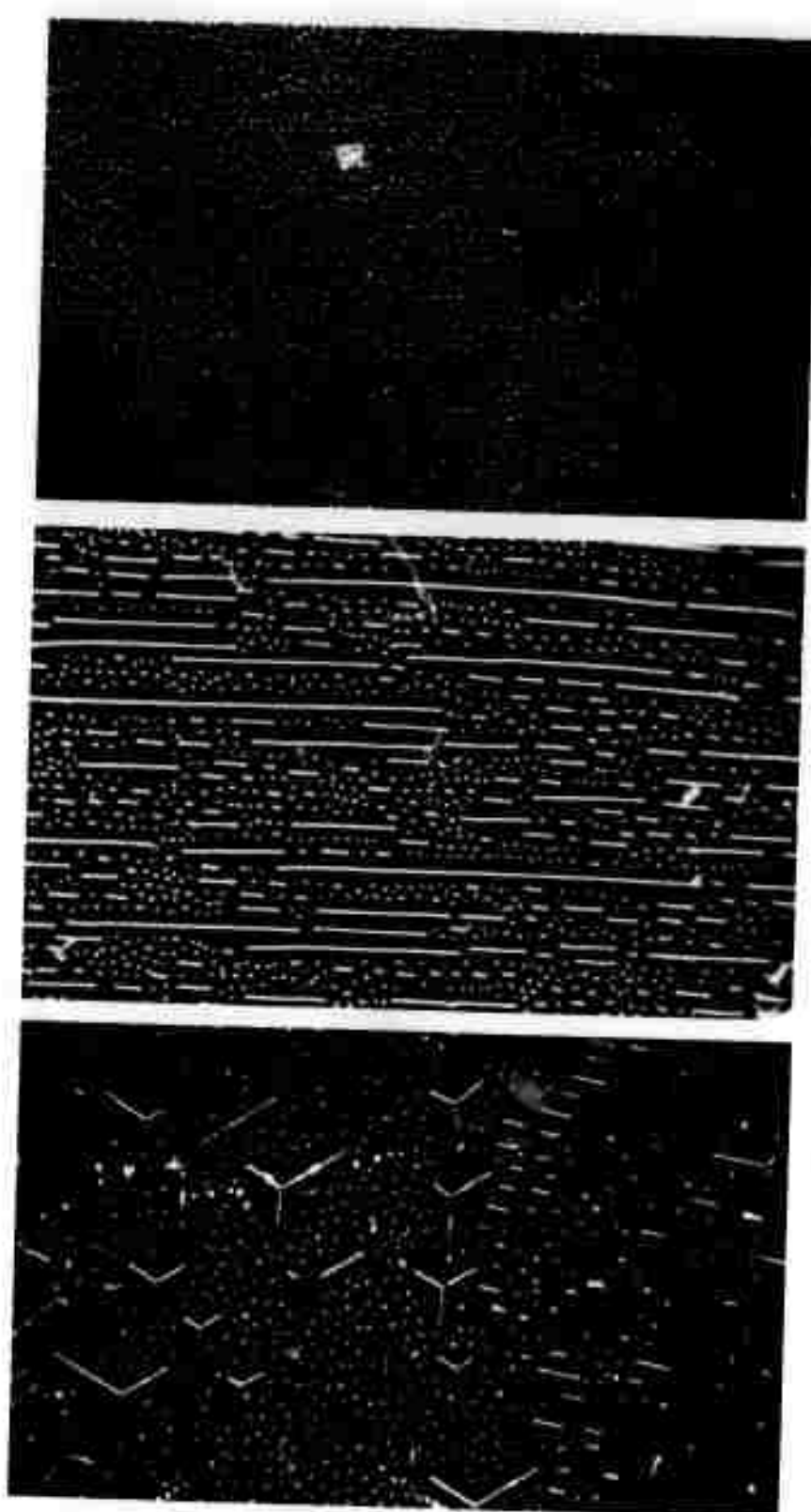
Figure 39. Increase in c_0 Lattice Parameter of Nd_2O_3 [Calculated From (0002) Planes]

a molten zone increased (electrical conductivity of liquid decreased).

Although the morphology of the metal phase seen in the $\text{Nd}_2\text{O}_3\text{-CeO}_2\text{-Mo}$ composites was about 95% circular fibers, two other morphologies (platelets and a triangular "birds feet" geometry) have also been observed and are shown in Figure 40. The platelet structure was by far the second most prevalent form. The causes of these different metal forms is unknown, but it should be noted that the structure within a given cell was predominantly one type, and that there were abrupt structural or orientational changes occurring at the colony boundaries. (Figure 41).

The technique developed to prevent the molten zone from running to the top of the pellet (top molybdenum heater tube) was combined with a bottom molybdenum post-heater tube in a growth geometry similar to Figure 1 to reduce thermal gradients and allow slower cooling of the solidified pellets. This technique consistently produced crack-free $\text{Nd}_2\text{O}_3\text{-CeO}_2\text{-W}$ or Mo samples.

One of the advantages of using the rare earth oxides is the opportunity to selectively remove the oxide matrix using weak HCl to "harvest" the metal fibers. Figure 42 is an SEM micrograph of Mo fibers after removal from the CeO_2 doped Nd_2O_3 matrix.



a) W Rod or Fiber Growth.

b) W Platelet or Lammelar Growth.

c) Random W Triangular or "Bird Feet" Growth.

Figure 40. Transverse Sections of $\text{Nd}_2\text{O}_3\text{-CeO}_2\text{-Mo}$ Samples Displaying Three Types of W Morphology. Dark Field, x600.

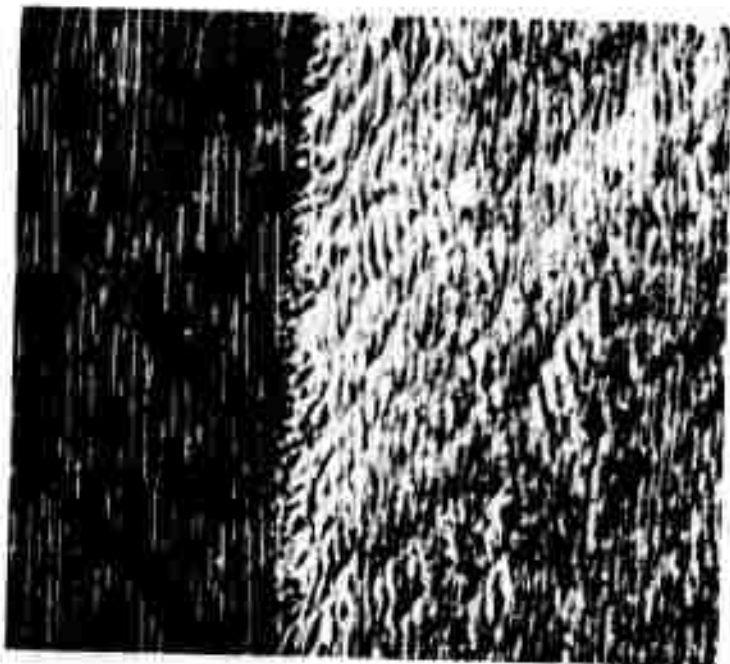


Figure 41. Longitudinal Section of $\text{Nd}_2\text{O}_3\text{-CeO}_2\text{-Mo}$ Sample Showing Abrupt Change in Fiber Morphology Seen at Colony Boundaries. Dark Field, X600.

Reproduced from
best available copy.

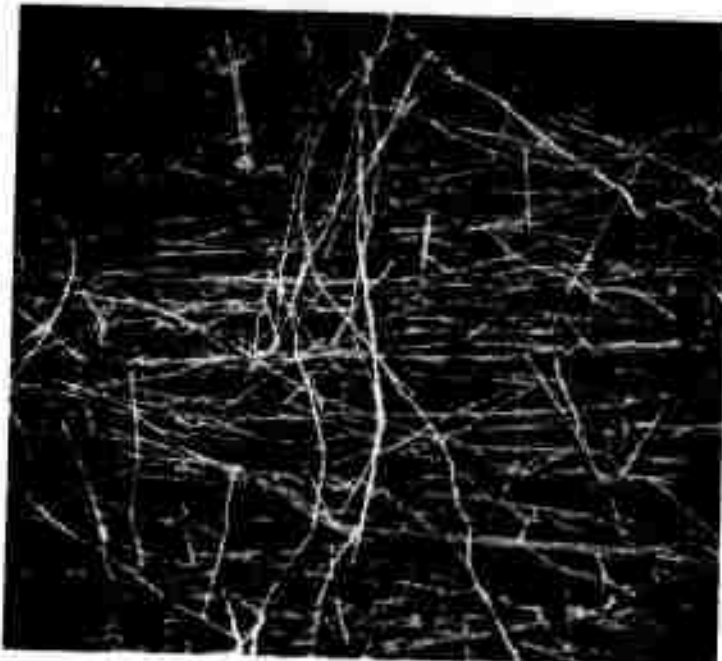


Figure 42. SEM Photograph of Mo Fibers That Have Been Removed From the $\text{Nd}_2\text{O}_3\text{-CeO}_2$ Matrix With Dilute HCl. X660.

e. Gd_2O_3 - CeO_2 -W and Mo

Gadolinia- CeO_2 -W and Mo composites have been successfully grown using the same technique described for the Nd_2O_3 - CeO_2 -Mo samples. Fiber structures as good as those previously grown in the Nd_2O_3 - CeO_2 -metal systems and identical with Figure 36 were observed for Gd_2O_3 samples containing 20 weight % CeO_2 with 10 weight % Mo or 15 weight % W. It should be noted that this is a significant achievement, since gadolinia does not destructively hydrate as do La_2O_3 and Nd_2O_3 . Gadolinia samples have been kept under water for two months with no signs of hydration.

Fiber densities in these systems ranged from 21×10^6 fibers/cm² in a sample containing 10 weight % Mo which was lowered at 3 cm/hr to 8×10^6 fibers/cm², in a sample containing 16 weight % W which was lowered at 0.8 cm/hr. The only differences noted between the Nd_2O_3 - CeO_2 -metal and Gd_2O_3 - CeO_2 -metal systems was that for Gd_2O_3 : 1) higher preheat temperatures were required for coupling, (sintered gadolinia pellets have lower electrical conductivities), 2) the samples were more susceptible to thermal shock, 3) the composite structures displayed a greater tendency to form metal platelets, and 4) a narrower range of power settings was available between melting through the pellet walls and achieving a well melted internal zone.

f. La_2O_3 - CeO_2 -Mo

Limited work has been done on using La_2O_3 because of the severe hydration problem associated with this material. However, a La_2O_3 - CeO_2 -Mo composite containing extensive metal

fibers was successfully grown from a La_2O_3 sample containing 20 weight % ceria and 10 weight % Mo. Although it was difficult to maintain a stable zone due to melting out through the pellet walls, this experiment confirmed the trend noted previously with Nd_2O_3 and Gd_2O_3 that ceria additions improve the growth of Mo or W fibers in rare earth oxides.

g. Discontinuous Banded Fiber Growth

During the controlled unidirectional solidification of numerous oxide-metal composites in different systems, the presence of a number of distinct types of metal fiber discontinuities (banded or interrupted growth) has been observed^{1,2}. Two major types found in stabilized ZrO_2 -W samples were shown in Figures 17 and 18. The development of the system Nd_2O_3 - CeO_2 -Mo where very repeatable eutectic growth was obtainable enabled the first systematic study into the causes of fiber banding. It is felt that the results described below are applicable to the solidification behavior of other oxide-metal systems.

There are many different mechanisms which are potential causes of non-uniform growth conditions, and three of the most probable include erratic mechanical motion or vibrations, changes in input power and variable compositions in the liquid. A number of carefully controlled experiments designed to investigate the effects of mechanical vibrations and power fluctuations on banded fiber growth were run using Nd_2O_3 pellets containing 20 weight % CeO_2 and 10 weight % Mo. The lowering rate for all of these experiments was about 2 cm/hr, and the skin

temperature of the samples was maintained at 1700°C in a H₂-N₂ atmosphere. Table VII summarizes the experimental variables investigated and their effect on banded fiber growth. The artificially induced power changes of about 2% noted in Table VII is of very practical significance since power fluctuations of this magnitude are often observed, the result of line voltage surges.

In analyzing the results presented in Table VII, it should be noted that to obtain a repetitive power decrease (or increase) while maintaining nearly constant growth conditions, the power must initially be increased (or decreased). The most significant finding shown in Table VII is that power fluctuations, especially sudden decreases in input power, caused severe banding, whereas mechanical vibrations appear to be a negligible contributor to fiber discontinuities. Figure 43 shows the entire length of a Nd₂O₃-Mo sample that was subjected to the periodic 2% power changes noted in Table VII, and the regularly spaced bands are very distinct. A higher magnification view of one of the bands shown in Figure 43 is presented in Figure 44. (It is also noteworthy - Figure 43 - that the solidification front is fairly flat across the molten zone and that this solidification geometry was achieved in a sample grown without rotation to shape the liquid-solid interface.)

The reason power fluctuations caused banding can be explained by the fact that the size of the molten zone was controlled by the amount of available power, and apparently the size of the molten zone changed very rapidly with small changes

TABLE VII

SUMMARY OF ATTEMPTS TO ARTIFICIALLY INDUCE INTERRUPTED
(BANDED) FIBER GROWTH IN Nd₂O₃-CeO₂-Mo SAMPLES

<u>Treatment of Sample During Growth</u>	<u>Effect on Degree of Banding</u>
Mechanical vibration of sample.	Possibly less banding than normal.
Stopping growth (sample lowering) for 10 seconds at 5 minute intervals.	Normal random bands.
Power increased 2% for 10 seconds, then returned (<u>decreased</u>) to normal, repeated at 5 minute intervals.	Regularly spaced bands at distances corresponding to 5 minutes of zone travel. Sample shown in Figures 43 and 44.
Power decreased 2% for 10 seconds, then returned (<u>increased</u>) to normal, repeated at 5 minute intervals.	Normal random bands.
Random increases and decreases of power for various durations of time.	Only power increases for longer than 1 second followed by power <u>decreases</u> appear to induce bands.



Figure 43. Entire Molten Zone of $\text{Nd}_2\text{O}_3\text{-CeO}_2\text{-Mo}$ Sample Showing Regularly Spaced Bands Induced Through Periodic Power Fluctuations. X2.0

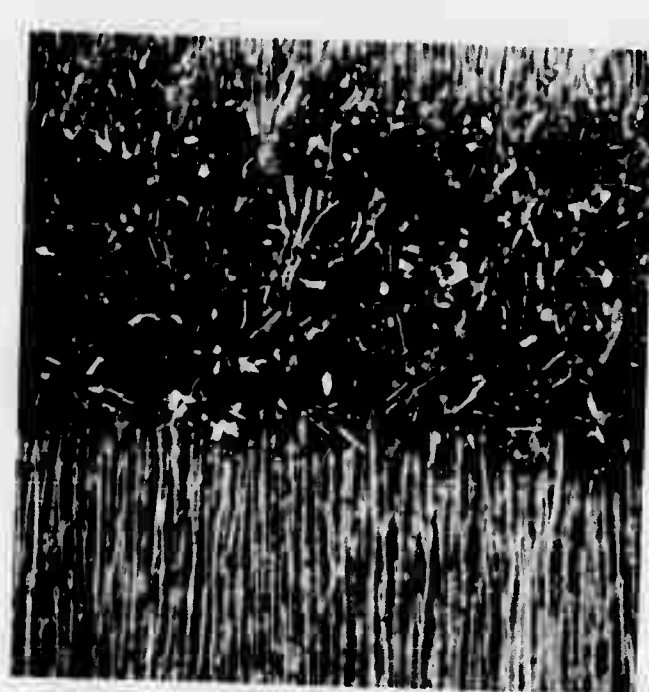


Figure 44. Higher Magnification View of the Band Induced Through a Power Fluctuation Shown in Figure 43. Dark Field, X600.

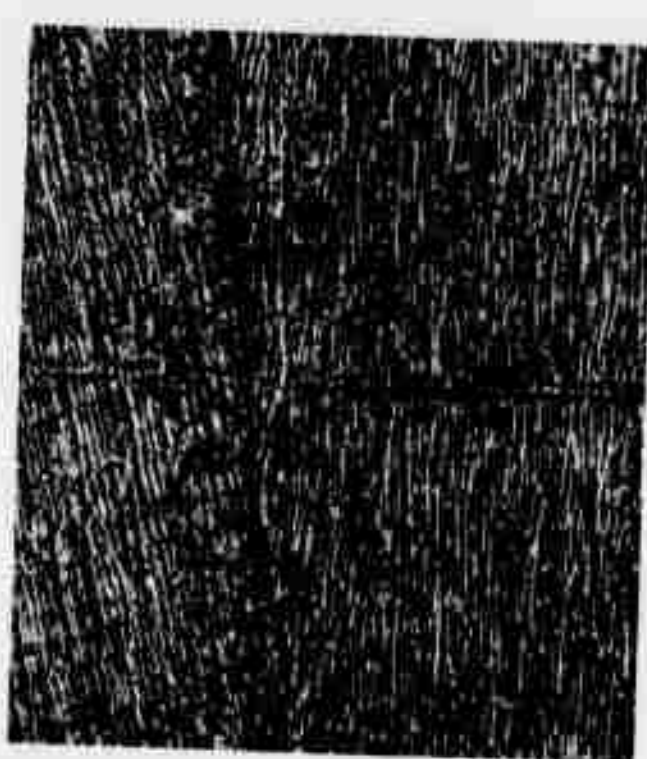


Figure 45. Longitudinal Section of $\text{Nd}_2\text{O}_3\text{-CeO}_2\text{-Mo}$ Sample Showing Narrow Band of Pure Oxide With Aligned Fibers Above and Below the Discontinuity. Also Note the Typical Cell or Colony Boundary. Dark Field, X600.

in input power. During growth when the power increased abruptly, (for example after the power had been decreased about 2% for ten seconds, Table VIII) some of the already solidified composite remelted. After equilibrium growth was re-established at the normal power settings, the oxide-metal solidification resumed without any major disruption of the composite structure. However, when the power was suddenly decreased (after the power had been increased about 2% for 10 seconds, Table VIII) a layer of oxide and metal was solidified much too rapidly to produce ordered growth, and the oxide band containing the Mo particles resulted. Then as controlled solidification started again the fibers renucleated, and ordered composite growth proceeded. Various ways to stabilize the input line voltage and reduce the occurrence of banded growth are currently being considered.

The cause or causes of the second type of banding shown in Figure 45 where the fibers stop, are interrupted by a narrow band of pure oxide, and then continue directly aligned over the lower fibers, is still unknown.

h. Nd_2O_3 - CeO_2 -Co, Ni and Fe

Several preliminary attempts to produce rare earth oxide-metal composite structures containing ferromagnetic metal fibers were made by melting Nd_2O_3 - 20 weight % CeO_2 pellets containing Co, Fe or Ni additions. Samples containing 10 weight % Co were difficult to couple to and could not be melted due to arcing. Pellets containing 5 and 10 weight % Fe were easily induction melted in a 20% H_2 - 80% N_2 atmosphere. The 5% Fe sample melted

through the pellet walls, spilling the molten material. More care was taken melting the 10% Fe sample, and a large solidified area was examined; however, only limited solubility was indicated as the Fe was present as small beads. Samples containing 5 and 10 weight % Ni were also melted in the same manner, and examination of the solidified area revealed the Ni to be in the form of small spheres. Based on these initial results the solubility of Co, Ni and Fe in the rare earth oxides does not appear sufficient to achieve ordered eutectic structures.

C. ELECTRON BEAM SOLIDIFICATION TECHNIQUES

A Materials Research Corporation electron beam zone refiner has been utilized in preliminary attempts to produce eutectic solidified composites in oxide-metal systems that can not be inductively melted (i.e. Al_2O_3 -W) or cannot be successfully self contained using the internal floating zone technique due to their low melting points.

Samples of a low melting ZnO - Nb_2O_5 eutectic composition (70 mole % ZnO - 30 mole % Nb_2O_5 , M.P. 1285°C), to which 10 and 15 weight % iron was added, were sintered to 1140°C in a nitrogen atmosphere and then machined to just fit inside a one-half inch I.D. steel crucible. The electron beam was used to weld caps onto the crucibles after they had been evacuated. Two attempts to unidirectionally solidify these compositions using the zone refiner failed when the samples melted through the crucible walls. The primary reasons for this problem were the

difficulty in obtaining accurate temperature readings on the highly reflective crucible wall and an apparent increase in crucible temperature because of a change in the thermal geometry as the hot zone moved towards the top of the crucible.

A third $ZnO-Nb_2O_5$ eutectic sample containing 15 weight % Fe was prepared and enclosed in an evacuated steel crucible. This crucible was induction heated to $1350^{\circ}C$ using a 3.8 MHz field in an effort to control the temperature more effectively, and was lowered through the rf coil to unidirectionally solidify the melt. This sample also reacted with and melted through the crucible wall. Examination of the solidified portions of these samples revealed some limited areas of iron lamellae structures in the 15 weight % iron samples, which may indicate that if more iron is added to this system and suitable containment is available, an ordered oxide-metal structure might result.

A sample of Al_2O_3 - 30 mole % CeO_2 containing 10 weight % tungsten was sintered and machined to fit inside a one-half inch I.D. tungsten crucible. During the attempt to electron beam weld the lid to this crucible, a supporting platform of the zone refiner which was fabricated out of aluminum failed. The oxide-metal mixture was then melted and unidirectionally solidified in a 20 volume % H_2-N_2 atmosphere using a 3.8 MHz rf field to heat the crucible. The surface temperature of the hottest portion of the crucible was maintained at $1900^{\circ}C$ as the crucible was lowered through the rf coil. Examination of the sample revealed that most of the tungsten had migrated to the center

of the solidified zone. It appeared that little or no tungsten was soluble in the molten oxide mixture. The presence of numerous voids and irregular shaped tungsten particles indicated that higher temperatures will be necessary in future attempts to melt Al_2O_3 -metal mixtures.

SECTION III

THE FORMATION OF OPTIMUM EMITTING ARRAYS

During the past year several advancements have been made in the area of selective etching of oxide-metal composites. In previous reports¹⁻³ procedures were reported for exposing, shaping and removing tungsten fibers in UO_2 -W and ZrO_2 -W samples. Now several new developments have been made in these areas, and in addition HfO_2 -W and rare earth oxide-Mo (Nd_2O_3 , Gd_2O_3) samples have been successfully etched to expose the W or Mo fibers.

Possibly the most interesting development during this period has been the successful etching of the ZrO_2 -W materials to expose the fibers; the same procedure has also been successful with HfO_2 -W samples. The last report¹ noted the preliminary work using hot, concentrated phosphoric acid to etch ZrO_2 -W specimens. Continued work in this area has resulted in some very satisfactory results. Samples were etched by placing a smoothly polished specimen in a beaker containing concentrated phosphoric acid, then heating to 175-210°C and holding for approximately 17 hours. At present there are large variations in the etched samples as far as fiber length and matrix texture are concerned, even when etched as nearly identically as possible. Figures 46, 47 and 48 display the range of results obtained to date. These variations are at present unexplained. One of the first samples etched under these conditions is shown in Figure 46. As can be seen the matrix is etched into a hillock-like

structure, contrasting with the smooth matrix of the sample in Figure 47. Noticeable also is the wide variation in fiber lengths from the fibers 0.5 microns high in Figure 46 to the fibers 15 microns in length in Figure 48.

On the basis of the work to date it appears that control of changes in acid composition at the high temperatures used, the control of etching temperature, and an understanding of the saturation of the etchant with the only slightly soluble zirconia-phosphate material are necessary to provide good control and repeatability in the etching process. It should also be pointed out that the samples shown in the Figures were grown under a wide variety of growth conditions, and that this too may be an important variable.

The etching procedure used with the ZrO_2 -W samples has been successfully employed to remove the matrix in HfO_2 -W specimens. Figure 49 shows the results of etching this material for 22 hours and the small diameter of the W fibers, about 0.15 microns, is noteworthy.

In the selective etching of UO_2 -W specimens to remove the oxide matrix there have been two recent developments. The first of these is the ability to produce sharply pointed fibers of virtually any length required. A method of producing short ($\sim 4\mu$) pointed fibers was previously reported¹. This method made use of an etchant of the following composition:

20 ml saturated aqueous solution of CrO_3
10 ml glacial acetic acid
7 ml concentrated nitric acid
5.8 ml concentrated hydrofluoric acid

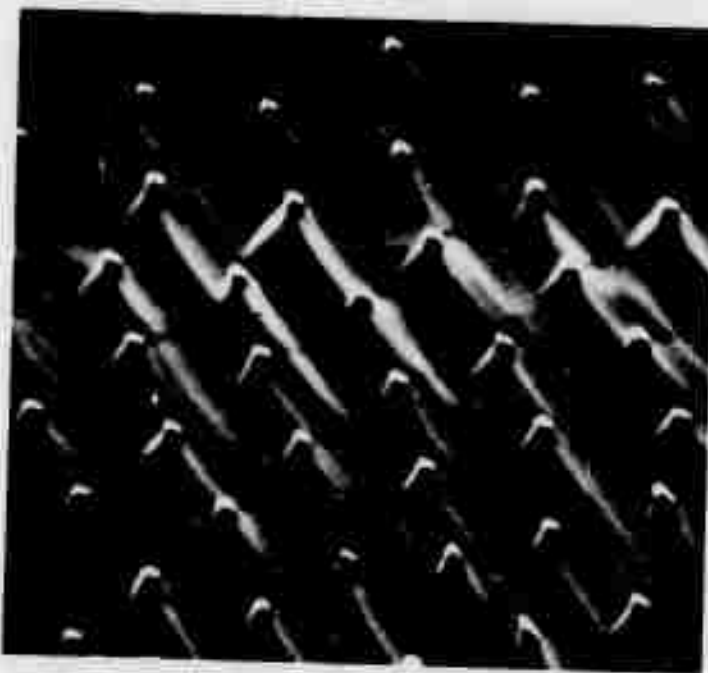


Figure 46. A $\text{ZrO}_2\text{-W}$ Sample Etched in Hot, Concentrated Phosphoric Acid for 17 Hours. Fibers Are Approximately 0.5 Microns in Length. SEM Photomicrograph, X6200.

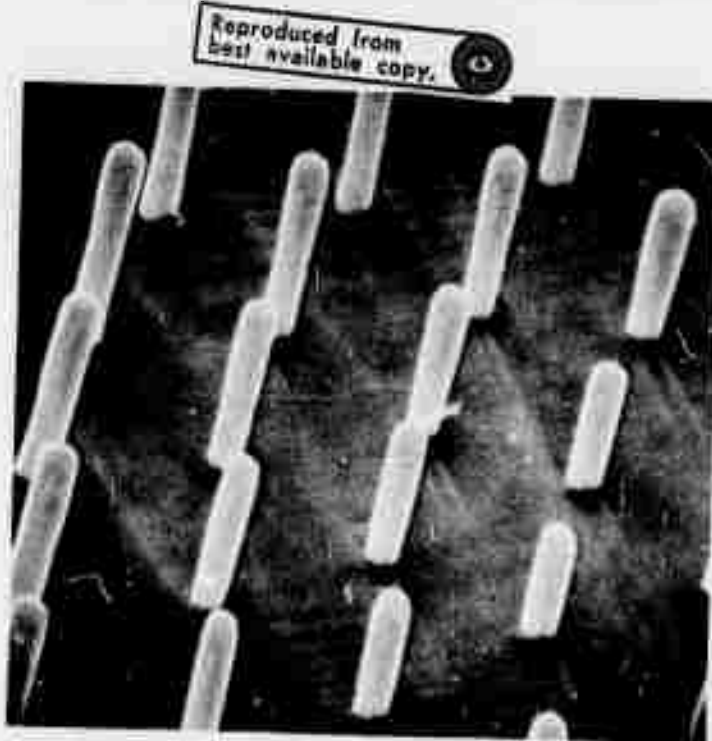


Figure 47. A $\text{ZrO}_2\text{-W}$ Sample Etched in Hot, Concentrated Phosphoric Acid for 17 Hours. Fibers Are Approximately 4 Microns in Length. SEM Photomicrograph, X6950.



Figure 48. A ZrO₂-W Sample Etched in Hot, Concentrated Phosphoric Acid for 17 Hours. Fibers Are Approximately 15 Microns in Length. SEM Photomicrograph, X6200.



Figure 49. A HfO₂-W Sample Etched in Hot, Concentrated Phosphoric Acid for 22 Hours. Fiber Diameter is Approximately 0.15 Microns. SEM Photomicrograph, X6500.

and resulted in samples as shown in Figure 50 when the sample was rotated at 20 rpm in the etchant for 40 minutes.

In addition it was previously reported¹ that the use of an etchant of the following composition:

20 ml saturated aqueous solution of CrO_3
10 ml glacial acetic acid
3 ml concentrated nitric acid
2 ml concentrated hydrofluoric acid

resulted in the exposure of tungsten fibers essentially unaffected by the etchant. This composition was used to produce fibers of virtually any length by increasing the etching time. Figure 51 shows an example of the results obtained with this composition. Notice that the fibers are blunt and cylindrical, as the etching process left them virtually unchanged in shape.

Using these two procedures in sequence it was possible to produce long, pointed fibers as seen in Figure 52. The sample was etched first to point the fibers; then using the second etchant composition the fibers were made virtually any length desired without destroying the sharply pointed tips. Exposed fibers of this morphology may be of value in enhancing electron emission characteristics.

Another interesting development in the etching of $\text{UO}_2\text{-W}$ materials was the use of an ultrasonic cleaner to provide the necessary motion of the etchant relative to the sample. Previously this was accomplished by grasping the sample in tweezers and rotating it via a geared electric motor at the desired speed. When etching very small samples which require etching over their entire surface, holding with tweezers was obviously difficult

if not impossible, and the ultrasonic vibration method has proven valuable for small samples. Another advantage of this method is the great speed with which etching can be accomplished. Figure 53 shows a sample etched for 10 minutes using the last etchant composition (3 ml HNO_3 - 2 ml HF), and the result was fibers approximately 80 microns in length. Ultrasonic etching has possibilities of providing a very good alternative method of etching; however, a number of problems with excessive matrix damage and roughness have been encountered and are not yet understood.

Preliminary work has been undertaken in etching of the rare earth oxide - Mo materials. Both Nd_2O_3 and Gd_2O_3 -Mo materials have been etched with approximately the same results. Figure 54 shows a typical etched sample of Nd_2O_3 - CeO_2 -Mo, treated for 15 seconds in a 50% HCl solution. The sample matrix shows a very definite pattern of striation and exposure of undamaged Mo fibers. A 5% HCl solution was also tried for 7 minutes with nearly identical results.

Etching of Gd_2O_3 -Mo specimens was accomplished using a 50% HCl solution for 30 minutes resulting in longer fibers but the same striated appearance of the matrix. Attack on the Gd_2O_3 samples by HCl is slower than that on Nd_2O_3 , but the end results are essentially identical.

Some work has continued in the area of selective removal of tungsten from the UO_2 and ZrO_2 matrices. Using the previously

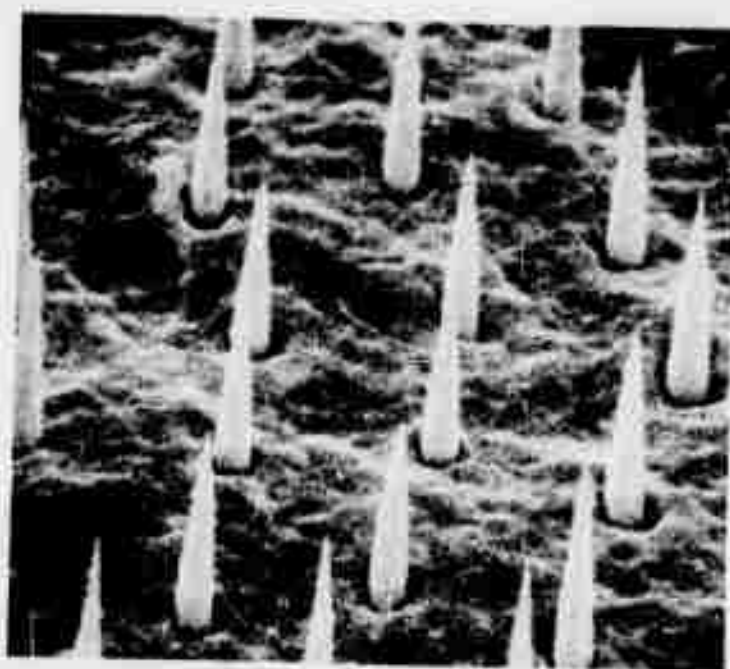


Figure 50. $\text{UO}_2\text{-W}$ Specimen Etched to Point Tungsten Fibers. Fibers Are Approximately 4 Microns in Length. SEM Photomicrograph, X9700.

Reproduced from
best available copy.

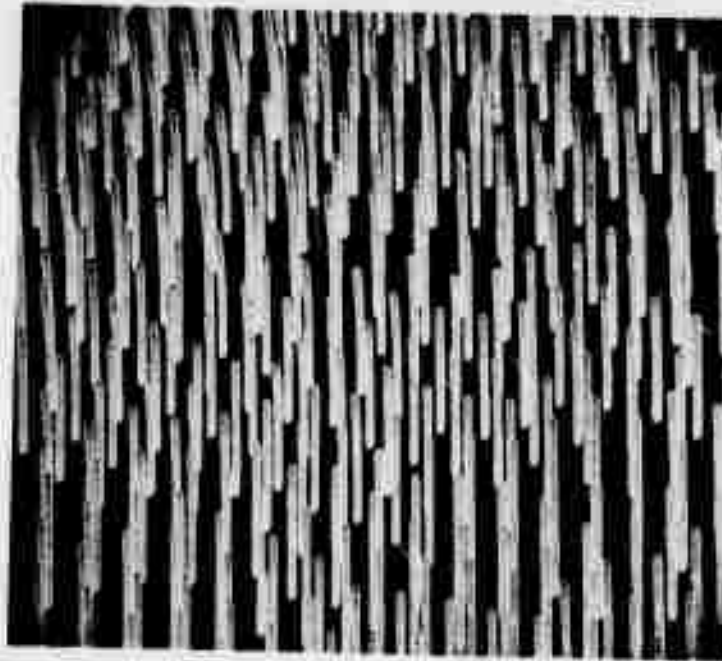


Figure 51. $\text{UO}_2\text{-W}$ Specimen Etched to Expose Fibers Without Affecting Fiber Shape. Fibers Are Approximately 17 Microns in Length. SEM Photomicrograph, X2200.

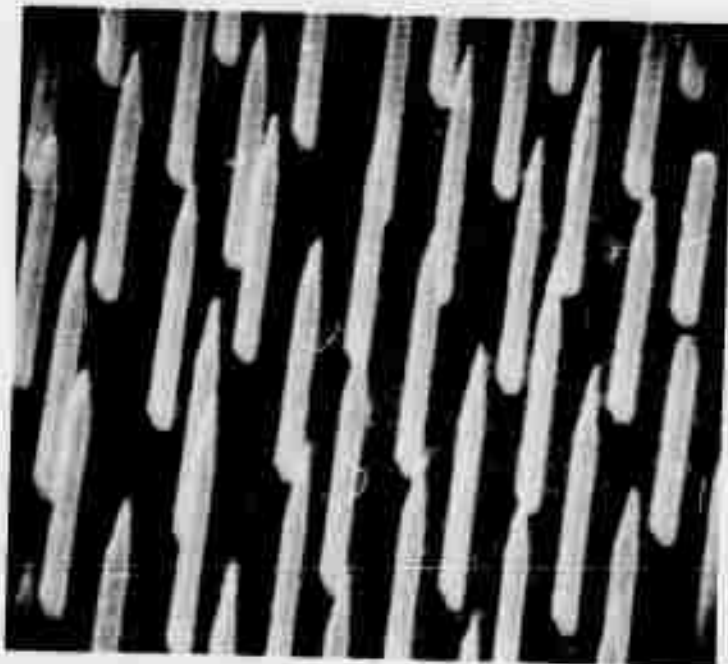


Figure 52. $\text{UO}_2\text{-W}$ Specimen Etched Using Two-Step Process to Produce Long, Sharply Pointed Fibers. Fibers Are Approximately 10 Microns in Length. SEM Photomicrograph, X6200.

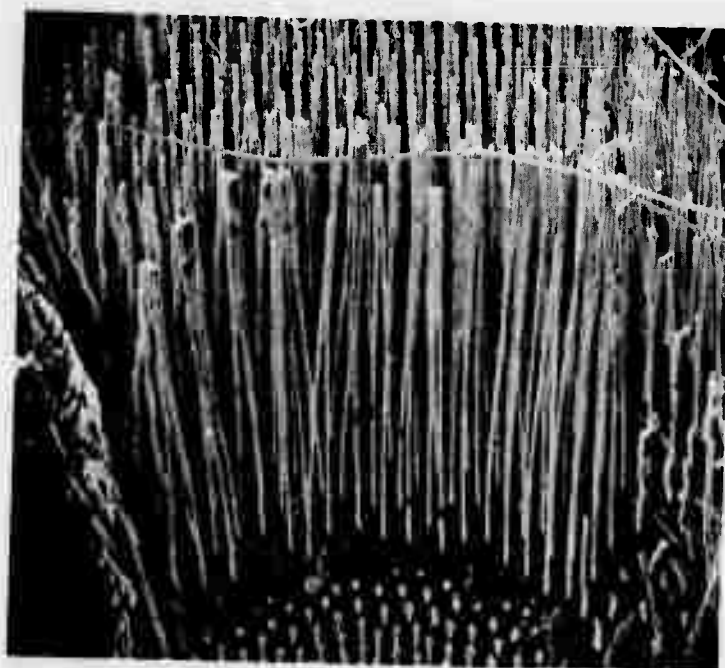


Figure 53. $\text{UO}_2\text{-W}$ Specimen Etched Using Ultrasonic Vibrator. Etching Time of 10 Minutes and Fiber Length Approximately 89 Microns. SEM Photomicrograph, X1205.



Figure 54. Nd_2O_3 -Mo Sample Etched in 50% HCl for 15 Seconds.
SEM Photomicrograph, X2500.

reported etchant composition:

100 ml distilled H₂O
5 g NaOH
15 g K₃Fe(CN)₆

it was found to be difficult to etch shallow holes, as etching times of 5 to 7 minutes gave hole depths much greater than the 18 to 30 microns previously reported. By dilution of this etchant to one-half the concentrations shown above, it was possible to gain more control of the process; however, many problems still exist in determining hole depths accurately. The ultrasonic bath has also been used with this etchant, and in preliminary work has given some indication of improved results.

SECTION IV

OXIDE-METAL COMPOSITE PROPERTIES

Electrical resistance and electrochemical deposition have been employed to characterize oxide-metal composites in an effort to understand and improve the varied and limited electron emission noted thus far. Several parameters have been suspect as limiting emission. Among them are poor electrical contact to a large portion of the metal fibers, lack of a high percentage of continuous fibers, and substantial variation in the resistance of continuous pins. Investigation of various electrical contact methods and correlation of fiber continuity with electron emission are presented. Evidence for producing electrochemical deposits on the ends of individual fibers is presented, and the prospects of using this technique to obtain a resistor (desirable for emission performance) on every pin is discussed.

A. ELECTRICAL RESISTIVITY

Until the initiation of this investigation, silver paste was used for electrical contact between SEM pins and the oxide-metal composite emission samples serving as part of the cathode in the emission test facility. Bulk resistivities of 10^3 ohm cm were measured parallel to the fibers for UO_2 -W emission samples coated on two surfaces with silver paste. The 10^3 value was

typical of the UO_2 matrix itself, which indicated a complete absence of good electrical contact to the tungsten fibers. With good electrical contact, resistivities parallel to the fibers should approach 10^{-6} ohm cm. This large discrepancy initiated a number of attempts to establish improved contact to tungsten fibers.

1. Resistivity Calculations and Resistance Measurement

Bulk resistivities based on tungsten content were calculated using resistance measurements parallel to fibers,

$$\rho = R a f_w / l$$

where ρ is bulk resistivity in ohm-cm, R is resistance of the sample in ohms, a is cross-sectional in cm^2 , f_w is volume fraction tungsten, and l is sample thickness parallel to fibers in cm. Thus, the value of ρ has as its limit the resistivity value of tungsten, or approximately 5×10^{-6} ohm-cm.

Resistance was calculated from the voltage drop across a sample and the current through the sample. Voltage was measured with a Hewlett Packard 419A DC voltmeter and amperage with a Keithley 610C electrometer. Resistance values were checked periodically by measuring the resistance of two 1% 200 ohm resistors. Values were always within the precision of the standard resistors.

Sample contact was made using both indium and mercury. Using indium contacts the composite wafers were placed between two 0.015 cm sheets of indium, and slight pressure was applied with spring loaded brass discs. In the mercury method samples

were placed between mercury filled glass capillaries. An instrument was constructed from an optical microscope frame which provided precise alignment of capillary tubing across a sample and permitted longitudinal movement of the tubing. Use of various capillary sizes allowed measurement of average resistivity values by establishing mercury contact over the entire face of a sample using large diameter tubing; or at the other extreme, a sample could be probed over small areas for regions of good pin continuity using small diameter capillary tubing.

Initial work with indium contacts on UO_2 -W resulted in resistances parallel to the fiber of the order of 10^{-2} ohm-cm. This value was obtained on sample surfaces which had been prepared by final grinding on 600 grit paper.

Next a sample of UO_2 -W was etched using the chromic acid etchant (see Section III) to expose a short length of the W fibers (~ 5 microns). Tests run with this sample as etched and rinsed in water showed no improvement in resistance compared to the unetched samples.

Discussion of this problem with Dr. Engle of the Metallurgy Section at Georgia Tech revealed the possibility of forming a WO_3 layer on the tungsten pins due to the treatment in the etchant containing chromic acid, i.e. strongly oxidizing conditions. In order to remove this oxide layer, a washing in a weak NaOH solution was tried. With NaOH the WO_3 would be expected to form a soluble sodium tungstate. Testing of this UO_2 -W sample gave a bulk tungsten resistance on the order of

10^{-4} ohm-cm. The same order of resistance was also obtained on a second sample treated identically. This represented an improvement in the conductivity of the UO_2 -W samples in the fiber direction and merited further study of NaOH treatment. (Subsequent tests are reported in Section IV, A, 2.)

A wafer of UO_2 -W was polished to a one micron diamond finish perpendicular to the fibers for comparison of the indium and mercury contact techniques. The polished sample had a 10 ohm resistance with mercury contacts. The same sample etched in the chromic acid solution to expose the fibers and cleaned with NaOH had a resistance of 30 ohms using mercury and 20 ohms when pressed between indium. The sample was repolished and remeasured using mercury contacts with a resulting 5 ohms resistance. These results indicated the mercury contact on polished samples was as low as samples that had received chemical etching and cleaning.

Because the two methods were comparable for samples that had not been vapor coated with a metal, resistance of samples without vapor coatings were measured with mercury contact. To better preserve the integrity of the coating, samples with metal vapor deposits were measured with indium contacts.

2. Effect of Chemical Cleaning and Vapor Deposited Contacts

Initial attempts to obtain good contact with the metallic pins in the oxide-metal structure using vapor deposited coatings were performed, utilizing deposition equipment located in the Engineering Experiment Station at Georgia Tech. In

trial runs UO_2 -W samples polished with flush pins and etched with exposed pins and polished ZrO_2 -W samples were coated with gold. Several wafer shaped UO_2 -W samples were polished and coated on both surfaces to provide samples for bulk resistivity measurements. Several measurements using simply a multimeter indicated that the vapor coated samples had a bulk resistivity parallel to the fiber direction of 10^{-2} ohm cm. Obviously, the vapor coating was more effective than silver paste in making electrical contact with the tungsten pins.

The other two samples that were vapor coated with gold as described above, that is, the ZrO_2 -W sample #18-16/12 and UO_2 -W sample with exposed pins #13-57/11-6, were tested for emission (Section VI). The ZrO_2 -W wafer was gold coated only on the back side for emission testing. Gold was deposited on exposed pin face of the UO_2 -W sample to a thickness of 4000 Å. A fairly uniform film was deposited on the UO_2 matrix. There were isolated areas of gold bridging on the tips of the tungsten fibers forming islands of gold above the matrix, Figure 55a. The gold had a tendency to form accumulations on the tops of the individual fibers, Figure 55b, and the islands probably formed in regions where the tip accumulations became large enough to cause significant scattering to neighboring fibers. A second cause of bridging may have been infrequent sputtering of large groups of atoms from the evaporant source. The sides of the fibers were coated with granular deposits thought to be caused by scattering from neighboring fibers.



a) X240

Reproduced from
best available copy.



b) X2400

Figure 55. Gold Vapor Deposit on Exposed Pin UO₂-W Sample.
SEM Photomicrograph.

As a result of the variation in resistivity values of UO_2 , cleaned by various techniques as described in Section IV-A-1, the effect of a more thorough cleaning on electrical contact established by gold vapor coating was studied. Three samples of $\text{ZrO}_2\text{-W}$, sequential slices (13, 14, and 15) of pellet 18-11, were selected to obtain samples with as near as possible the same fiber concentration and continuity. All samples were polished to a one micron diamond finish and ultrasonically cleaned in a detergent solution, distilled water and ethanol. After initial cleaning the samples received the chemical treatment indicated in Table VIII for Run No. 1, followed by an ultrasonic rinse in distilled water and ethanol. Gold was vapor deposited on both sides of the sample to a thickness of 3000 Å.

Resistivity values using indium contact to the gold deposits, Table VIII, indicated that best cleaning was achieved with a hydrofluoric acid etch. The value of 1.4×10^{-3} ohm-cm was the lowest resistivity measured to that date for $\text{ZrO}_2\text{-W}$ specimens. Contrary to $\text{UO}_2\text{-W}$ resistivity data, NaOH cleaning did not lower the resistivity of the $\text{ZrO}_2\text{-W}$ samples. However, the $\text{ZrO}_2\text{-W}$ results compared different samples and may have reflected variation in tungsten fiber continuity, or the hydrofluoric acid may not have formed a tungsten oxide film as proposed for the etch containing nitric acid used on $\text{UO}_2\text{-W}$ samples.

To determine if the resistivity values represented variation due to contact differences caused by cleaning or to varying fiber continuity, the three samples were repolished to a

TABLE VIII
CHEMICAL TREATMENT AND ELECTRICAL RESISTIVITY
FOR ZrO_2 -W, SAMPLE NO. 18-11

<u>Slice Number</u>	<u>Run Number</u>	<u>Cleaning Technique (a)</u>	<u>Resistivity (ohm-cm)</u>
13	1	1 ^(b)	1.4×10^{-3}
13	2	1 ^(b)	1.1×10^{-3}
14	1	2 ^(b)	2.5×10^{-1}
14	2	1 ^(b)	1.3×10^{-2}
15	1	3 ^(b)	20
15	2	1 ^(b)	1.9

(a) - All chemical treatments were followed by a distilled H_2O and Ethanol rinse.

(b) - Cleaning Techniques

- 1) - Rotated in Concentrated HF (20 rpm, 20 min.)
- 2) - Rotated in Concentrated HF (20 rpm, 20 min.)
Rinsed in Distilled H_2O , and
Rotated in Dilute NaOH (20 rpm, 20 min.)
- 3) - None^(a)

one micron diamond finish and cleaned in HF using the same procedure described for slice 13. Gold was vapor deposited on one side to a thickness of 2000 Å and 600 Å on the other. Resistivity was measured using indium as the electrical contact to the deposited gold.

Comparison of resistivity values, Table VII, for slices 14 and 15 show that the HF etch produced resistivities on order of magnitude lower than either cleaning with HF followed by a NaOH rinse or rinsing in water and ethanol. Slice 13, run as a control, exhibited almost the same resistivity after the two cleanings with HF. Of the three cleaning techniques, HF etching produced the best electrical contact between the tungsten fibers and a vapor deposited gold film.

The most significant observation from the resistivity values of adjacent slices from the same pellet was the variation in resistivity, about three orders of magnitude. The most logical explanation was variation in pin continuity. Further discussion of this point will follow in the next section.

Electrical resistivity was used in selecting ZrO_2 -W sample #18-11, slice 13, for electron emission testing as reported in Section VI. The wafer-shaped sample which was vapor coated with gold on both surfaces had a resistivity of 1.1×10^{-3} ohm-cm (corresponding to a total resistance of 0.07 ohms). After mounting on an SEM pin using silver paste the SEM pin, silver paste and emission sample composite had a resistance of 0.16 ohms. The electrical contact to the gold plated composite

surface was made with indium metal. This increase in total resistance may have reflected the poor contact the silver paste makes with the gold-plated composite structure or a deterioration of the gold film.

B. ELECTRO CHEMICAL EFFECTS

1. Composite Anodes

An investigation was initiated to develop a technique capable of delineating between continuous and discontinuous fibers in any of the oxide-metal composites. This effort was the result of the great variability observed in electrical resistivity values and the lack of any resistivities that approach the low resistance of tungsten closer than two orders of magnitude. Until this time there has been no way to determine if high resistivities result from poor electrical contact or from poor fiber continuity. The basis for the investigation was to produce an observable chemical reaction at each fiber resulting from the passage of electric current. Such a reaction would occur only at the ends of continuous fibers.

Initial experiments produced significant results, although a complete understanding of the reactions occurring is lacking at this time. An electrolysis cell was assembled, Figure 56, with an oxide-metal composite serving as the anode, aqueous copper sulfate as the solution and copper as the anode. Both UO_2 -W and ZrO_2 -W composites were used as the anode. The anodes were polished to a one micron diamond finish on both sides of the

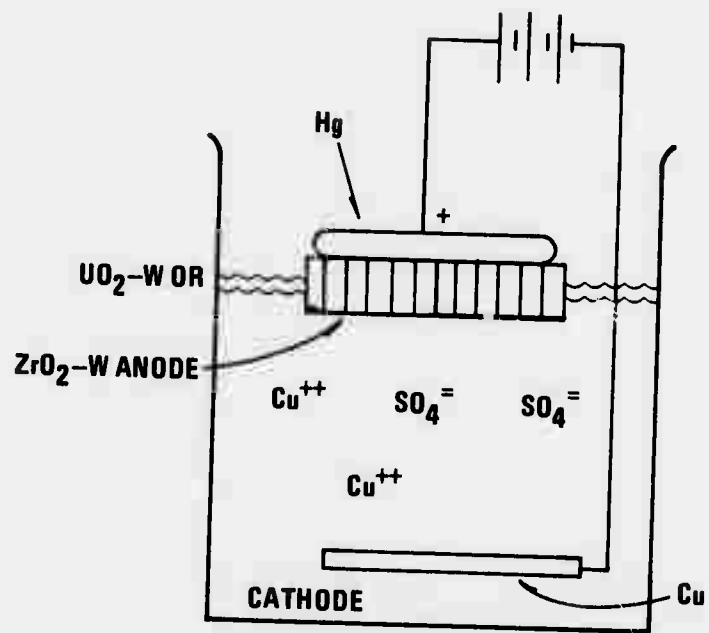


Figure 56. Copper Sulfate Electrolysis Cell Using Either $\text{UO}_2\text{-W}$ or $\text{ZrO}_2\text{-W}$ Composites as the Anode.

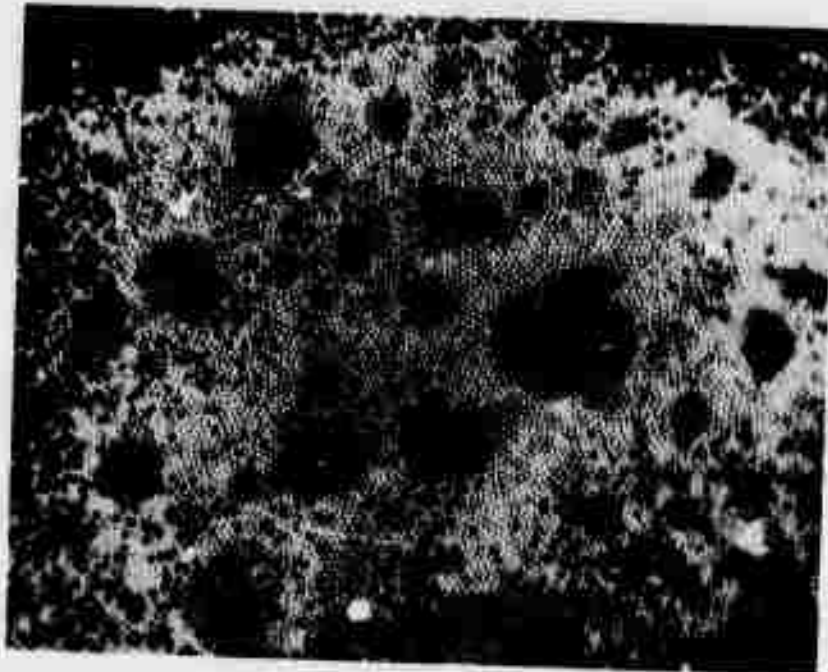
composite slice normal to the fibers. Mercury served as a contact to one side, and the other side was immersed in the copper sulfate solution. A current of 0.5×10^{-4} amps was passed for three and four minutes. The effect observed was the same for both times and both composites, $\text{UO}_2\text{-W}$ and $\text{ZrO}_2\text{-W}$. Under reflected light the reflectivity of some pins was greatly enhanced, and others were unchanged (Figures 57 and 58). (Samples immersed in the solution but not subjected to a voltage drop remained unchanged.) The enhanced reflectivity was assumed to be due to a reaction at each continuous fiber. If this hypothesis is true, continuous pins were but a small percentage of the total number of pins and were confined to the center of grains. No continuous pins were observed at or near grain boundaries in the samples examined. As can be seen from the SEM micrograph, Figure 58b, the pins had small caps on the end presumed to be tungsten oxide.

An experiment was conducted to characterize the highly reflecting caps produced on tungsten pins when $\text{ZrO}_2\text{-W}$ or $\text{UO}_2\text{-W}$ composites when used as an anode in a copper sulfate electrolysis cell. Interest in this phenomenon derived from the possibility of producing an oxide coating on the continuous pins to create a resistor in series with the individual metallic pins, and hopefully improve the emission performance. To achieve a large tungsten surface area for analysis, tungsten powder was pressed at 3300 psi in a 3/8-inch circular die and sintered in a H_2 atmosphere at 1600°C for 2 hours. The 80% dense tungsten pellets were mounted on SEM pins via silver paste and encapsulated



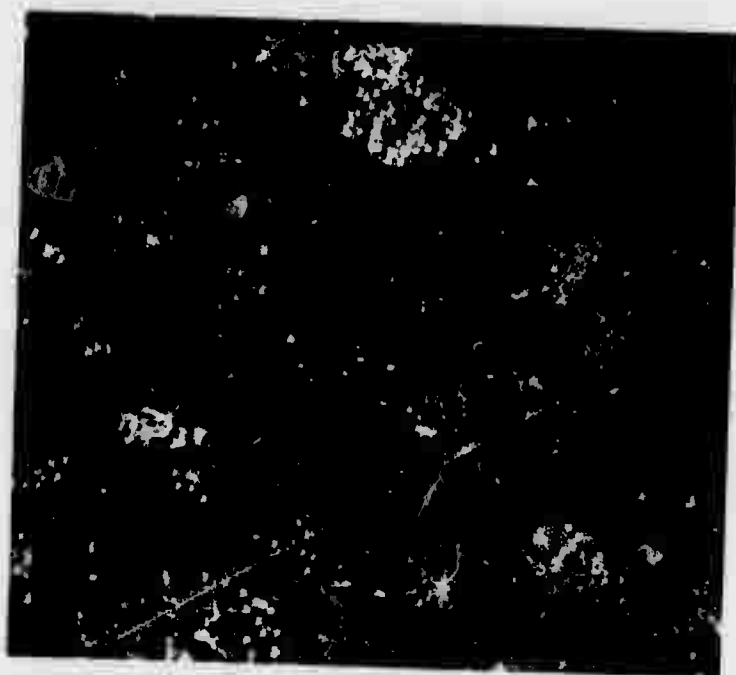
a) X200

Reproduced from
best available copy.



b) X600

Figure 57. Dark Field Reflected Light Micrographs of ZrO_2-W Sample 18-11, Slice 10, Used as Anode in a $CuSO_4$ Electrolysis Cell.



a) Dark Field,
X200.



b) SEM Photomicro-
graph, X2350.

Figure 58. UO_2 -W Sample 13-52 Used as Anode in a CuSO_4 Elec-
trolysis Cell.

in Araldite 502 epoxy (Figure 59). Electrical contact was established through the exposed stem of the SEM pin, and the exposed surface of the tungsten pellet was ground to a 600 grit finish.

The ground surface of the tungsten pellet was the anode in a N/50 H_2SO_4 electrolysis cell with platinum serving as the cathode. A 50 volt potential was maintained for 16 hours. The current, Figure 60, initially increased from 0.47 to 0.49×10^{-2} amp during the first one-half hour and then decreased to a minimum of 0.03×10^{-2} amps at 16 hours. During the first hour, the surface of the pellet turned from metallic silver to a dark blue to yellow and finally to a dull brown. Attempts were made to detect (through x-ray diffraction) any crystalline nature to the electro-chemically formed film, but there was no change in the diffraction pattern before and after electrolysis.

Mercury contact over 0.18 cm^2 of the tungsten surface was used in measuring resistance of the tungsten pellets subjected to electrolysis. Resistance prior to electrolysis was 0.13 ohms and independent of voltage. After electrolysis, resistance was voltage dependent and was 2.94×10^6 , 2.5×10^5 , and 2.78×10^4 ohms at 0.22, 0.50 and 0.86 volts respectively. The voltage dependence exhibited by the resistance of the film is typical of an oxide-metal interface.

The film was presumed to be tungsten oxide with an increasing O/W ratio from the interior to the exterior of the film. Whatever its chemical nature, the high resistance of the

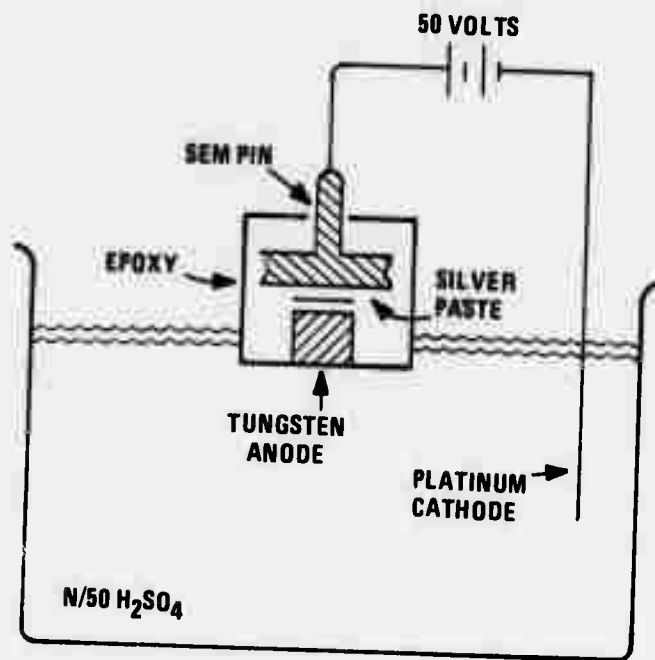


Figure 59. Sulfuric Acid Electrolysis Cell.

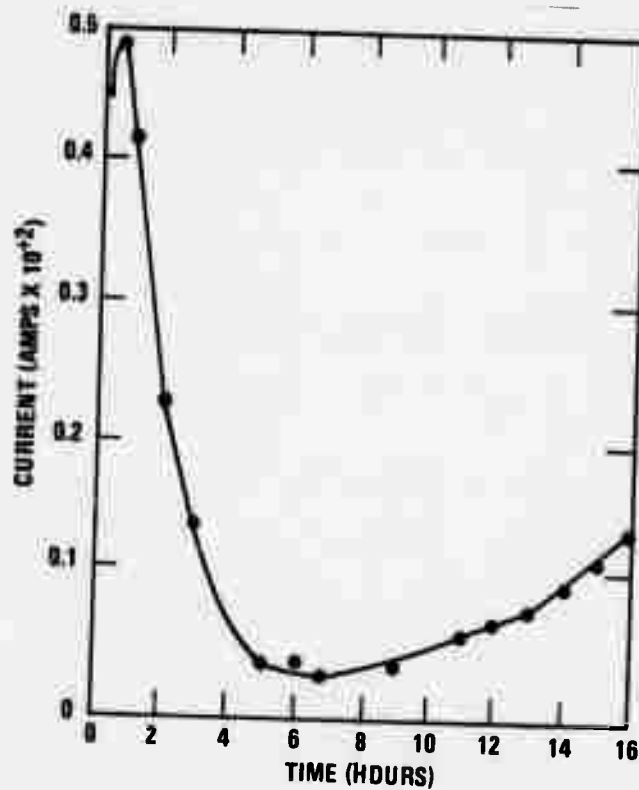


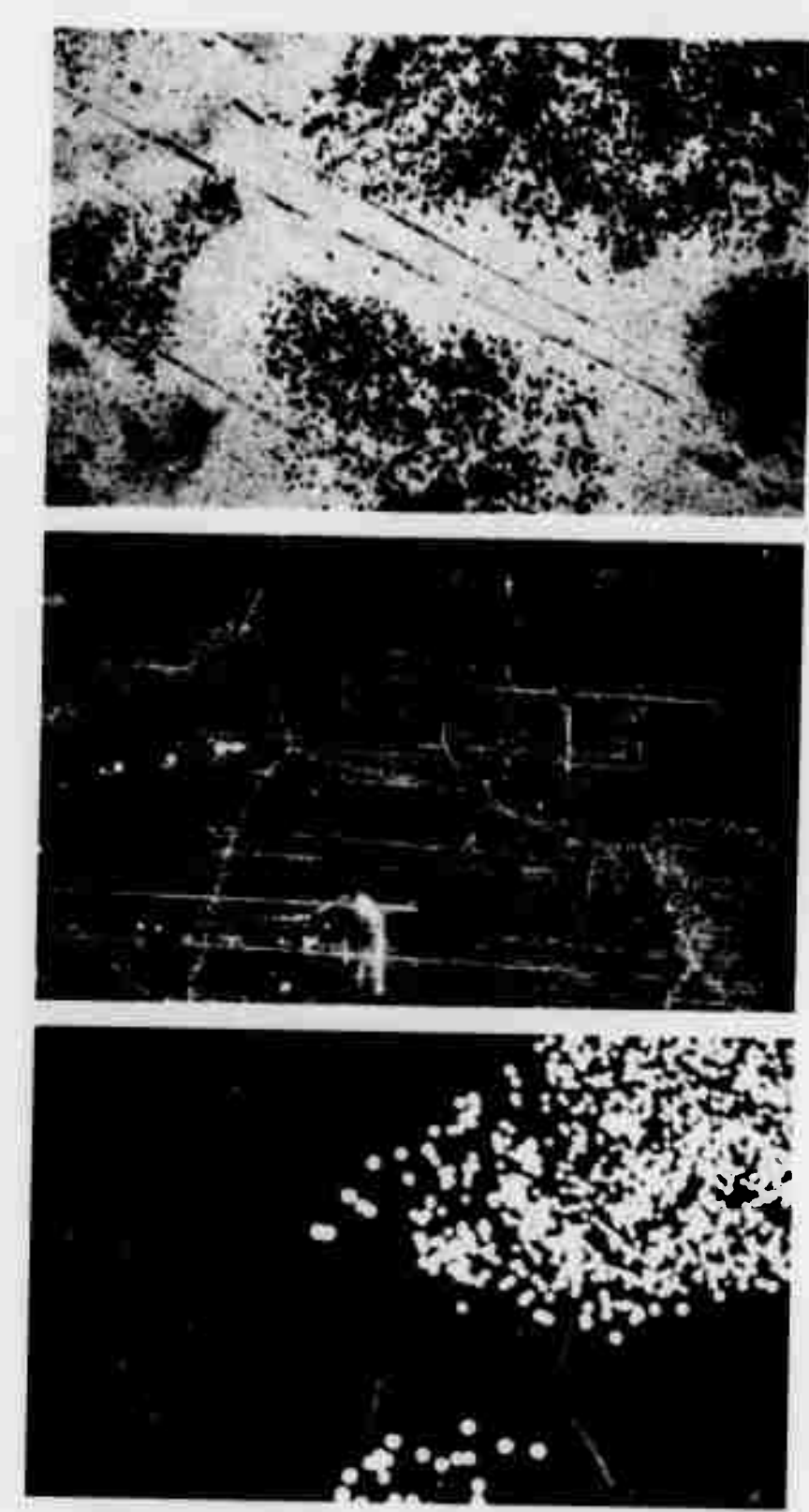
Figure 60. Electrolysis Current as a Function of Time for H_2SO_4 Cell.

film may be useful in establishing series resistors on each conducting pin in tungsten composites with insulating matrices.

2. Composite Cathodes

In an effort to correlate emission performance with fiber continuity, copper was deposited on the ZrO_2 -W sample #18-11, slice 13, after emission testing. Photomicrographs of the sample after emission showed the typical isolated areas of pin "burn out" and matrix damage (Figure 6la), presumably caused by vacuum arcs occurring during emission. For this comparison the sample was first polished, photographed (Figure 6lb), and used as the cathode in a copper sulfate electrolysis cell.

Copper was deposited from a 0.2N $CuSO_4$ solution at 2.5×10^{-5} amp for 0.5 and 2.5 minutes using a platinum anode. Copper deposits formed on individual pins in the same areas where emission damage was evident (Figure 6lc). The deposits were time dependent in that, as deposition time progressed, additional new areas of deposition appeared. Areas of low electrical resistivity would produce visible deposits first, and at longer deposition times the higher resistance areas would also build up visible deposits. This correlates with the hypothesis that during emission, the fibers in areas of low resistance emit first, burn out due to vacuum arcs if run at high emission currents, and emission moves to the area of next lowest resistance.



a) Bright Field,
X200.

b) Dark Field,
X200.

c) Dark Field,
X200.

Figure 61. Three Photomicrographs Comparing (a) Post Emission Damage, (b) Cell Boundary Location, and (c) Copper Electro-deposits for Sample ZrO₂-W Sample 18-11, Slice 13.

Again, as seen in previous work, the continuous fibers were limited to the center of grains or cells. This can be easily seen by comparing the location of the cell boundaries (Figure 61b) to the locations of the "burned out" areas of Figure 61a and the copper deposits in Figure 61c. Again there was no evidence of any continuous fibers for approximately 40 to 50 microns away from each grain boundary.

In future tests using the oxide-metal composites alternately as the anode and cathode in an electrolysis cell, it may be possible to show "all possible" emission sites when the sample is employed as the anode, and the "primary" emission sites when the sample is the cathode. As the anode, if the expected tungsten oxidation occurs, the pins should become less conductive due to the formation of an oxide cap; and the oxidation process should move rapidly to areas of initially higher resistance. As the cathode, the copper deposits continuously build up at all conducting pins with the lower resistance areas forming the larger deposits.

Both conditions described above have been observed. When the composites were used as the anode, the highly reflecting pins appeared in a short time and did not appear changed in size or number with additional time. Further, the highly reflecting areas were confined to individual fibers. As the cathode, copper deposits were apparent and increased in size with time. When photographed the deposits varied greatly in size (Figure 62a). The size variation was probably caused by



a) X200.

Reproduced from
best available copy.



b) X5500.

Figure 62. Scanning Electron Micrographs of Copper Electro-deposits on ZrO_2 -W, Sample 18-11, Slice 13.

three or four pins supplying electrons to the large deposits and the small ones being supplied by only one pin. Other possible explanations are variation in resistance of each pin or variation in contact of the gold film on the back of the wafer. The deposits did cover four or five pin spacings as can be seen in Figure 62b.

C. SUMMARY

In the preceding sections a wide variability of resistance values have been obtained for the oxide-metal composite samples. These values certainly reflect the difficulty achieving good electrical contact to the very fine metallic fibers and the probability that the samples contained some percentage of discontinuous (banded) eutectic growth. Some samples for emission testing have been extensively etched to expose very long fibers (Figure 68, Section V), and the SEM micrographs show a very large percentage of the fibers to be continuous. Work has just begun using metal brazing alloys to make electrical contact to composite samples with exposed pins, and the initial results indicate good wettability of the W and Mo fibers and significant decreases in the resistivity values reported above using indium and mercury contacts.

SECTION V

EXPERIMENTAL EMISSION MEASUREMENTS

This section discusses the experimentally observed high field electron emission characteristics of the oxide-metal composite materials. The experimental measurements were accomplished with a slightly modified version of the diode assembly previously described.² A variety of emitter configurations were tested for electron emission, and attempts were made to correlate the observed emission with emitter morphology. Lifetime (endurance) tests of a particularly promising emitter were initiated.

A description of the modified experimental apparatus is given, and the various experimental results are summarized. The observed correlation of the emission with emitter morphology and preliminary endurance test results are presented.

A. EXPERIMENTAL APPARATUS

Figure 63 shows an overall view of the experimental facility as it presently exists. Vacuum system controls are in the left-hand rack, and the various power supplies and emission measurement instrumentation are on the right side of the vacuum chamber. The experimental diode, previously described,² was slightly modified to improve the anode heat dissipation capability. This was accomplished through a change

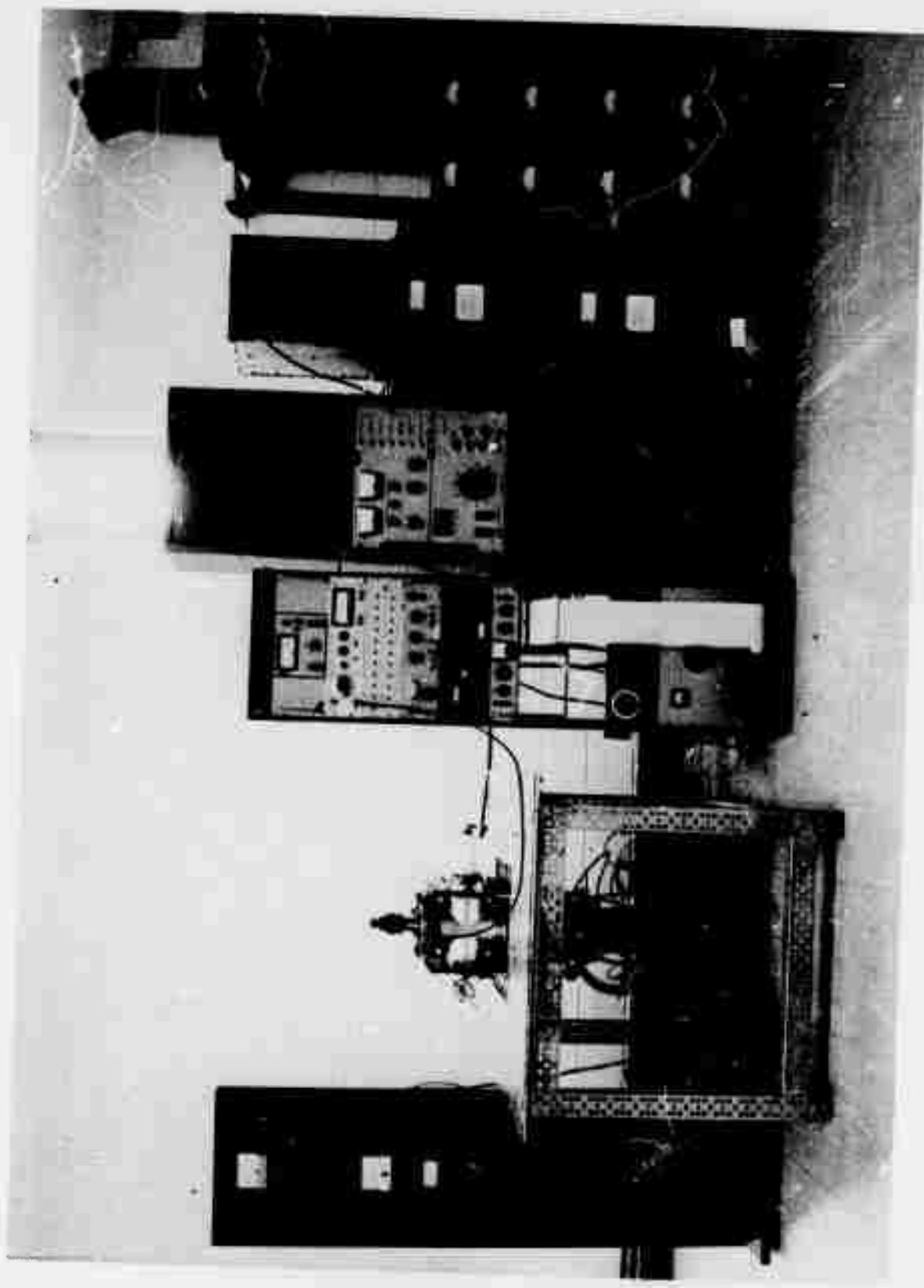


Figure 63. Overall view of the Experimental Apparatus.

in the method by which the anode was electrically isolated from the linear motion feedthrough. The steatite pillar approximately 2.5 cm long connecting the anode to the stainless steel feedthrough extension was removed and the feedthrough extension isolated from the feedthrough by a thin mica disc. The loss of 2.5 cm in overall anode assembly was made up by increasing the anode length; anodes of various configurations can be attached to the feedthrough extension.

B. ELECTRON EMISSION MEASUREMENTS

A chronological summary of the emission data together with important emitter characteristics for all samples tested since the last Semi-Annual Report¹ is given in Table IX . The primary objectives of the emission tests performed during this period were as follows:

- (a) Investigate unique emitter geometries including those having an unconventional emitting surface and those designed to produce internal current limiting.
- (b) Determine how to possibly improve the electrical connection to the back surface of the emitter, for example by the use of vapor deposited metallic coatings.
- (c) Obtain emission data for composites other than UO_2 -W, for example ZrO_2 -W.
- (d) Continue efforts to correlate electron emission with emitter microscopic morphology; this study was

initiated using the segmental collector assembly
¹
described previously.

- (e) Examine the effects of various anode configurations on electrical breakdown within the test diode.
- (f) Continue efforts to produce an emitter having maximum emission capability.

The most significant experimental results are discussed below with reference to the above objectives. Since a given experiment might make use of techniques developed in the course of other investigations, the following material often overlaps two or more of the stated objectives. Table IX should be consulted for the correct chronological order of the research.

1. Unique Emitter Geometry

The performance of exposed pin and flush pin type electron emitters was treated in the last Semi-Annual Report.¹ In order to complete the family of possible configurations, sample #13-45/11-13 having pins recessed below the emitter surface was prepared. Approximately 95% of the W pins were etched to an estimated depth of 20-30 microns. The remaining pins were poorly etched and were thus flush with the matrix. For equivalent interelectrode spacing and anode potential, the emission from the recessed pin sample was about 10^{-2} of the value obtained when the pins were flush and about 10^{-8} of the exposed pin value. When the interelectrode spacing was decreased to about 0.004 inch, current values typical of the maximum observed with emitters having flush pins were observed. It appears likely that the bulk of the emission originated from the poorly recessed pins.

TABLE IX

CHRONOLOGICAL SUMMARY OF EMISSION MEASUREMENTS

Date Installed	Sample Designation	Type of Composite	Emitter Configuration	Maximum Current Density mA/cm ²	Active Emitter Area cm ²	Remarks and Notes
10 Dec 1971	13-45/11-13	UO ₂ -W	Pins etched 20-30 below front surface	10	0.48	Made to complete series: exposed pins, flush pins, recessed pins.
12 Jan 1972	18-16/12	ZrO ₂ -W	flush pins	No significant current	0.45	Vapor gold coated back side.
18 Jan 1972	13-57/11-6	UO ₂ -W	exposed pins	80	0.01	0.5 inch diameter Mo anode and entire surface gold coated.
25 Jan 1972	13-57/11-6	UO ₂ -W	exposed pins	80	0.01	0.25 inch diameter Mo anode. Entire sample gold coated. Anode insulation modified.
4 Feb 1972	13-57/11-6	UO ₂ -W	exposed pins	80	0.01	0.5 inch diameter Pt Grid and Faraday cup. Entire sample gold coated.
4 Mar 1972	13-57/13-65	UO ₂ -W	exposed pins	90	0.05	Good growth characteristics.
20 Mar 1972	13-57/13-67	UO ₂ -W	Pins etched from back side	20	0.05	Attempt to introduce resistance by etching back side.
18 Apr 1972	18-11/13	ZrO ₂ -W	flush pins	6	0.05	Gold coated on back side surface. Later used in electrodeposition experiments.
9 May 1972	13-58/11-27	UO ₂ -W	exposed pins	18	0.08	0.125 inch diameter Mo anode used; sample larger than anode.
29 May 1972	13-57/11-31c	UO ₂ -W	exposed pins	200	0.02	Long fibers

A post-emission SEM micrograph of sample #13-45/11-13 is given in Figure 64. Note in addition to the area of severe arc damage, there are areas having flush pins and the degree of pin recession appears to be variable. Some of the difficulties in producing uniformly recessed pins are further considered later in this Section.

Vacuum breakdown in the field emission diode is caused either by intense localized heating leading to vaporization and ionization of the cathode material or by electron bombardment localized melting and ionization of the anode material. Both of these mechanisms have been advanced as the cause of vacuum breakdown.⁷ In either case breakdown can be prevented if the current per emitter pin is limited to some maximum value less than that required to initiate the breakdown process. Since the high field emission is strongly dependent upon the local electric field and hence the emitter-to-anode potential, a resistance in series with each pin could be used to limit the maximum current. If, for example, a particular pin had an unusually sharp point and tended to emit excessive current, the voltage drop across the series resistance would reduce the interelectrode potential and therefore decrease the emitted current. To be effective, however, each pin should have its individual resistor. With respect to the external circuit, individual pin resistances appear in parallel and therefore represent a small power loss.

One possible way of introducing such individual series resistances is by recessing the base of the W pins and utilizing the oxide matrix as the resistive element. A diagram of this

Reproduced from
best available copy.

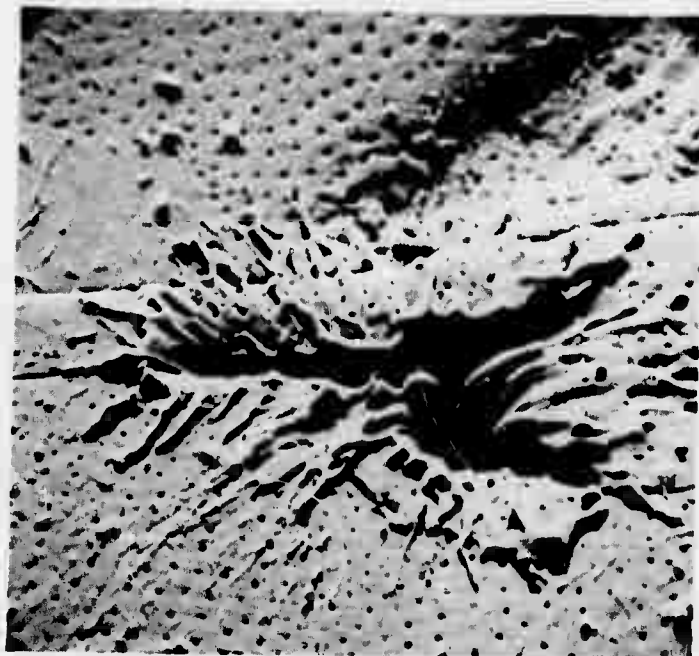


Figure 64. Scanning Electron Micrograph of UO_2 -W Sample 13-45/11-13 With Recessed Pins Showing Non-Uniform Pin Etching and Post Emission Damage. X2470.

emitter configuration and an approximate lumped parameter equivalent circuit are shown in Figure 65. A two-dimensional geometry is used for simplicity. The symmetrically distributed resistance between the cathode mount and the pin is designated R_s while the inter-pin resistance is R_p . From the equivalent circuit it is apparent that the required isolated individual pin in series with a resistance is approximated when $R_s \ll R_p$. However, R_s must still be large enough to effect the desired voltage drop. For the emitter geometry shown and a homogeneous isotropic matrix conductivity, the resistance inequality will be met if

$$t_2 \sim t_1$$

and

$$t \sim d$$

Since d is only a few microns, it is unlikely that such a situation could be completely realized. However, even if the ideal conditions were not realized, series resistance could be introduced that would be effective over a group of pins; and some improvement in breakdown characteristics might be noted. A UO_2 -W sample, #13-57/13-67, was fabricated to test this technique. By methods described in Section III the W pins were etched to a depth of about 50 microns. Since the pin spacing is about 4 microns the ideal situation was not realized. In addition, it is likely that areas along grain boundaries where the W fiber growth was discontinuous did not etch more than a few microns deep. Such boundaries would be of low resistance and would tend to "short out" the effects of the recessed pins.

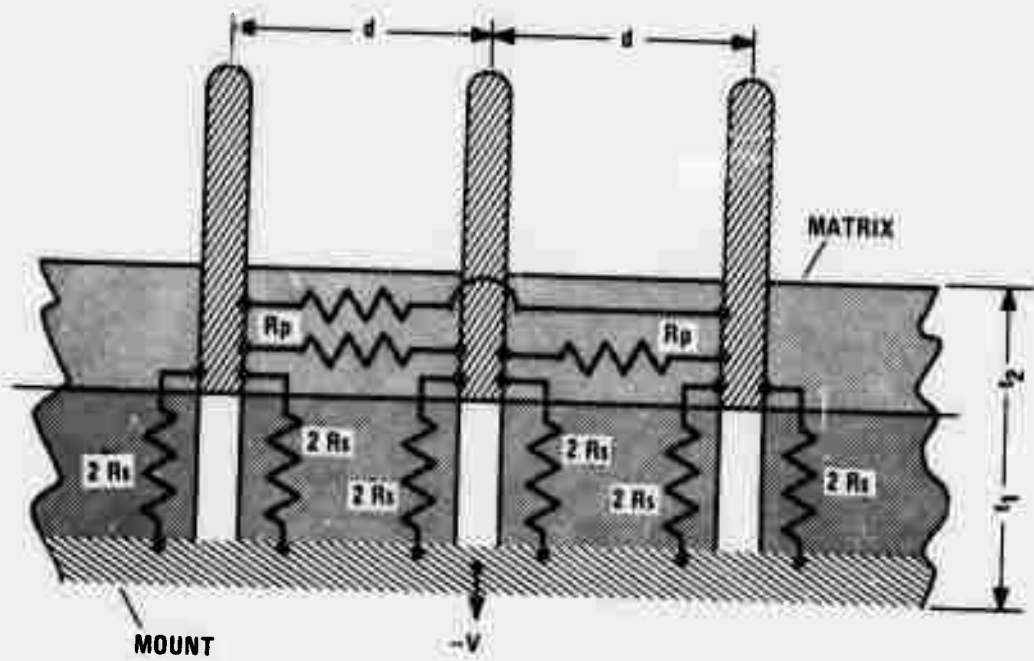


Figure 65a. Section of a Simplified Recessed Pin Type Emitter Showing Origin of Components of Matrix Resistance.

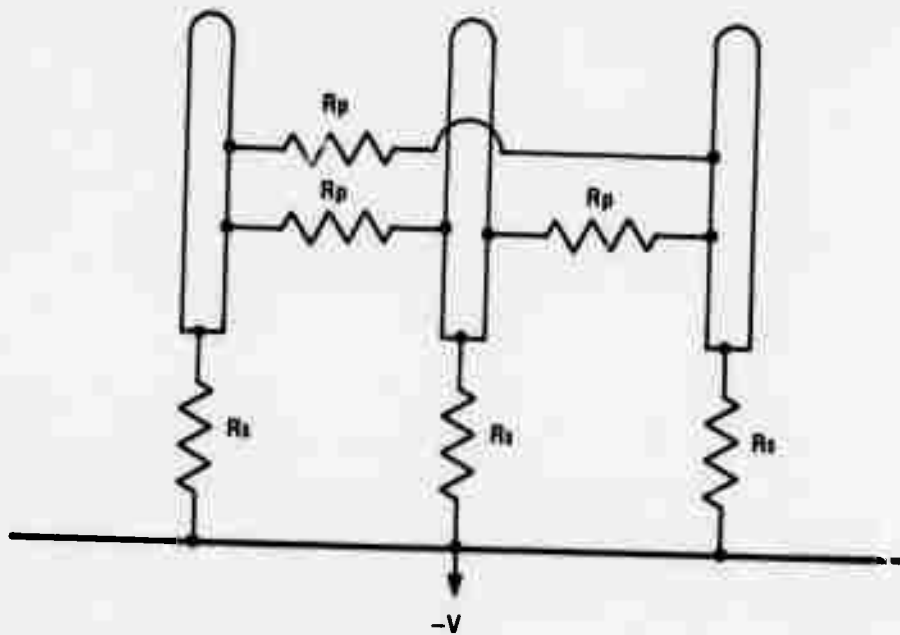


Figure 65b. Approximate Lumped Parameter Model of Emitter Pins and Oxide Matrix.

The emission performance of the base-recessed pin sample was below average. Only about 20 mA/cm^2 emission current could be obtained before vacuum breakdown occurred. Various combinations of anode potential and interelectrode spacing were tried in an effort to achieve the optimum performance. Although anode potentials in excess of 30 kV and spacings of 0.005 to 0.05 inch were employed, no significant improvement in emission was noted. The breakdown problem was not eliminated by the recessed pins.

The most logical explanation for the failure of this geometry is its poor approximation to the ideal case. The idea of current limiting resistance should not be discarded, but approaches such as the one outlined in Section IV should be tried.

2. ZrO₂-W Composite Type Electron Emitters

In the last Semi-Annual Report¹ it was noted that a ZrO₂-W composite had been tested as an emitter with unrepeatable results. In an effort to improve the emitter performance, sample #18-16/12 was coated with gold by vacuum evaporation over a portion of its back surface. This was the first sample to be so coated. The emission performance of this sample was very poor; no significant current could be detected. When the vacuum system was vented, it was found that the contact resistance between the sample and the support was quite variable and depended upon the mechanical pressure applied to the sample. After this experience the procedure of resistance testing samples prior to insertion in the diode fixture was usually followed.

The details of the method of resistance measurement are discussed in Section IV.

A third ZrO_2 -W type electron emitter (18-11/13) was grown and gold plated on the back surface to improve contact with the emitter pins. As in the case of Sample 18-16/12, the matrix was not etched so the pins were flush with both the front and back surfaces. Electrical resistance measurements indicated that the mounted sample had a resistance of 0.16 ohm. This resistance was significantly higher than the theoretical value, but was one of the lowest obtained with a mounted sample. The emission was measured for a variety of interelectrode spacings and anode potentials. The maximum recorded DC current density was about 6 mA/cm^2 . Measurements using 60 Hz AC gave similar data. Post-emission SEM micrographs of the sample are shown in Figure 66a. As in previously tested flush pin UO_2 -W type emitters, the arc damage is confined to a region about the pin sites. An effort was made to correlate the observed emission performance with pin continuity. The procedure involved is discussed below.

3. Correlation of Emission with Pin Continuity

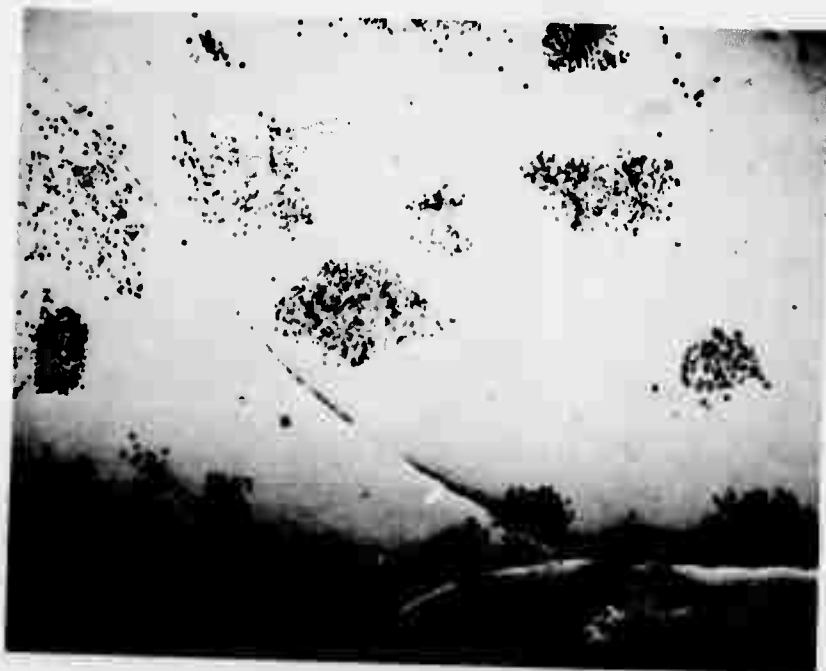
The correlation was made by plating Cu onto the pin tips in an electrolysis cell. The details of the procedure are given in Section IV. A brief summary is given here for completeness. The sample was first polished and then used as the cathode in a $CuSO_4$ electrolysis cell. Copper deposits formed on individual pins and small groups of pins in the same areas where arc damage

was evident. Photomicrographs of the emitter as removed from the deposition are shown in Figure 66. Since the process of copper plating is influenced by the strength of the local electric field in a manner analogous to electron emission, the copper would be expected to be preferentially deposited on those sites most favorable to electron emission. As can be seen from Figure 66 the electro-deposited copper provides a strong indication that electron emission is confined to a relatively small portion of the emitter area. As discussed in Section IV, the electro-deposition of copper is somewhat time dependent. This suggests that the emitter pins do not all have the same resistance, or that the pin geometry and hence local electric field varies greatly from pin to pin. Since SEM analyses have shown the pins to have nearly the same shape and in the sample under discussion all pins were polished flat, it would appear that gross differences in pin tip geometry are unlikely. Therefore, the preferential plating and electron emission from certain pin sites is probably due to variations in total pin resistance. The variation in pin resistance could be introduced in any of several ways. The connection between the pin base and the sample mount could be variable due to the failure of the gold coating to adhere equally to all pins. Another source of additional resistance could be the existence of very small breaks in the W fibers. Since the resistivity of bulk zirconia is very large, such breaks would have to be quite small. An additional possibility could be an extreme variation in the thickness of the W fibers. This latter condition seems improbable since



a) Post Emission Micrograph Showing Arc Damage, X50.

Reproduced from
best available copy.



b) Micrograph After Polishing and Immersion in CuSO_4 Electrolytic Cell for 2.5 Minutes with a Current of $2.5 \times 10^{-5} \text{ A}$, X50.

Figure 66. Micrographs of $\text{ZrO}_2\text{-W}$ Sample 18-11/13 Showing Correlation of Arc Damage with Pin Continuity.

dimensional variations of the required magnitude have not been observed.

Of the several hypotheses, the most reasonable appears to be that of the existence of a very small break in certain pins. This is favored over the contact resistance hypothesis because the emitting pins always appear to be confined to a single grain. If contact resistance were a problem, it would not be expected to be associated with any particular grain.

It is believed that gross resistance measurements coupled with electrolytic examinations of pin continuity will lead to a better understanding of pin growth and the development of more viable emitters.

4. Effects of Various Anode Configurations

The effects of various anode configurations was investigated with Sample #13-57/11-6 (UO_2 -W). The sample was vacuum overcoated with gold on its front surface. (See Figure 55) The front coating was an attempt to compensate for possible poor pin continuity by connecting all pins through the gold film. Three different anodes were used in testing this sample. Initial measurements were made with the steatite pillar insulated 0.5 inch diameter Mo anode having poor heat sinking properties. The anode insulation was changed to the thin mica disc discussed earlier, and measurements were made with a 0.25 inch Mo anode and a 0.5 inch diameter Pt grid anode supported by a stainless steel Faraday cup. In all cases approximately the same current density of 80 mA/cm^2 was observed before electrical breakdown.

Neither the application of the gold coating nor the use of different anodes seemed to materially affect the performance of the emitter.

5. High Current Emitter Development

From the general viewpoint, all work has been directed toward the production of a field emitter suitable for use in an electron device. Most of the emitters discussed above were, in addition, utilized to explore some specific aspect of composite field emitter technology. However, several emitters were fabricated with the expectation that they would exhibit superior electron emission.

Sample #13-57/13-65 (UO_2 -W) with growth characteristics shown in Figure 67 was tested for electron emission. This round sample had beveled edges and was approximately 0.05 cm^2 in area. The maximum current density obtained was about 90 mA/cm^2 .

It was thought that the recessed pin type emitter 13-57/13-67 discussed previously might have unusually good emission. The performance of this emitter, which was also round with an area of about 0.05 cm^2 , was below average.

The largest current density measured in the course of this work was obtained with Sample # 13-57/11-31C (UO_2 -W). As can be seen from Figure 68, the emitter has unusually long pins. The great degree of etching is indicated by the fibers visible along the edge and by the holes through the sample. No effort was made to sharpen the pins. Initial emission tests produced a maximum current density of over 200 mA/cm^2 . This current

Reproduced from
best available copy.



Figure 67. Pre-Emission Scanning Electron Micrograph of Sample No. 13-57/13-65 (UO₂-W). X52.



a) View of Sample
Showing Long
Pins Exposed
Near Edge. X245.



b) Interior of
Sample. X4400.

Figure 68. Pre-Emission Scanning Electron Micrographs of Sample No. 13-57/11-31C (UO_2 -W).

density was 100% larger than the highest previously obtained. A graphical comparison of sample #13-57/11-31C to a sample typical of past performance is presented in Figure 69.

No attempt was made to extract maximum current from the composite; the interelectrode spacing and anode potential were adjusted to obtain stable emission of about 100 mA/cm^2 . A strip-chart recorder was then connected to the electrometer to provide a continuous record of the emitter performance. Data from the recorder sampled at 24 hour intervals are given in Figure 70. It can be seen that the emission current initially increased and then remained steady within about $\pm 5\%$ for about 10 days after which it increased steadily until the current limiting series resistor failed. Since the series resistor was of the composition carbon type, failure was probably preceded by a decrease in resistance value. This caused the anode potential to increase and the current to behave as indicated in Figure 70. At a sufficiently high power dissipation the carbon resistor cracked and open circuited, thus terminating the experiment.

Post-emission scanning electron micrographs of the sample are shown in Figure 71. A low magnification overall view showing areas of arc damage is given in Figure 71a. It is believed that the majority of these arcs occurred during initial measurements prior to initiating the endurance test. Examination of the 0.125 inch diameter Mo anode after removal of the test diode from the vacuum chamber showed that it was not perfectly centered over the emitter, but was slightly displaced toward one

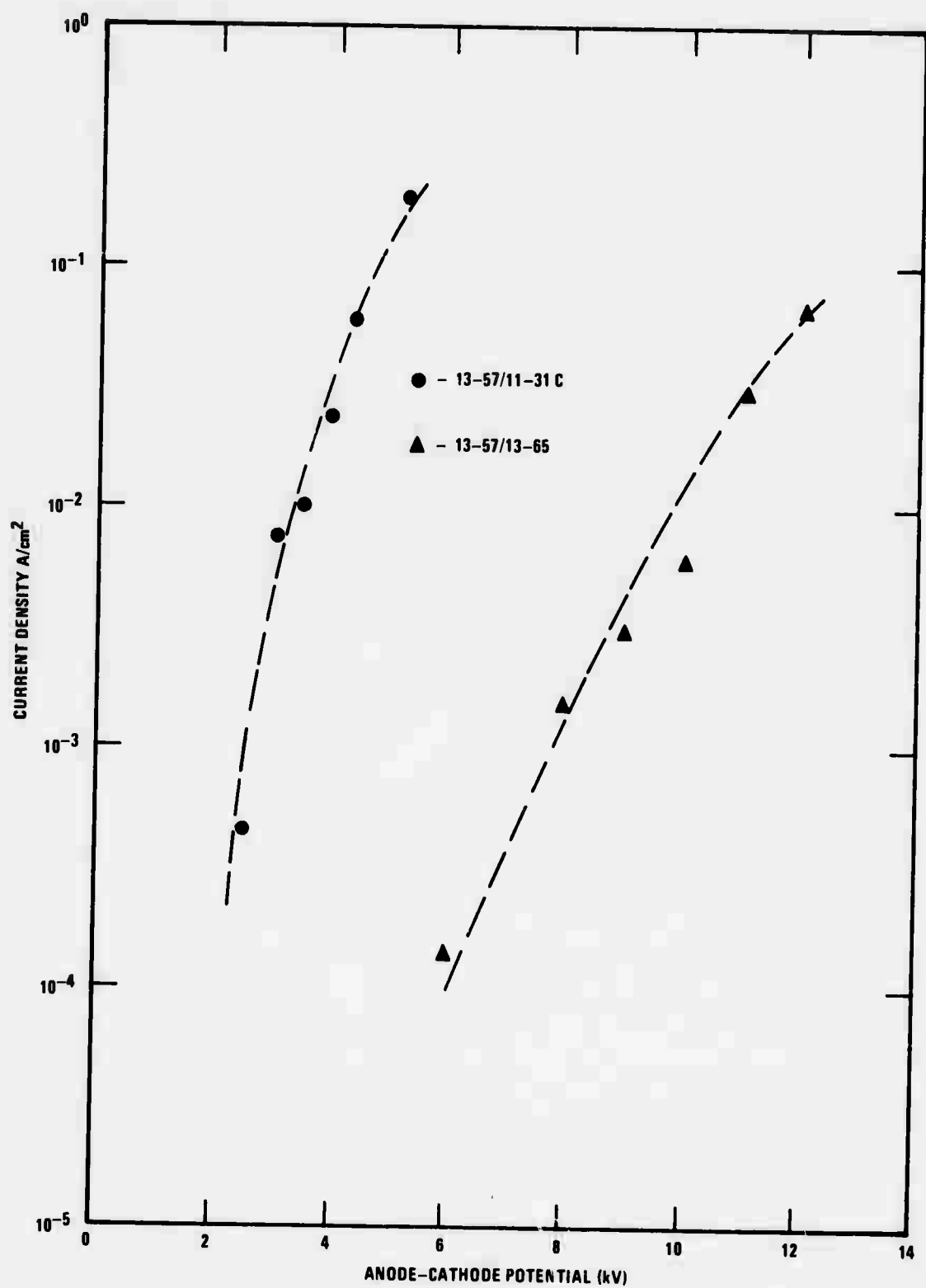


Figure 69. High Field Electron Emission Current Density for Two Different UO_2 -W Samples. Anode-to-Cathode Spacing 0.030-Inch Both Cases.

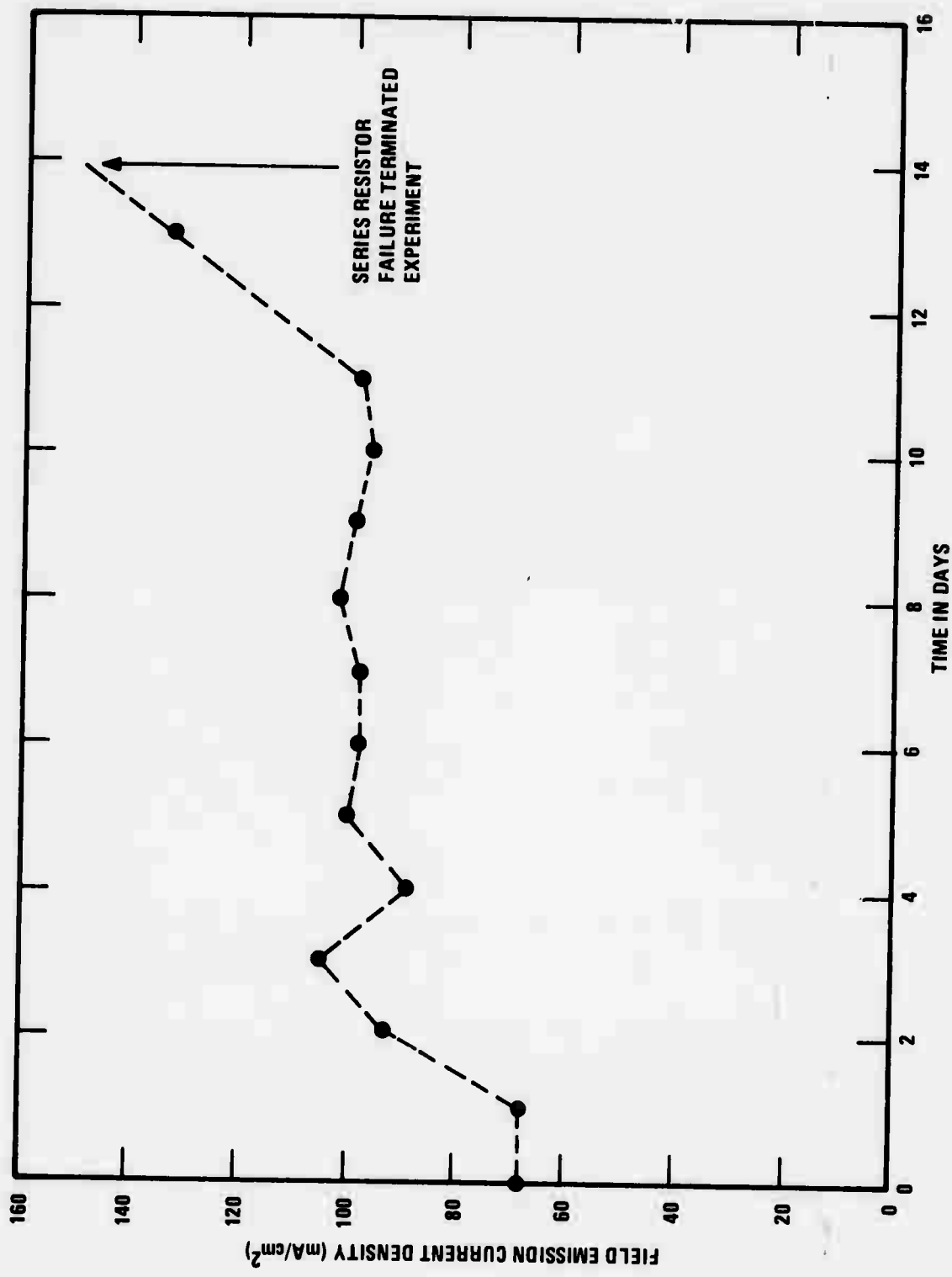
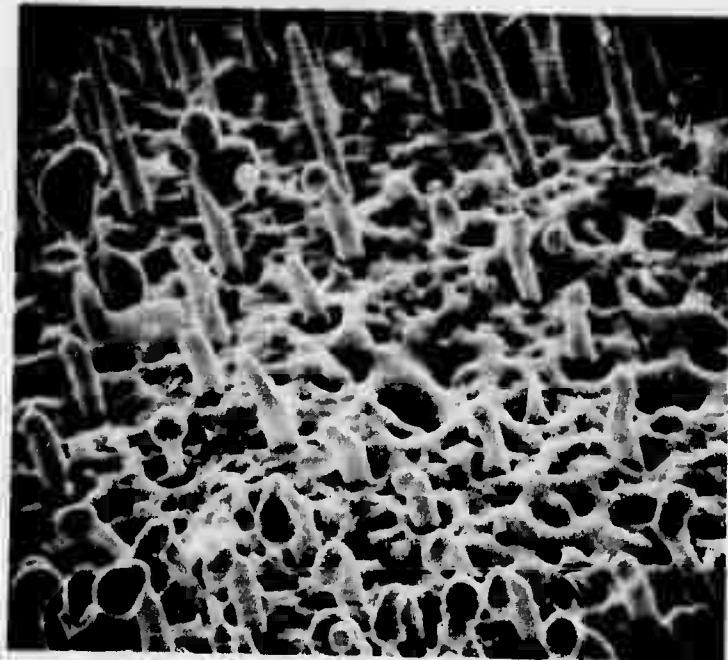


Figure 70. Field Emission Current Density as a Function of Time for $\text{UO}_2\text{-W}$, Sample 13-57/11-31C.



a) Overall View of Sample Showing Areas of Arc Damage. X48.

Reproduced from
best available copy.



b) High Magnification View of Arc Damage Area. X4875.

Figure 71. Post Emission Scanning Electron Micrographs of Sample 13-57/11-31C (UO_2-W).

corner. This could account for the lack of arcs on the upper left corner of the sample as seen in Figure 71a. Figure 71b shows the arc damage at higher magnification. The appearance here is typical of that observed with other emitter samples.

Qualitatively Sample 18-57/11-31C was the best electron emitter yet tested. There was never any difficulty in obtaining emission current densities in the 100 mA/cm^2 range. The emission current appeared to be quite reproducible; and arcs, when they occurred, had relatively little effect on the available current. The current density of 100 mA/cm^2 , which has previously been obtained for only a few minutes during test runs was recorded for over 300 hours of continuous operation with no degradation in performance. There is reason to believe that this current could have been maintained at this value for an even longer period had not the series resistor failed.

Of prime importance is the reason for the unusually good performance of this emitter. As can be seen from Figures 68 and 71, the emitter pins, while long, are typical of several previous samples. Thus, pin configuration is probably not the unique factor. It appears more probable that the high emission was due to good growth characteristics, particularly to superior pin continuity. If this is indeed the case, further improvement in emitter morphology and pin continuity should result in a corresponding increase in available emission current.

SECTION VI

THEORETICAL ANALYSIS OF ELECTRON EMITTING ARRAYS

In an earlier study,⁸ the calculation of the electrostatic potential distribution surrounding a square array of charged surface states on an insulating dielectric substrate was presented. The potential was determined by imaging the surface states through a grounded conducting planar anode and by solving the appropriate Poisson equation by using a harmonic mode expansion of the potential distribution in each cell which consisted of a surface state and its image. The resulting undetermined coefficients in the series expansions were computed by applying the Neumann boundary conditions at every common cell interface. The resulting form of the solution for the potential distribution was a double Fourier series.

In a later study¹, the surface charge states were replaced with the finite conducting pins of the actual device, which protrude out of the insulating dielectric substrate. Therefore, an attempt was made to generalize the earlier model to include the more important parameters of the pins themselves, e.g. pin shapes, pin heights, and pin cross-sectional areas, which were not present in the earlier model. This generalization of the earlier model, of course, severely complicated the problem and necessitated the use of several approximations in order to obtain a solution in a useable form. Several mathematical

models were developed to calculate the potential distribution in the neighborhood of the conducting pins. An actual three-dimensional solution was not obtained; instead, two orthogonal cross-sectional cuts of the device were analyzed. In each case, the appropriate Laplace equation was separated in a rectangular coordinate system. Each resulting separated equation was then solved by using a harmonic mode expansion. The resulting undetermined coefficients in the recombined product series expansion were computed by applying the continuity conditions on the potential and its first derivative at all common interfaces. The resulting form of the solution for the potential distribution was a double Fourier series.

A. MODELS

Previously, the potential distribution in the neighborhood of the pin tips was calculated by analytical methods only; now, however, due to the complexity of the geometry being considered, a purely numerical approach is being considered. It was observed in the previous studies that the analysis was complicated by the periodicity of the structure and by the closeness of the planar anode structure above the pins. The solution to the Laplace equation for a device with non-periodic spacings of the pins, or with pins of a geometry for which the Laplace equation is inseparable, is very complicated if not impossible to solve, and at best will produce a solution in the form of a slowly converging infinite series. An alternate approach to this

problem is to solve the Laplace equation by a purely numerical-type solution and to implement this solution on a high speed computer.

The earlier mathematical models, which were convenient for purely analytical techniques, must now be modified somewhat if they are to remain suitable for numerical computations. Each of the earlier models had several sharp edges, which were not actually physically realizable but were well suited for analytical computations and lead to convenient boundary conditions. In the neighborhood of these edges, the potential approaches some finite value; but the electric field intensity, which is the negative gradient of the potential at that point and which is now calculated by a numerical differentiation technique, becomes very large and is very difficult to evaluate. Therefore, new models with essentially the same features as the old models, except that they have no edges, are being considered.

1. Prolate Spheroids

Each individual pin is modeled by an appropriately oriented and adjusted prolate spheroid. The major axis of each spheroid is perpendicular to the insulating substrate matrix, and the minor axis of each spheroid is in the plane of the substrate. The parameters to be varied in this model are the heights of the pins above the substrate and the cross-sectional areas of the pins, i.e. the major and minor axis of the spheroids. Various realistic pin shapes can be approximated by this model.

The following development presents the exact analytical solution for a single prolate spheroidal emitter pin. Since emitter arrays are composed of many pins, this analysis is not directly applicable to the case of prime interest. However, the exact solution is very useful as a test problem while the numerical method is under development. In addition, it is quite interesting to compare the emission from a superposition of single pins with that of the actual array and thus gain some insight into the magnitude of electric field reduction that occurs when pins are placed in close proximity.

Referring to Figure 72, let ℓ by the length of the major axis of the spheroid. If z_0 is the height of the top half of the spheroid above the xy plane and if ρ_0 is the radius of the cross section of the spheroid at the xy plane, then

$$\ell = \sqrt{z_0^2 - \rho_0^2}$$

Also, if the distances from the upper and lower foci of the spheroid to the point r on the surface of the spheroid are denoted by r_+ and r_- , respectively, then the following definitions can be made:

$$u = \frac{r_+ + r_-}{2\ell} \equiv \cosh \zeta$$

$$v = \frac{r_+ - r_-}{2\ell} \equiv \cos \eta$$

It can be shown that

$$\begin{aligned} z &= \ell \cosh \zeta \cos \eta & = \ell u v \\ \rho &= \ell \sinh \zeta \sin \eta & = \ell \sqrt{u^2 - 1} \sqrt{1 - v^2} \\ \left\{ \begin{aligned} x &= \ell \sinh \zeta \sin \eta \cos \varphi & = \ell \sqrt{u^2 - 1} \sqrt{1 - v^2} \cos \varphi \\ y &= \ell \sinh \zeta \sin \eta \sin \varphi & = \ell \sqrt{u^2 - 1} \sqrt{1 - v^2} \sin \varphi \end{aligned} \right. \end{aligned}$$

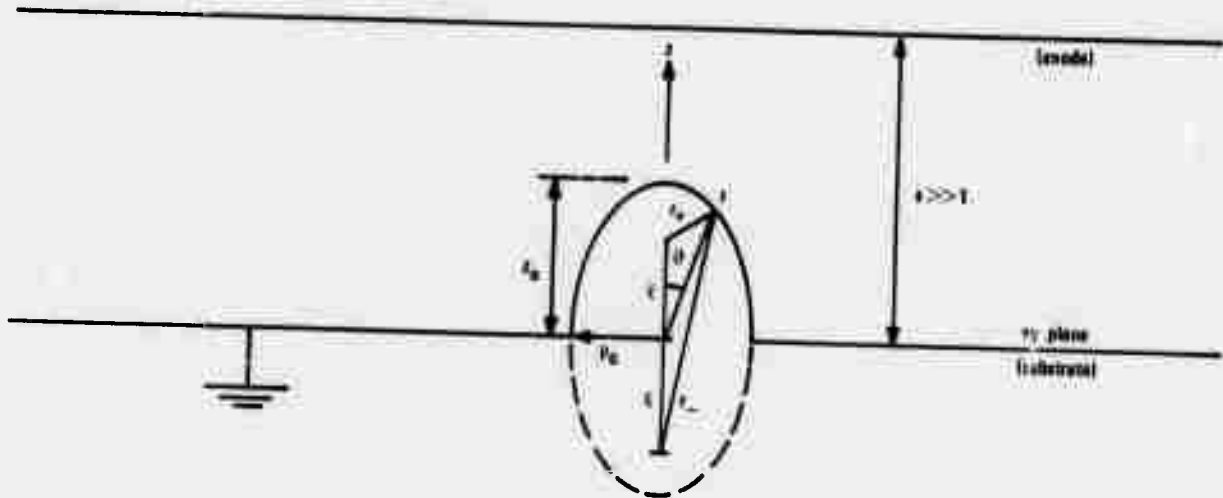


Figure 72. Prolate Spheroidal Model.

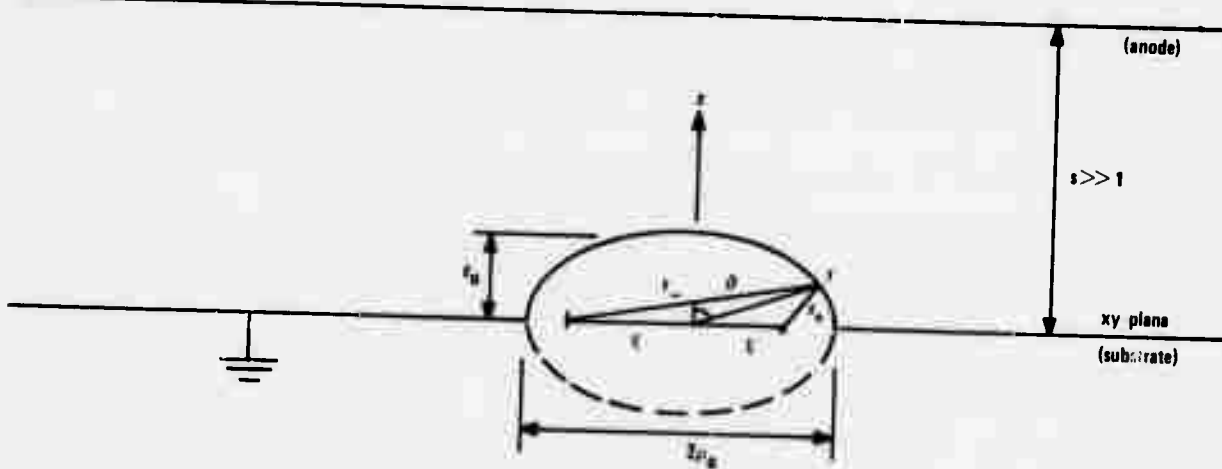


Figure 73. Oblate Spheroidal Model.

and that

$$\left(\frac{z}{\cosh \zeta}\right)^2 + \left(\frac{\rho}{\sinh \zeta}\right)^2 = \ell^2$$

$$\left(\frac{z}{\cos \eta}\right)^2 - \left(\frac{\rho}{\sin \eta}\right)^2 = \ell^2$$

Therefore, $\zeta = \text{constant}$ curves are ellipses, and $\eta = \text{constant}$ curves are hyperbolas.

Fortunately, the Laplace equation

$$\nabla^2 \Phi = 0$$

where

$$\nabla^2 = \frac{1}{\ell^2(u^2 - v^2)} \left[-\frac{\partial}{\partial u} (1 - u^2) \frac{\partial}{\partial u} + \frac{\partial}{\partial v} (1 - v^2) \frac{\partial}{\partial v} - \frac{u^2 - v^2}{(1-u^2)(1-v^2)} \frac{\partial^2}{\partial \varphi^2} \right]$$

is separable in a prolate spheroidal coordinate system. Therefore, let

$$\Phi = UV\varphi$$

where U, V, φ are functions of u, v, φ alone, respectively.

After substituting the separated Φ into the Laplace equation and separating the variables, there results three uncoupled ordinary differential equations

$$\begin{aligned} \left[\frac{\partial^2}{\partial \varphi^2} + n^2 \right] \varphi &= 0 \\ \left[\frac{\partial}{\partial u} (1 - u^2) \frac{\partial}{\partial u} - \frac{u^2}{1 - u^2} + m(m + 1) \right] U &= 0 \\ \left[\frac{\partial}{\partial v} (1 - v^2) \frac{\partial}{\partial v} - \frac{v^2}{1 - v^2} + m(m + 1) \right] V &= 0 \end{aligned}$$

The solutions of these equations are

$$U_{mn} = a_1 P_m^n(\cosh \zeta) + a_2 Q_m^n(\cosh \zeta)$$

$$V_{mn} = b_1 P_m^n(\cos \eta) + b_2 Q_m^n(\cos \eta)$$

$$\varphi_n = c_1 \cos n\varphi + c_2 \sin n\varphi$$

where P_m^n and Q_m^n are the associated Legendre polynomials of the first and second kinds, and m and n are integers.

A suitable form of the solution is a linear combination of the product functions

$$\Phi = \sum_{m=0}^{\infty} \sum_{n=-m}^{n=m} C_{mn} U_{mn} V_{mn} \phi_n$$

The constants C_{mn} can be found by applying the boundary conditions to the potential

$$\Phi = V_o = E_o z \quad z \gg 1$$

$$\Phi = 0 \quad z = 0$$

$$\Phi = 0 \quad \zeta = \zeta_o \quad u = u_o$$

The results of applying the boundary conditions are

$$\Phi = E_o z \left[1 - \frac{\coth^{-1} u - \frac{1}{u}}{\coth^{-1} u_o - \frac{1}{u_o}} \right] = E_o z \left[1 - \frac{\coth^{-1}(\cosh \zeta) - \operatorname{sech} \zeta}{\coth^{-1}(\cosh \zeta_o) - \operatorname{sech} \zeta_o} \right]$$

where

$$u_o = \frac{z_o}{\sqrt{z_o^2 - \rho_o^2}}$$

$$\zeta_o = \cosh^{-1} \frac{z_o}{\sqrt{z_o^2 - \rho_o^2}}$$

and

$$E_o = \frac{V_o}{s}$$

The electric field intensity can be determined by taking the negative gradient of the potential distribution

$$\mathbf{E} = -\nabla \Phi = -\left(\hat{u} \frac{1}{\ell} \sqrt{\frac{u^2 - 1}{u^2 - v^2}} \frac{\partial}{\partial u} + \hat{v} \frac{1}{\ell} \sqrt{\frac{1 - v^2}{u^2 - v^2}} \frac{\partial}{\partial v} + \hat{\varphi} \frac{1}{\ell \sqrt{u^2 - 1} \sqrt{1 - v^2}} \frac{\partial}{\partial \varphi} \right) \Phi$$

where

$$\hat{u} = \frac{1}{\sqrt{u^2 - v^2}} (\hat{u} \sqrt{1 - v^2} + \hat{z} v \sqrt{u^2 - 1})$$

$$\hat{v} = \frac{1}{\sqrt{u^2 - v^2}} (-\hat{u} v \sqrt{u^2 - 1} + \hat{z} u \sqrt{1 - v^2})$$

$$\hat{\phi} = \hat{\phi}$$

The non-zero components of the electric field are

$$E_u = -E_o v \sqrt{\frac{u^2 - 1}{u^2 - v^2}} \left[1 - \frac{\coth^{-1} u - \frac{u}{u^2 - 1}}{\coth^{-1} u_o - \frac{1}{u_o}} \right] = -\frac{\sinh \zeta_o \cos \eta}{\sqrt{\cosh^2 \zeta_o - \cos^2 \eta}} \left[1 - \frac{\coth^{-1}(\cosh \zeta) - \frac{\cosh \zeta}{\sinh^2 \zeta}}{\coth^{-1}(\cosh \zeta_o) - \frac{\cosh \zeta_o}{\sinh^2 \zeta_o}} \right]$$

$$E_v = -E_o \sqrt{\frac{1 - v^2}{u^2 - v^2}} \left[1 - \frac{\coth^{-1} u - \frac{1}{u}}{\coth^{-1} u_o - \frac{1}{u_o}} \right] = -\frac{\sin \eta \cosh \zeta}{\sqrt{\cosh^2 \zeta_o - \cos^2 \eta}} \left[1 - \frac{\coth^{-1}(\cosh \zeta) - \frac{\cosh \zeta}{\sinh^2 \zeta}}{\coth^{-1}(\cosh \zeta_o) - \frac{\cosh \zeta_o}{\sinh^2 \zeta_o}} \right]$$

On the surface of the spheroid, the only non-zero component of the electric field is

$$E_u \Big|_{\substack{u=u_o \\ \zeta=\zeta_o}} = -\frac{\sqrt{\frac{u_o^2 - 1}{u_o^2 - v^2}}}{v} \left[1 - \frac{\coth^{-1} u_o - \frac{u_o}{u_o^2 - 1}}{\coth^{-1} u_o - \frac{1}{u_o}} \right] = -\frac{\sinh \zeta_o \cos \eta}{\sqrt{\cosh^2 \zeta_o - \cos^2 \eta}} \left[1 - \frac{\coth^{-1}(\cosh \zeta_o) - \frac{\cosh \zeta_o}{\sinh^2 \zeta_o}}{\coth^{-1}(\cosh \zeta_o) - \frac{\cosh \zeta_o}{\sinh^2 \zeta_o}} \right]$$

The electric field intensity given above can be used in the calculations for the total emitted current. This single pin model of the actual device will give some insight into the accuracy of the numerical solutions.

2. Oblate Spheroids

In addition to the prolate spheroidal model, an oblate spheroidal model is occasionally useful. For example, after arcing the pin geometries no longer fit a prolate spheroidal model, since the pin height is usually not greater than the pin radius. In this situation the oblate spheroidal model,

in which it is assumed that the pin height is less than the pin radius, is valid.

There are a few small but important differences between the prolate and oblate models, which will be pointed out now. Each individual pin is modeled by an appropriately oriented and adjusted oblate spheroid. The minor axis of each spheroid is perpendicular to the insulating substrate matrix, and the major axis of each spheroid is in the plane of the substrate. The parameters to be varied in this model are the heights of the pins above the substrate and the cross-sectional areas of the pins, i.e. the major and minor axis of the spheroids. The exact analytical solution for the single pin case is discussed below.

Referring to Figure 73, let ℓ be the length of the major axis of the spheroid. If z_0 is the height of the top half of the spheroid above the xy plane, and if a_0 is the radius of the cross section of the spheroid at the xy plane, then

$$\ell = \sqrt{\frac{2}{a_0^2 - z_0^2}} \quad a_0 > z_0$$

Also, if the distances from the right and left foci of the spheroid to the point r on the surface of the spheroid are denoted by r_+ and r_- , respectively, then the following definitions can be made:

$$u \equiv \frac{r_+ + r_-}{2\ell} \equiv \cosh \zeta \quad u \geq 1$$

$$v \equiv \frac{r_+ - r_-}{2\ell} \equiv \cos \eta \quad |v| \leq 1$$

It can be shown that

$$\begin{aligned}
 z &= \ell \sinh \zeta \sin \eta & = \ell \sqrt{u^2 - 1} \sqrt{1 - v^2} \\
 \rho &= \ell \cosh \zeta \cos \eta & = \ell u v \\
 x &= \ell \cosh \zeta \cos \eta \cos \varphi & = \ell u v \cos \varphi \\
 y &= \ell \cosh \zeta \cos \eta \sin \varphi & = \ell u v \sin \varphi
 \end{aligned}$$

and that

$$\begin{aligned}
 \left(\frac{\rho}{\cosh \zeta} \right)^2 + \left(\frac{z}{\sinh \zeta} \right)^2 &= \ell^2 \\
 \left(\frac{\rho}{\cos \eta} \right)^2 - \left(\frac{z}{\sin \eta} \right)^2 &= \ell^2
 \end{aligned}$$

Therefore, $\zeta = \text{constant}$ curves are ellipses, and $\eta = \text{constant}$ curves are hyperbolas. Fortunately, the Laplace equation

$$\nabla^2 \Phi = 0$$

where

$$\nabla^2 = \frac{1}{\ell^2(u^2 - v^2)} \left[\frac{\sqrt{u^2-1}}{u} \frac{\partial}{\partial u} u \sqrt{u^2-1} \frac{\partial}{\partial u} + \frac{\sqrt{1-v^2}}{v} \frac{\partial}{\partial v} v \sqrt{1-v^2} \frac{\partial}{\partial v} + \frac{u^2-v^2}{u^2 v^2} \frac{\partial^2}{\partial \varphi^2} \right]$$

is separable in an oblate spheroidal coordinate system. Therefore, let

$$\Phi = U V \phi$$

where U, V, ϕ are functions of u, v, φ alone, respectively.

After substituting the separated Φ into the Laplace equation and separating the variables, there results three uncoupled ordinary differential equations.

$$\begin{aligned}
 \left[\frac{\partial^2}{\partial \varphi^2} + n^2 \right] \phi &= 0 \\
 \left[\frac{\sqrt{u^2-1}}{u} \frac{\partial}{\partial u} u \sqrt{u^2-1} \frac{\partial}{\partial u} + \frac{n^2}{u^2} - m(m+1) \right] U &= 0 \\
 \left[\frac{\sqrt{1-v^2}}{v} \frac{\partial}{\partial v} v \sqrt{1-v^2} \frac{\partial}{\partial v} - \frac{n^2}{v^2} + m(m+1) \right] V &= 0
 \end{aligned}$$

To simplify the equations in U and V , let

$$\begin{aligned} u' &\equiv i\sqrt{u^2-1} \\ v' &\equiv \sqrt{1-v^2} \end{aligned}$$

After making this change of variables, the equations in U and V become

$$\begin{aligned} \left[\frac{\partial}{\partial u'} (1-u'^2) \frac{\partial}{\partial u'} - \frac{n^2}{1-u'^2} + m(m+1) \right] U &= 0 \\ \left[\frac{\partial}{\partial v'} (1-v'^2) \frac{\partial}{\partial v'} - \frac{n^2}{1-v'^2} + m(m+1) \right] V &= 0 \end{aligned}$$

The solutions of these equations are

$$U_{mn} = a_1 P_m^n(u') + a_2 Q_m^n(u')$$

$$V_{mn} = b_1 P_m^n(v') + b_2 Q_m^n(v')$$

$$\phi_n = c_1 \cos n\varphi + c_2 \sin n\varphi$$

where P_m^n and Q_m^n are the associated Legendre Polynomials of the first and second kinds, and m and n are integers.

In terms of u and v or ξ and η

$$U_{mn} = a_1 P_m^n(i\sqrt{u^2-1}) + a_2 Q_m^n(i\sqrt{u^2-1}) = a_1 P_m^n(i \sinh \xi) + a_2 Q_m^n(i \sinh \xi)$$

$$V_{mn} = b_1 P_m^n(\sqrt{1-v^2}) + b_2 Q_m^n(\sqrt{1-v^2}) = b_1 P_m^n(\sin \eta) + b_2 Q_m^n(\sin \eta)$$

$$\phi_n = c_1 \cos n\varphi + c_2 \sin n\varphi$$

A suitable form of the solution is a linear combination of the product functions

$$\phi = \sum_{m=0}^{\infty} \sum_{n=-m}^{n=m} C_{mn} U_{mn} V_{mn} \phi_n$$

The constants C_{mn} can be found by applying the boundary conditions to the potential

$$\Phi = V_o = E_o z \quad z \gg 1$$

$$\Phi = 0 \quad z = 0$$

$$\Phi = 0 \quad \zeta = \zeta_o \quad u = u_o$$

The results of applying the boundary conditions are

$$\Phi = E_o z \quad \left[1 - \frac{\cot^{-1} \sqrt{u^2 - 1} - \sqrt{u^2 - 1}}{\cot^{-1} \sqrt{u_o^2 - 1} - \sqrt{u_o^2 - 1}} \right] = E_o z \quad \left[1 - \frac{\cot^{-1} (\sinh \zeta) - \operatorname{csch} \zeta}{\cot^{-1} (\sinh \zeta_o) - \operatorname{csch} \zeta_o} \right]$$

where

$$u_o = \frac{p_o^2}{\sqrt{\frac{p_o^2}{u_o^2} - z_o^2}}$$

$$\zeta_o = \cosh^{-1} \frac{p_o}{\sqrt{\frac{p_o^2}{u_o^2} - z_o^2}}$$

and

$$E_o = \frac{V_o}{s}$$

The electric field intensity can be determined by taking the negative gradient of the potential distribution

$$\mathbf{E} = -\nabla \Phi = -\left[\hat{u} \frac{1}{\ell} \sqrt{\frac{u^2 - 1}{u^2 - v^2}} \frac{\partial}{\partial u} + \hat{v} \frac{1}{\ell} \sqrt{\frac{1 - v^2}{u^2 - v^2}} \frac{\partial}{\partial v} + \hat{\phi} \frac{1}{\ell} \frac{1}{u - v} \frac{\partial}{\partial \phi} \right] \Phi$$

where

$$\hat{u} = \frac{1}{\sqrt{\frac{u^2}{u_o^2} - 1}} (\hat{p} v \sqrt{u^2 - 1} + \hat{z} u \sqrt{1 - v^2})$$

$$\hat{v} = \frac{1}{\sqrt{\frac{u^2}{u_o^2} - 1}} (\hat{p} u \sqrt{1 - v^2} - \hat{z} v \sqrt{u^2 - 1})$$

$$\hat{\phi} = \hat{\phi}$$

The non-zero components of the electric field are

$$E_u = -\sqrt{\frac{1-v^2}{u^2-v^2}} u E_o \left[1 - \frac{\cot^{-1} \sqrt{\frac{u^2-1}{v^2-1}} - \frac{\sqrt{u^2-1}}{\sqrt{v^2-1} + 1}}{\cot^{-1} \sqrt{\frac{u^2-1}{v^2-1}} - \frac{1}{\sqrt{\frac{u^2-1}{v^2-1}}}} \right] = -\frac{\cosh \zeta \sin \eta E_o}{\sqrt{\cosh^2 \zeta - \cos^2 \eta}} \left[1 - \frac{\cot^{-1}(\sinh \zeta) - \frac{\sinh \zeta}{1 + \sinh \zeta}}{\cot^{-1}(\sinh \zeta_o) - \frac{\cosh \zeta_o}{\sinh \zeta_o}} \right]$$

$$E_v = \sqrt{\frac{u^2-1}{u^2-v^2}} v E_o \left[1 - \frac{\cot^{-1} \sqrt{\frac{u^2-1}{v^2-1}} - \frac{\sqrt{u^2-1}}{\sqrt{v^2-1}}}{\cot^{-1} \sqrt{\frac{u^2-1}{v^2-1}} - \frac{1}{\sqrt{\frac{u^2-1}{v^2-1}}}} \right] = \frac{\cos \eta \sinh \zeta}{\sqrt{\cosh^2 \zeta - \cos^2 \eta}} E_o \left[1 - \frac{\cot^{-1}(\sinh \zeta) - \frac{\sinh \zeta}{1 + \sinh \zeta}}{\cot^{-1}(\sinh \zeta_o) - \frac{\cosh \zeta_o}{\sinh \zeta_o}} \right]$$

On the surface of the spheroid, the only non-zero component of the electric field is

$$E_u \Big|_{u=u_o} = -\sqrt{\frac{1-v^2}{u_o^2-v^2}} u_o E_o \left[1 - \frac{\cot^{-1} \sqrt{\frac{u_o^2-1}{v^2-1}} - \frac{\sqrt{u_o^2-1}}{\sqrt{v^2-1} + 1}}{\cot^{-1} \sqrt{\frac{u_o^2-1}{v^2-1}} - \frac{1}{\sqrt{\frac{u_o^2-1}{v^2-1}}}} \right] = -\frac{\cosh \zeta_o \sin \eta E_o}{\sqrt{\cosh^2 \zeta_o - \cos^2 \eta}} \left[1 - \frac{\cot^{-1}(\sinh \zeta_o) - \frac{\sinh \zeta_o}{1 + \sinh \zeta_o}}{\cot^{-1}(\sinh \zeta_o) - \frac{\cosh \zeta_o}{\sinh \zeta_o}} \right]$$

The electric field intensity given above can be used in the calculations for the total emitted current. This single pin model of the actual device after arcing can also give insight into the accuracy of the numerical solutions.

B. NUMERICAL SOLUTIONS

1. Potential Distribution

A numerical method has been developed to solve the Laplace equation for any three-dimensional geometry. This method was used to calculate the electrostatic potential inside a closed

volume with known boundary conditions on the surface enclosing the volume. Inside this region there may be no free charges; however, there may be numerous conducting obstacles, such as emitting pins.

a. Test Problem

In order to check the accuracy of the numerical method, a test run was made with a geometry for which the exact solution of the potential distribution was known analytically. Since the actual problem of interest with typical emitter geometries is so complex, an exact analytical calculation was not possible; therefore, a much simpler example, one in which an exact answer could be found, was used.

The test problem chosen was that of a hollow grounded conducting box of sides x_o , y_o , and z_o centered about the origin of a rectangular coordinate system as shown in Figure 74. The top of the box was insulated from the sides of the box and was held at a fixed potential

$$v_o \sin \frac{\pi}{x_o} x \sin \frac{\pi}{y_o} y$$

This test problem does not, unfortunately, approximate in any way the actual problem of interest, but does provide a check on the accuracy of the numerical method itself. (Only simple problems of this nature can be solved exactly.)

First, the exact analytical solution for the test problem will be developed.

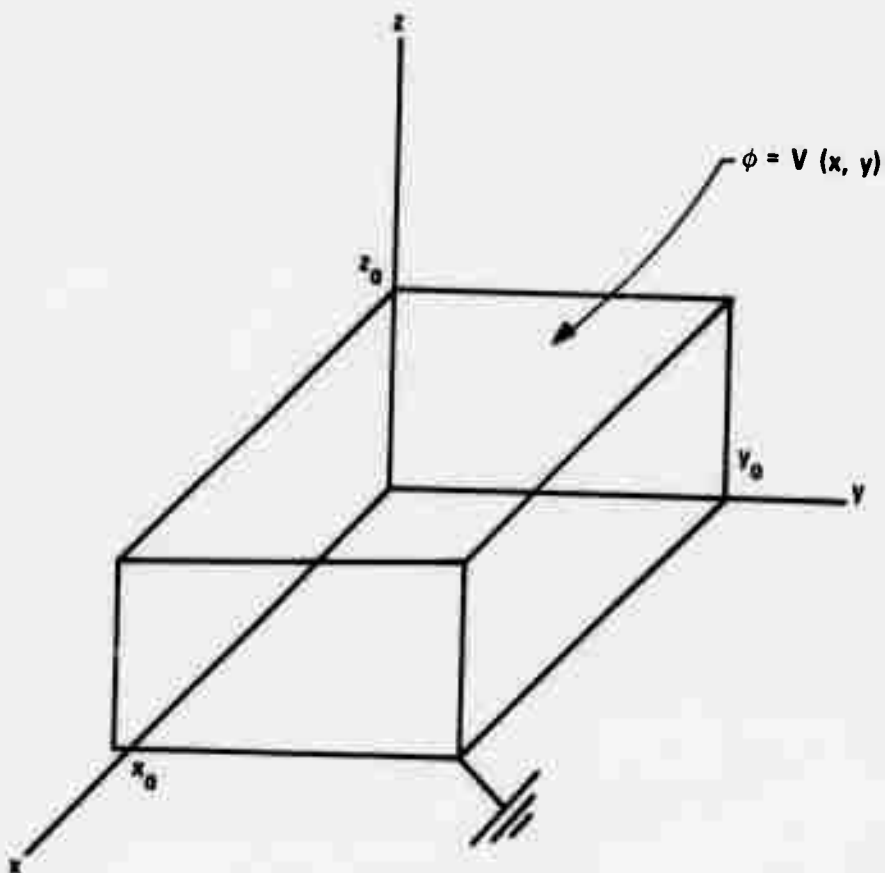


Figure 74. Geometry for Test Problem.

Due to the homogeneity of the boundary conditions at the origin for $x=0$, $y=0$, and $z=0$, a suitable form for the solution inside the box is a product of the rectangular eigenfunctions of the form $\phi = c \sin k_x x \sin k_y y \sinh k_z z$

In order to satisfy the boundary conditions at $x=x_0$ and $y=y_0$,

$$k_x = \frac{m\pi}{x_0} \quad m = 1, 2, 3, \dots$$

$$k_y = \frac{n\pi}{y_0} \quad n = 1, 2, 3, \dots$$

and

$$k_z = \sqrt{k_x^2 + k_y^2} = \sqrt{\left(\frac{m\pi}{x_0}\right)^2 + \left(\frac{n\pi}{y_0}\right)^2}$$

The constant c can be determined by applying the remaining boundary condition at $z=z_0$. If $m=1$ and $n=1$, the constant is given by

$$c = \frac{v_0}{\sinh \sqrt{\left(\frac{\pi}{x_0}\right)^2 + \left(\frac{\pi}{y_0}\right)^2} z_0}$$

and therefore,

$$\phi = v_0 \sin \frac{\pi}{x_0} x \sin \frac{\pi}{y_0} y \frac{\sinh \sqrt{\left(\frac{\pi}{x_0}\right)^2 + \left(\frac{\pi}{y_0}\right)^2} z}{\sinh \sqrt{\left(\frac{\pi}{x_0}\right)^2 + \left(\frac{\pi}{y_0}\right)^2} z_0}$$

b. Test Results

This same problem was run on the UNIVAC 1108 computer using the numerical method with $v_0 = 100$. The numerical solution for a typical planar cross section through the middle of the box is reproduced in Figure 75a; the exact solution for the same cross section is presented in Figure 75b. A comparison of Figures 75a and 75b shows that the maximum error between any two

NUMERICAL SOLUTION

Potential ($z = \text{constant}$)

X	Y →	.000	.000	.000	.000	.000	.000	.000	.000
↓	.000	1.587	2.934	3.836	4.155	3.841	2.942	1.593	.000
.000	.000	2.934	5.425	7.093	7.683	7.103	5.440	2.946	.000
.000	.000	3.836	7.093	9.274	10.045	9.286	7.112	3.851	.000
.000	.000	4.155	7.683	10.045	10.879	10.058	7.703	4.171	.000
.000	.000	3.841	7.103	9.286	10.058	9.298	7.121	3.856	.000
.000	.000	2.942	5.440	7.112	7.703	7.121	5.453	2.953	.000
.000	.000	1.593	2.946	3.851	4.171	3.856	2.953	1.599	.000
.000	.000	.000	.000	.000	.000	.000	.000	.000	.000

EXACT SOLUTION

Potential ($z = \text{constant}$)

X	Y →	.000	.000	.000	.000	.000	.000	.000	.000
↓	.000	1.570	2.901	3.790	4.102	3.790	2.901	1.570	.000
.000	.000	2.901	5.360	7.003	7.580	7.003	5.380	2.901	.000
.000	.000	3.790	7.003	9.149	9.903	9.149	7.003	3.790	.000
.000	.000	4.102	7.580	9.903	10.719	9.903	7.580	4.102	.000
.000	.000	3.790	7.003	9.149	9.903	9.149	7.003	3.790	.000
.000	.000	2.901	5.360	7.003	7.580	7.003	5.360	2.901	.000
.000	.000	1.570	2.901	3.790	4.102	3.790	2.901	1.570	.000
.000	.000	.000	.000	.000	.000	.000	.000	.000	.000

Figure 75. Comparison of Numerically Calculated (a) and Exact (b) Solutions on a Typical Plane Parallel to the x-y Plane.

corresponding points is never greater than 1%. This error bound was obtained in 84 iterations in a total run time of 13.855 seconds.

2. Electric Field Intensity

The electric field is calculated by numerically differentiating the potential. Aitken's "Table Look Up" method⁹ was modified for ascending and descending tables and was programmed to interpolate, extrapolate, and differentiate for this purpose.

The method was developed using an arbitrary n^{th} order matching polynomial; a third degree polynomial was chosen for the present problem, since this gives sufficient accuracy in determining the derivative. One-sided derivatives out of the range of the table (especially the upper and lower end points of the table) can also be approximated.

The grid chosen for the calculation of the potential distribution must be fine enough to cover the pin geometry with enough points so that the calculated numerical derivative approximates the true derivative in the limit of infinitesimally close grid spacing.

In order to calculate the three orthogonal components of the electric field, the program sets up three orthogonal axis through each point of interest and calculates three ordinary directional derivatives, one along each orthogonal axis, and combines these vectorially to produce the gradient of the potential distribution. The electric field intensity is just the negative gradient of the potential distribution.

3. Current Density

The current density emitted from a point on a typical pin is developed from a knowledge of the field external to the point and from the surface properties of the pin in the neighborhood of that point.

The current density is given by the corrected Fowler-Nordheim field emission equation^{10,11}

$$j = \int_{-\infty}^{+\infty} d\epsilon c N(\epsilon, T) \tau(|E|, \epsilon, T)$$

where

$$c = 4\pi \frac{mkT}{h^3}$$

$$N(\epsilon, T) = \ln(1 + e^{-\frac{\epsilon}{kT}})$$

(number density)

$$\text{and } \tau(|E|, \epsilon, T) = e^{-\frac{6.83 \times 10^7 (\phi - \epsilon)^{3/2}}{|E|} f(x)} \quad (\text{transmission coefficient})$$

ϵ energy

T absolute temperature

k Boltzmann's constant

h Plank's constant

m electron mass

ϕ metal work function

$$\text{also } x = \frac{3.79 \times 10^{-4} \sqrt{|E|}}{\phi - \epsilon}$$

and the numerical values of Burgess, Kroemer, and Houston for the field emission function $f(x)$ have been adopted¹² (Table X).

TABLE X

FIELD EMISSION FUNCTION

(for the Fowler-Nordheim Field Emission Equation)

x	f(x)
0.00	1.0000
.05	.9948
.10	.9817
.15	.9622
.20	.9370
.25	.9068
.30	.8718
.35	.8323
.40	.7888
.45	.7412
.50	.6900
.55	.6351
.60	.5768
.65	.5152
.70	.4504
.75	.3825
.80	.3117
.85	.2379
.90	.1613
.95	.0820
1.00	0.0000

When $T = 0$, which is the case of pure field emission and no thermionic emission, the Fowler-Nordheim equation can be integrated analytically and leads to

$$j = \frac{1.54 \times 10^{-5} |E|}{\phi} e^{-\frac{6.83 \times 10^7 \phi^{3/2} f(x)}{|E|}} \Big|_{\epsilon=0}$$

4. Total Current

The total current emitted by a collection of pins is obtained from the current density at each point on the pins by integrating the current density over the surface of each pin and by summing over the total number of pins in the collection

$$i_t = \sum_{\text{pins}} \int_{\text{pins}} \underline{ds} \cdot \underline{j}$$

The surface integral is calculated numerically by multiplying the current density by the area of the grid spacing and summing over the grid.

C. SAMPLE RUN

A single pin geometry corresponding to the prolate spheroidal model, as given in Figure 72, was considered as a sample run with the numerical procedure just described.

The sample prolate spheroid had a height to width ratio of 5 and was subjected to an average field strength of 10^6 V/cm. The numerical grid chosen had 729 uniformly spaced sample points, with the spheroid at its center and completely enclosed in a perfectly conducting box. The numerical solution achieved

after 58 iterations and a total elapsed time of 17.958 seconds was a current density of approximately 15 microamperes per cm^2 . This small current density is consistent with the rather low electric field intensity (compared with values usually encountered in field emission) of 10^6 V/cm .

The method used above is completely general and can be extended to an array geometry without change. The only additional requirement is sufficient computer storage locations to accomodate the greatly increased grid size.

D. SUMMARY

The various models decribed in this report will be used in the following contract period to study the emission properties of several realistic array geometries. A parametric study will be undertaken with the objective of optimizing the total current emitted by the arrays.

SECTION VII

SUMMARY

During the last two years oxide-metal composite structures suitable for electron emission testing have been melt grown under ARPA Order No. 1637. The primary objectives of this study are to understand the growth processes and parameters leading to ordered composite structures during controlled solidification of oxide-metal mixtures and to produce samples suitable for the electronics application evaluation. To meet these objectives the research program is divided into five areas.

- 1) Induction Coupling and Solidification Behavior of Oxides and Oxide-Metal Mixtures.
- 2) The Formation of Optimum Emitting Arrays.
- 3) Oxide-Metal Composite Properties.
- 4) Experimental Emission Measurements.
- 5) Theoretical Analysis of Electron Emitting Arrays.

During the current report period a number of oxides without metal additions have been tested to determine their suitability for melting using the modified floating zone technique. The most noteworthy development of this work was the successful melting of the rare earth oxide Nd_2O_3 indicating that some of the rare earth oxides are candidates for oxide-metal composite growth.

Currently there are four major oxide systems which have been melted with various metals and unidirectionally solidified to form oxide-metal composite structures. These are stabilized HfO_2 with W, stabilized ZrO_2 with various metals, UO_2 with various metals, and rare earth oxides (Gd_2O_3 , Nd_2O_3 and La_2O_3) with W and Mo additions. In the system stabilized HfO_2 -W, numerous samples have been melted using both calcia and yttria as the stabilizer addition. The samples containing yttria produced substantially better composite structures than those containing CaO, mainly because of the formation with CaWO_4 . The optimum oxide-metal composition has been established as well as the influence of various growth atmospheres. Structures containing 70 million approximately 0.15 micron diameter fibers per square centimeter have been routinely produced in the HfO_2 - Y_2O_3 -W system. One drawback of the HfO_2 -W samples is their inability to withstand the thermal gradients inherent in the internal floating zone technique without cracking.

In the system stabilized ZrO_2 -W, yttria has also proved to be the best stabilizer. The influence of rf frequency as well as the optimum yttria and W content have been studied. Some insight into the kinetic processes and mechanisms whereby tungsten is depleted by vaporization of W, WO_2 or WO_3 from the melt zone have also been considered. A series of experiments have shown the influence of growth rate on the size and density of the tungsten fibers in this system and samples containing between 7 and 48 million fibers per square centimeter have been grown. Some initial information relative to discontinuous

(interrupted) fiber growth is also presented. Development of well grown stabilized ZrO_2 -W samples has progressed to the extent that the initial high field electron emission testing of this material was performed. Preliminary attempts to form magnetic metal fibers in stabilized ZrO_2 are also reported; however, the areas of ordered growth obtained to date in the systems stabilized ZrO_2 -Co, Ni or Fe have been minimal.

Work has continued in the model system UO_2 -W and the most noteworthy development has been the discovery of the importance of the O/U ratio of the oxide melt on tungsten solubility. This result has helped to explain some of the inconsistent growth results achieved in the past. As a consequence of this work it was found that maintaining an O/U ratio of the molten oxide of the neighborhood of 2.08 was necessary to achieve sufficient tungsten solubility (3 to 4 weight %) to successfully grow UO_2 -W composites. Various methods, including WO_2 and WO_3 additions, mixtures of high and low O/U ratio powders as well as atmosphere control were investigated as approaches to achieve and maintain the excess oxygen in molten UO_2 -W. All of these approaches were partially successful.

While the use of low O/U ratio UO_2 powders caused poor growth results with W because of limited metal solubility, the same material greatly improved the eutectic growth in UO_2 -Ta samples. Apparently Ta solubility in molten UO_2 is less sensitive to stoichiometry changes of the molten oxide than W. However, extensive microcracking of the matrix was noted in UO_2 -Ta

samples, presumably the result of the high Ta content (approximately 15 weight %) of the eutectic composition.

Within the last six months significant advances have been made in the controlled solidification of the rare earth oxides (Gd_2O_3 , Nd_2O_3 and La_2O_3) doped with CeO_2 in conjunction with W and Mo to form well-ordered crack-free composite structures. The initial work in these systems without CeO_2 additions indicated limited metal solubility in the rare earth oxides; however, with 10 to 20 weight % ceria added to the oxide, larger amounts of metal were dissolved, and very uniform eutectic structures containing both W and Mo fibers were achieved. Some of the properties of the rare earth oxides which make them attractive include their thermal stability, especially in reducing atmospheres, and their ability to withstand the large temperature gradients inherent in the internal floating zone melting technique without cracking. An additional advantage using these materials is the opportunity to easily "harvest" the metal fibers from the oxide matrix. Samples of Gd_2O_3 -Mo or W have shown no tendency to hydrate, a characteristic of many of the rare earth oxides including La_2O_3 and Nd_2O_3 . Because of reproducible growth in these systems, a series of experiments have identified power fluctuations as a major cause of interrupted (banded) growth, and line voltage stabilization should improve fiber continuity in routinely grown samples.

The selective etching of oxide-metal composites has been used to expose the fibers to form structures suitable for electron emission testing. Boiling phosphoric acid has proved

useful for exposing the tungsten fibers in both stabilized HfO_2 and ZrO_2 samples, although variable etching behavior has been encountered. Work has continued using chromic acid as the etchant for UO_2 -W samples. A two step etching process was developed where the fibers were initially pointed and subsequently etched in a solution which did not attack the tungsten to yield sharpened fibers of essentially any desired length. Ultrasonic agitation of the etch greatly increased the etching speed. Rare earth oxide-W or Mo samples have been lightly etched with dilute acid to expose the fibers and form emitting arrays for future emission testing.

Extensive work has been initiated to measure the electrical resistivity of the composite materials and to use electrochemical deposition as a technique to determine metallic fiber continuity. A variety of contact materials and cleaning techniques were tested as approaches to attain effective electrical contact with the very small metallic pins in the composite structures. The use of mercury, indium, as well as vapor deposited metallic coatings were tested as were various chemical cleaning techniques prior to making electrical contact. Major improvements in electrical conductivity were made using these techniques; however, a wide variability in resistance from sample to sample still is a problem.

Electro-chemical deposition using oxide-metal composites as both the anode and cathode was demonstrated. An oxide layer was formed on the individual metallic pins when the sample was the anode, and it is planned to exploit this phenomenon as a method

of achieving a resistor in series with each pin to more nearly equalize the emission performance of the pin arrays. Copper deposits were grown on the ends of individual or groups of pins when the composites were employed as the cathode in a Cu_2SO_4 solution.

Electro-chemical deposition was also performed on samples after emission testing to compare the emission damaged areas with pin continuity as determined through electrodeposition. Arc damaged areas were found to coincide with regions of good pin continuity.

A variety of UO_2 -W and stabilized ZrO_2 -W samples were incorporated in high-field cathode configurations and emission tested. Composite UO_2 -W structures tested included an emitter having pins recessed from the front (emitting) surface, one with pins recessed from the back surface for current limiting, one completely over-coated with gold, and several with their back surfaces gold coated. Two ZrO_2 -W samples with flush pins were also tested. The effect of various anode geometries was evaluated and found to have little effect on the maximum obtainable emission current. Preliminary endurance tests were initiated and an emitter was operated for more than 300 hours at a current density of about 50 mA/cm^2 before failure of a power supply limiting resistor terminated the experiment. This same sample prior to the endurance test produced a maximum current density of 200 mA/cm^2 , which is the largest value yet observed in this work.

The first step in the theoretical determination of the high-field emission electron current is the calculation of the electrostatic potential in the interelectrode space. The present work first considered the case of single spheroidal pins for which there is an exact analytical solution. The exact solution was then compared with a three-dimensional numerical approximation and good agreement was obtained. Additional numerical methods were employed to calculate the electric field at the surface of a single emitter pin and to integrate the quantum mechanical expression for the electron current. The complete calculation was made for this case. Because of the extensive nature of this calculation excessive computer time is required to exchange information between the core and peripheral memory. When techniques currently under development overcome this problem, the theoretical emission expected from pin arrays of different geometries will be calculated.

REFERENCES

1. A. T. Chapman, et. al., "Melt-Grown Oxide-Metal Composites", Semi-Annual Technical Report (No. 3), ARPA Order No. 1637 and Contract DAAH01-71-C-1046, School of Ceramic Engineering, Georgia Institute of Technology, January 1972.
2. A. T. Chapman, et. al., "Melt-Grown Oxide-Metal Composites", Final Technical Report (No. 2), ARPA Order No. 1637 and Contract DAAH01-70-C-1157, School of Ceramic Engineering, Georgia Institute of Technology, July 1971.
3. A. T. Chapman, et. al., "Melt-Grown Oxide-Metal Composites", Semi-Annual Technical Report (No. 1), ARPA Order No. 1637 and Contract DAAH01-70-C-1157, School of Ceramic Engineering, Georgia Institute of Technology, January 1971.
4. P. Duwez, "The Zirconia-Yttria System", J. Electrochem. Soc. 98 No. 9, 356-362 (1951).
5. R. E. Latta and R. E. Fryxell, "Determination of the Solidus-Liquidus Temperatures in the UO_{2+x} System ($-0.50 < x < 0.20$)", J. Nuc. Materials 35 195-210 (1970).
6. A. T. Chapman, et. al., "Stoichiometry Changes in Molten Uranium Dioxide", presented at the 74th Annual Meeting of the Am. Cer. Soc., Washington, D.C. (paper 25-N-72) May 10, 1972.
7. R. P. Little, "Electrical Breakdown in Vacuum", IEEE TRANS on Electron Devices ED-12 (2) 77-83 (1965).
8. J. D. Levine, "The 3-D Electrostatic Potential Surrounding a Square Array of Surface Charges", Surface Sci. 10 313-326 (1968).
9. Abramowitz and Stegen, NBS Handbook, Ch. 25.
10. R. H. Fowler and L. Nordheim, "Electron Emission in Intense Electric Fields", Roy. Soc. Proc., A, 119 173 (1928).
11. L. W. Nordheim, "The Effect of the Image Force on the Emission and Reflection of Electrons by Metals", Roy. Soc. Proc., A, 121 626 (1928).
12. R. E. Burgess, N. Kroemer and J. M. Houston, "Corrected Values of Fowler-Nordheim Field Emission Functions $v(y)$ and $s(y)$ ", Phys. Rev. 90 No. 4, 515 (1953).